SCUOLA
NORMALE
SUPERIORE

Classe di Scienze

Corso di perfezionamento in
Fisica

XXXV ciclo

The impact of primordial black holes on the high redshift Universe

Settore Scientifico Disciplinare **FIS/05**

Candidato
dr. Francesco ZIPARO

Relatori

Prof. Andrea FERRARA

Prof. Simona GALLERANI

SCUOLA
NORMALE
SUPERIORE

Anno accademico 2023/2024

Contents

Abstract

Recent measurements of the cosmic X-ray and radio backgrounds (CXB/CRB, respectively), obtained with Chandra and ARCADE2, report signals in excess of those expected from known sources. Similarly, measurements of the near infrared background (NIRB) angular power spectrum on angular scales $\theta \gtrsim 1$ arcmin exceeds by roughly two order of magnitudes predictions from known galaxy populations. The nature of the sources producing the CXB/CRB excesses, and the NIRB fluctuations remains unknown, suggesting the presence of a yet undiscovered population of emitters. Interestingly, the NIRB has been found to cross-correlate with the soft-X-ray background (SXB), possibly justified by X-ray emission from elusive, high redshift accreting black holes (BHs).

In this context, the most recent *James Webb Space Telescope* (JWST) observations have revealed the presence of $z \sim 6 - 11$ active galactic nuclei (AGN) powered by accreting MBHs ($M_{\rm BH} \sim 10^{6-8}\ M_\odot$). The existence of these sources, along with supermassive black holes (SMBHs, $M_{\rm BH} \sim 10^{8-10}\ M_\odot$) powering $z \sim 6 - 7.5$ quasars, poses a puzzle for current theoretical models of BH formation and evolution. It is indeed still unclear both the nature of the seeds from which these SMBHs are formed and their ability to grow fast enough to assemble an SMBH in less than 1 Gyr (the age of the Universe at $z \sim 6$). These results can be interpreted as requiring either massive ($M_{\rm BH} \sim 10^{4-6}\ M_\odot$) seeds and/or less extreme BHs experiencing bursts of super-Eddington accretion.

In this Thesis, we tackle the aforementioned puzzles by ascribing their solution to a population of accreting primordial black holes (PBHs). PBHs are black holes that are expected to have formed during the radiation dominated era from the collapse of overdense regions, and have been considered as potential dark matter (DM) candidates.

In particular, the questions we would like to answer are:

- *Can PBHs be the sources of the observed backgrounds excess?*
- *Can PBHs lead to the formation of SMBHs seeds?*

This thesis describes the PBH theoretical model we developed and presents the analysis we carried out to answer the aforementioned two open questions. The structure of the thesis is outlined as follows:

1. Chapter 1 contains a general overview of the cosmological context of the Thesis, with a description of the thermal history of the Universe, from the Big Bang to the present days. It incorporates the description of the cosmic microwave background, an introduction to the formation of the first cosmological structures and the first stars, underlining the importance of the 21-cm signal for studying the dark ages of the Universe.

2. Chapter 2 describes the observations of the X-ray, radio and near infrared backgrounds. It focuses on the problem of the observed excesses, and briefly discusses the theoretical solutions proposed to interpret these observations.

3. Chapter 3 introduces the observational evidences of supermassive black holes (SMBHs) both in the local Universe and at high redshift ($z \sim 6$). In particular, we present the latest results concerning SMBHs at high redshift ($z \sim 6 - 11$), as observed with the James Webb Space Telescope (JWST). Furthermore, we outline the several channels proposed by theoretical models to form SMBH seeds at high-z.

4. In Chapter 4, we provide an introduction to primordial black holes (PBHs). We discuss their importance in the context of dark matter (DM), and we review their formation channels and the current existing constraints on their abundance.

5. In Chapter 5, we describe the semi-analytical model used to compute the PBHs accretion at high redshift. It also shows the results of our calculations and the resulting constraints on the fraction of PBHs in DM from the CXB/CRB measurements.

6. In Chapter 6, we extend the analysis presented in the previous chapter to the NIRB. By adopting an improved version of the model, we discuss the impact of PBHs accretion onto the NIRB, and update the constraints on the fraction of PBH in DM.

7. In Chapter 7, we consider the possibility that PBHs cluster in the center of DM halos and undergo runaway merger leading to the formation of massive ($M_{\rm seed} \sim 10^5\ M_\odot$) seeds at $z \gtrsim 10$. Based on this process, we propose a novel seeding prescription, and discuss its implications in the context of the latest JWST observation of $z \sim 6 - 11$ AGN.

8. In Chapter 8, we summarise all the results obtained in this work and mention future possible applications of our theoretical model to the study of gravitational waves from PBHs.

Part I

Theoretical and observational backgrounds

Cosmological Introduction 1

This chapter provides a concise introduction to the cosmological context of the Thesis and outlines an overview of the thermal history of the Universe from the Big Band to the present day.

1.1 Cosmological framework

During the last century, two events posed the basis for modern cosmology: Einstein introduced the theory of general relativity to describe gravity (Einstein, 1916); Hubble measured the radial velocity of extra-galactic objects, introducing the Hubble's law (Hubble, 1929). Moreover, the discovery of the Cosmic Microwave Background (CMB, Penzias & Wilson, 1965) radiation pointed us in the direction of the hypothesis of the "Hot Big Bang" model, with respect to the steady state one. From a theoretical point of view, the standard cosmological model relies on the assumption that *On sufficiently large scales, the Universe is homogeneous and isotropic* (Peebles, 1993). Originally, Einstein assumed a homogeneous and isotropic Universe to simplify his equations. Homogeneity implies that physical conditions are uniform at every point in space, while isotropy indicates that the Universe appears the same in all directions. These assumptions have proven to be a good approximation of the Universe on the largest observable scales, exhibiting fluctuations of about 10^{-5} around the average, as first revealed by measurements of the Cosmic Microwave Background (CMB) radiation.

In the framework of the General Relativity, the geometry of an homogeneous and isotropic Universe is described by the Friedmann- Lemaître-Robertson-Walker (FLRW) metric:

$$ds^2 = c^2dt^2 - a^2(t)\left[\frac{dr^2}{1-kr^2} + r^2d\Omega^2\right] \tag{1.1}$$

where a(t) is the cosmic scale factor, which describes the expansion of the Universe, and k is the curvature. The metric described by Eq. 1.1 enters Einstein equations that describe the dynamics of the Universe:

$$R_{\mu\nu} - \frac{1}{2}g_{\mu\nu}R = \frac{8}{c^4}T_{\mu\nu} + \Lambda g_{\mu\nu}, \tag{1.2}$$

where where $R_{\mu\nu}$ is the Ricci tensor, R is the curvature scalar, $T_{\mu\nu}$ is the energy-momentum tensor, Λ is the dark energy term or vacuum energy, and G is the gravitational constant. Λ was originally introduced as the cosmological constant in order to allow for a static solution to his equations. After discovering that the Universe expansion is accelerating (Riess et al., 1998), cosmologist reevaluated the cosmological constant. In an expanding Universe, the uniform energy density term progressively increases its pressure support, which accelerates the expansion.

The expansion of the Universe is related to the Hubble's law, that can be derived by expressing this expansion in the FLRW coordinates. The distance between two points in space is given by $r(t) = a(t)R_c$, where R_c is the comoving coordinate. This coordinate represent a framework expanding at the same rate of our Universe. The physical distance between the two points changes over time, and the velocity by which they recede from each other is given by $v = dr/dt = \dot{a}R_C$. We can then relate the distance with the velocity, obtaining the Hubble's law:

$$v = \frac{\dot{a}(t)}{a(t)} = H(t)r, \tag{1.3}$$

where $H(t)$ is the Hubble's constant, and it represent the expansion rate of the Universe.

This expansion modifies the energy of travelling photons, emitted at t_1 and observed at t_0. The quantity $cdt/a(t)$ is conserved, thus:

$$dt_1 = \frac{a(t_1)}{a(t_0)}dt_1. \tag{1.4}$$

Given that the frequency of a photon scales as $\nu \propto dt^{-1}$, the previous equation can also be expressed as:

$$\frac{\nu_1}{\nu_0} = \frac{\lambda_0}{\lambda_1} = \frac{a(t_0)}{a(t_1)}, \tag{1.5}$$

where λ is the photon's wavelength. The redshift z is defined as the relative difference between the observed and emitted wavelengths of a photon:

$$z(t_1) = \frac{\lambda_0 - \lambda_1}{\lambda_0}, \tag{1.6}$$

and consequently:

$$1 + z(t_1) = \frac{a(t_0)}{a(t_1)} = \frac{1}{a(t_1)}, \tag{1.7}$$

defining $a(t_0) = 1$. The redshift is conventionally used to express both the distance of an observed objects and the time in the past at which we are observing them.

For an homogeneous and isotropic Universe, filled by a perfect fluid with density ρ and pressure P, the scale factor evolves according to the Friedmann's equations (Friedmann, 1922):

$$\left(\frac{\dot{a}}{a}\right)^2 = \frac{8\pi G}{3}\rho - \frac{kc^2}{a^2}, \tag{1.8}$$

$$\frac{\ddot{a}}{a} = -\frac{4\pi G}{3}\left(\rho + \frac{3P}{c^2}\right). \tag{1.9}$$

From this set of two equations, the critical density (ρ_c) of the Universe can be derived:

$$\rho_c = \frac{3H^2}{8\pi G} \simeq 8.5 \times 10^{-30}\left(\frac{H}{H_0}\right)^2. \tag{1.10}$$

It represent the density (considering all the fluid components) necessary to have a flat Universe, that is the curvature parameter $k = 0$. Assuming an equation of state $P = w\rho c^2$, the first Friedmann's equation can be rewrite by considering the three energy-components contributing to ρ, and normalizing them with the present-day critical density ($\rho_{c,0}$):

$$\frac{H(t)}{H_0} = \sqrt{\Omega_m + \Omega_r + \Omega_\Lambda}, \tag{1.11}$$

where we have defined $\Omega_i = \rho_i/\rho_{c,0}$. Finally, we can express each component in terms of its present-day value, considering their scaling with the scale factor:

$$\frac{H(t)}{H_0} = \sqrt{\frac{\Omega_{m,0}}{a^3} + \frac{\Omega_{r,0}}{a^4} + \Omega_{\Lambda,0}}. \tag{1.12}$$

This equation describes the evolution of the Universe in terms of the matter-energy components that fill it.

1.2 Thermal history of the Universe

In this section, we describe the processes involved in the evolution of the Universe, pinpointing crucial moments that mark the different phases of the Universe's evolution.

1.2.1 From the Big Bang to recombination

The Universe originated from the event known as the Big Bang, which we consider as the beginning of the time ($t = 0$). With current scientific tools, it is not possible to explain how this event occurred or what happened in the very first moments of the Universe's existence. The so-called Planck time ($t_{Pl} \sim 10^{-43}$ s) represents the time scale beyond which our current physical models lose their predictive power.

At the very early stages the Universe was extremely hot and dense and there was thermal equilibrium. Matter was ultra relativistic due to thermal agitation, therefore radiation dominated in terms of energy budget. During this period the scale factor (i.e. the characteristic spatial dimension of the Universe) varies with time as: $a(\tau) \propto \tau^{1/2}$ (Peebles, 1993), where τ is the proper time. Using this relation, we can also derive the dependence on time of the Hubble parameter during the radiation dominated epoch: $H = \dot{a}/a = 1/2t$ (Peacock, 1998). These two relations describe the expansion of the Universe at this stage. The thermal equilibrium condition depends on two parameters, the interaction rate Γ_{int} and the expansion rate H. Thermal equilibrium holds until: $\Gamma_{int} \gg H$ (Dodelson, 2003).

Around $t \sim 10^{-34}$ s the inflationary period took over. The universe experienced exponential expansion (~ 60 e-folds, Loeb 2010) driven by an elevated vacuum state energy density. This expansion, lasting until about $t \sim 10^{-32}$ s, flattened any initial curvature of space-time, resulting in a nearly flat geometry. The rapid expansion also led to nearly uniform conditions across regions far larger than our observable universe. Additionally, inflation seeded tiny quantum fluctuations, which later evolved into the density perturbations responsible for the formation of galaxies and other large-scale structures. Inflation is thus crucial for explaining both the overall properties and the seeds of structure formation in the Universe.

After $t \sim 10^{-32}$ s, radiation begun to dominate again. While the Universe expanded, it also cooled down. We can compute the dependence on time of the temperature considering that during this early stage of the Universe life there was thermal equilibrium, as well as homogeneity and isotropy. As a consequence entropy S was conserved. Applying the first principle of thermodynamics, we get:

$$S = \frac{(\rho_R + P)V}{T} \tag{1.13}$$

where V and T represent the volume and the temperature. The volume scales as the cube of the scale factor $V \propto a^3$, and since for relativistic (hot) matter $P = \rho_R/3$, we have: $S \sim 4a^3\rho/3T$.

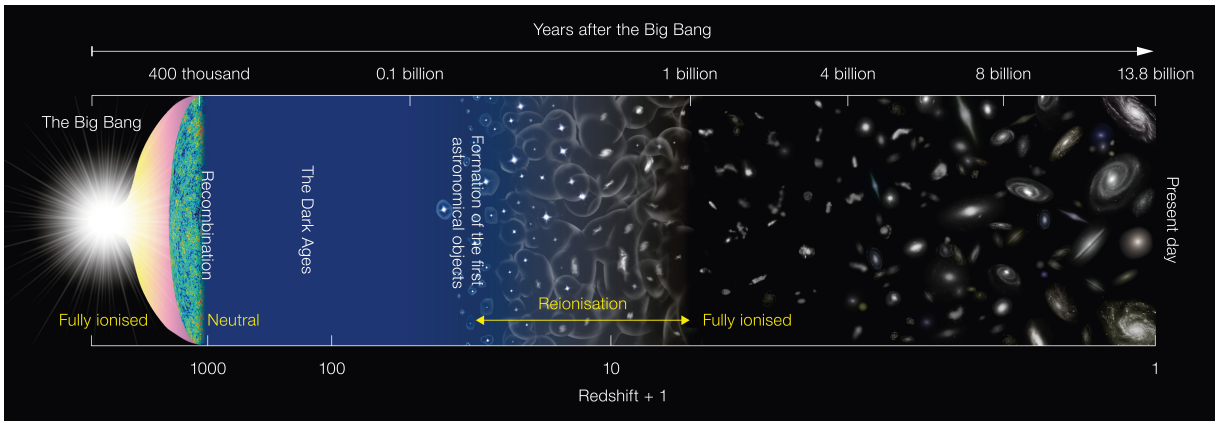

Figure 1.1: Schematic view of the thermal history of the Universe. Credit: National Astronomic Observatory of Japan (NAOJ).

The hot matter energy density scales as: $\rho_r \propto a^{-4}$, then the conservation of entropy implies that the temperature decreases as: $T \propto a^{-1}$, which is equivalent to $T \propto t^{-1/2}$.

After $t \sim 10^{-12}$ s the thermal energy of the Universe decreased enough to be comparable to the electroweak scale $k_B T \sim$ TeV. When this happens the symmetry between electromagnetic and weak interactions breaks. As the Universe cooled to a temperature of hundreds of MeV, protons and neutrons condensed out of the primordial quark-gluon plasma through the so-called QCD phase transition ($t \sim 10^{-6}$ s). At about one second after the Big Bang, the temperature declined to ~ 1 MeV, and the weakly interacting neutrinos decoupled. Shortly afterward the abundance of neutrons relative to protons froze and electrons and positrons annihilated. In the next few minutes, nuclear fusion reactions produced light elements more massive than hydrogen, such as deuterium, helium, and lithium, in abundances that match those observed today in regions where gas has not been processed subsequently through stellar interiors.

Although the transition to matter domination occurred at a redshift $z \sim 3.3 \times 10^3$ ($t \sim 4 \times 10^5$ Myr), the Universe remained hot enough for the gas to be ionized, and electron-photon scattering effectively coupled ordinary matter and radiation (Peebles, 1993). At $z \sim 1.1 \times 10^3$ the temperature dipped below ~ 3000 K, and free electrons recombined with protons to form neutral hydrogen atoms. As soon as the dense fog of free electrons was depleted, the Universe became transparent to the relic radiation, which is observed at the present time as the cosmic microwave background (CMB).

The CMB today corresponds to an almost perfect black body emission, isotropic and homogeneous, whose temperature is $T_{\rm CMB} = 2.72548 \pm 0.00057$K (Planck Collaboration, 2018). At this stage, after recombination and decoupling, the Universe was transparent but no stars had formed yet, so there were no sources of light. For this reason this period is commonly referred to as "The Dark Ages" (redshift $z \sim 100$ to ~ 10). The only photons in the Universe were those of the CMB and 21cm occasional radio emissions arising by the spin-flip of hydrogen atoms.

1.2.2 The Cosmic microwave background radiation

The spectrum of the cosmic microwave background (CMB) closely matches that of an almost perfect black body with a temperature of 2.7 K. In the early Universe, when photons were in thermal equilibrium with matter, the number density of photons at a given temperature T, within

a frequency range from ν and $\nu + \delta\nu$, can be described by the black body spectrum:

$$n_T(\nu)d\nu = \frac{8\pi\nu^2 d\nu}{exp(h\nu/K_B T) - 1}. \tag{1.14}$$

As time passed the matter became cooler and less dense, and eventually the radiation began a free expansion but its spectrum has kept the same form. The number density evolves with the Robertson-Walker scale factor $a(t)$ as:

$$n(\nu, t)d\nu = \big(a(t_L)/a(t)\big)^3 n_{T(t_L)}\big(\nu a(t)/a(t_L)\big)d(\nu a(t)/a(t_L)) \tag{1.15}$$

where t_L it the time of the last scattering surface. Substituting back in eq. 1.14, we find:

$$n(\nu, t)d\nu = \frac{8\pi\nu^2 d\nu}{exp(h\nu/K_B T(t)) - 1} = n_{T(t)}(\nu)d\nu \tag{1.16}$$

where $T(t) = T(t_L)a(t_L)/a(t) = T(t_L)(1 + z)$. Hence, the photon density always had a black body form, but the temperature increases with redshift. In the 1990s, observations with the FIRAS radiometer aboard the Cosmic Background Explorer Satellite (COBE) confirmed that the Planck spectrum of the microwave background has an almost perfect black body spectrum. This was observed in the wavelength range from 0.05 cm to 0.5 cm with a precise temperature measurement of $T_{\rm CMB} = 2.72548 \pm 0.00057$ K.

Photons ceased to exchange energy effectively with electrons when the temperature of the expanding Universe dropped to about 10^5 K. After that, photons continued to be scattered by free electrons but without appreciable gain or loss of energy. The Universe became fully transparent to CMB photons when the free electrons became bound into hydrogen and helium atoms, at the epoch of Recombination. We now want to give an estimation of the time at which this process occurred. The equilibrium condition for recombination is given by:

$$\mu(e) + \mu(p) = \mu(H). \tag{1.17}$$

Where the chemical potentials μ are obtained from the expressions for the occupation number, N:

$$N = e^{\mu - \epsilon/kT}. \tag{1.18}$$

The number of particles per unit volume is given by:

$$n = \frac{g}{(2\pi\hbar)^3}\int d^3p e^{\mu - \epsilon/kT}, \tag{1.19}$$

where g is the number of spin states. The energy is the sum of the annihilation and kinetic energies $\epsilon = mc^2 + \frac{p^2}{2m}$, resulting in:

$$n = g\frac{(2\pi m k_B T)^{3/2}}{(2\pi\hbar)^3}e^{\mu - \epsilon/k_B T}. \tag{1.20}$$

Replacing the above expression in eq.(1.18) and recalling the value of the hydrogen atom binding energy $B = 13.6$ eV, we can write the Saha thermal ionization equilibrium equation:

$$\frac{n_e n_p}{n_h n} = \frac{x^2}{1 - x} = \frac{(2\pi m_e k_B T)^{3/2}}{n(2\pi\hbar)^3}e^{-B/k_B T}, \tag{1.21}$$

where $xn_H = n_e = n_p$ is the fraction in proton of the total number density. We can write this equation as a function of the total number density of protons n considering that $n_p + n_H = n$(where n_H is the number density of HI atoms). We can then use the definition of the proton number density n:

$$n = 1.12x10^{-5}\Omega_B^2(1+z)^3\mathrm{cm}^{-3}, \tag{1.22}$$

where Ω_B is the baryonic cosmological parameter. Recalling that the equilibrium temperature corresponds to the CMB temperature $T = 2.72548(1+z)$ K, we can rewrite eq. 1.21 as:

$$log[x^2/(1-x)] = 20.99 - log[\Omega_B h^2(1+z)^{3/2}] - 25050/(1+z). \tag{1.23}$$

If we fix $\Omega_B h^2 = 0.013$ (h being the reduced Hubble constant) and choose $x = 0.5$, we find:

$$z_{at} = 1360, T_{at} = T_0 z_{at} = 3700 \text{ K}, \tag{1.24}$$

where z_{at} is the redshift at which the first atoms have formed, and T_{at} is the correspondent temperature. However, for different values of $\Omega_B h^2$ we get slightly different results for z_{dec}, the redshift of decoupling, and T_{at}, so the reference value is the intermediate $z_{dec} \equiv 1300$.

When the recombination rate falls below the expansion rate, the formation of neutral atoms ceases. The remaining electrons and protons have negligible probability of combining with each other. For $T < T_{dec}$ photons are decoupled from the rest of matter. Comparing the rate of Thomson scattering Γ with the expansion rate H (the Hubble parameter) we can get a good esteem of the epoch of decoupling, t_{dec}:

$$\Gamma = \sigma x_e n_B = 3.36 \times 10^{-11}(\Omega_B h^2)^{1/2}\tau^{9/4}exp(-6.8\tau)\mathrm{cm}^{-1} \tag{1.25}$$

where $\tau = T_{dec}/1\mathrm{eV}$. Matching the two rates $\Gamma = H$ and solving for τ we get:

$$\frac{1}{\tau} \simeq 3.972 + 0.0735ln(\Omega_B/\Omega) \tag{1.26}$$

resulting in the value for $T_{dec} \simeq 3000$K or $(1+z)_{dec} \simeq 1100$. From the optical depth, we can also compute the probability that photons were last scattered in the interval $(z, z+dz)$:

$$P(z) = e^{-\tau}\frac{d\tau}{dz} = 5.26x10^{-3}\left(\frac{z}{1000}\right)^{13.25} exp\left[-0.37\left(\frac{z}{1000}\right)^{14.25}\right]. \tag{1.27}$$

This $P(z)$ has a sharp maximum at $z \simeq 1070$ and a width of about $\Delta z \simeq 80$, it is reasonable to assume this value as the one for the redshift of occurrence of the last scattering surface.

So far we treated CMB radiation as a perfect black body, however both WMAP and Planck (Hinshaw et al., 2013; Planck Collaboration, 2018) have observed spatial variations in the CMB temperature of the order $\Delta T/T \sim 10^{-5}$ across $10-90$ on the sky. We can apply linear perturbation theory to describe this small fluctuations. In particular, we can use spherical harmonics to describe them, since they are distributed over the surface of a sphere with the Earth in the center. Indeed, for statistically isotropic, Gaussian random temperature fluctuations an harmonic description is more efficient than a real space one. The RMS expansion of the spherical harmonics coefficients gives the power spectrum of the CMB, its most important observable.

Most of the structure in the temperature anisotropy is associated with acoustic oscillations of the photon-baryon plasma on $\sigma \sim 1$ scales. Since we are interested in the deviation from the average temperature, we generally define the dimensionless quantity:

$$\Theta(\hat{n}) = \frac{T(\hat{n}) - \langle T\rangle}{\langle T\rangle} \tag{1.28}$$

where $\hat{n}$ is a generic direction in the sky. We can then write Θ in spherical harmonics as:

$$\Theta(\hat{n}) = \sum_{l,m} a_{l,m} Y_{l,m}(\hat{n}) \tag{1.29}$$

where

$$a_{l,m} = \int \Theta(\hat{n}) Y^*_{l,m}(\hat{n}) d\Omega \tag{1.30}$$

For statistically isotropic fluctuations, the ensemble average of the temperature fluctuations is described by a power spectrum:

$$\left\langle a^*_{l,m} a_{l',m'} \right\rangle = \delta_{l,l'} \delta_{m,m'} C_l. \tag{1.31}$$

So we can find a relation for C_l given by:

$$C_l = \frac{1}{2l+1} \sum_{m=-l}^{l} |a_{l,m}|^2 . \tag{1.32}$$

Theoretical expectation are in good agreement with the observed data as it is shown in figure(1.2). The large variance observed at large scales (small l) is called cosmic variance

$$\Delta C_l = \sqrt{\frac{2}{2l+1}} C_l, \tag{1.33}$$

and it is due to the fact that we can only observe one of the many possible Universes. Each acoustic peak in the CMB power spectrum gives additional information on a specific aspect of our Universe.

Generally the first three peaks are taken into account and the remaining part of the spectrum is treated as a damping tail:

The first peak has been localized around $l \sim 200$ from many observations after COBE. This peak in the power spectrum depends sensitively on the spatial curvature of the Universe and his position indicates that the Universe is very close to spatially flat.

The baryon-photon ratio controls the even-odd modulation of peak heights through the baryon loading effect. This is due to the fact that baryons add extra mass to the photon-baryon plasma or equivalently an enhancement of the momentum density of the plasma. The detection of the second peak in the CMB can be used to constrain the baryon density.

The third peak begins to show the effects of the matter-radiation ratio on the overall amplitude of the acoustic peaks. Furthermore, decay in the gravitational potential during radiation domination would reduce the baryon loading effect and change the peak height ratios of the second and third peaks.

Diffusion damping of photons is dominating in the $l \gg 1$. The amplitude of the acoustic peaks drops off rapidly at the highest multipoles or smallest angular scales. What happens is that the physical scale of these fluctuations are so small that they are comparable to the distance photons travel during recombination. In that short period during which the Universe recombines, the photons bounce around the baryons and execute a random walk. If the random walk takes the photons across a wavelength of the perturbation, then the hot and cold photons mix and average out. The acoustic oscillations are exponentially damped on scales smaller than the distance photons random walk during recombination.

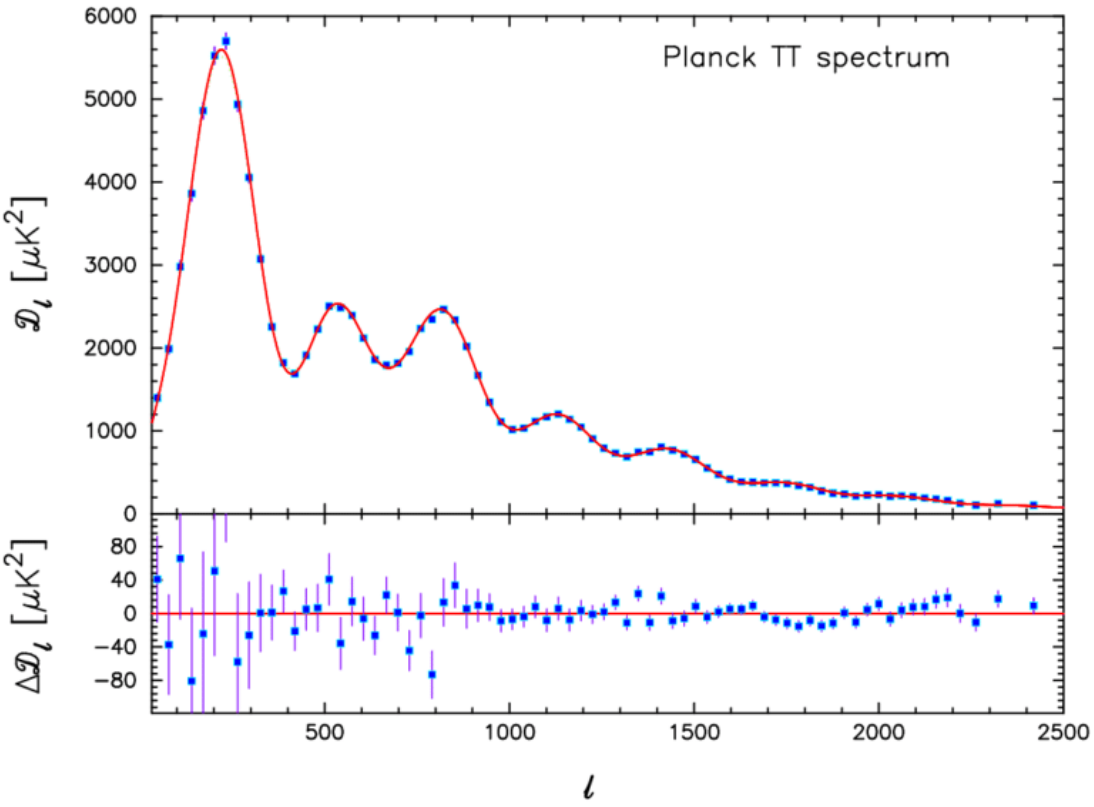

Figure 1.2: Angular power spectrum of the CMB radiation. Blue squares show Planck data, while the red line represent the theoretical prediction for the ΛCDM model. The lower panel shows the distance between measurements and the best fit. Credit: *Planck Collaboration*. Credit: Bucher 2015.

In the end, the analysis of the peak of the CMB give us information of the different components of the Universe today. At the moment our Universe is around 13.7 billion years old (Loeb, 2010), the baryon density parameter is $\Omega_b h^2 = 0.0224 \pm 0.0001$, the matter density parameter is $\Omega_m h^2 = 0.315 \pm 0.007$, the dark energy density is $\Omega_b h^2 = 0.685 \pm 0.0007$ and the Hubble constant value is $H_0 = (67.4 \pm 0.5)$ km s^{-1}Mpc^{-1} (Planck Collaboration, 2018).

1.2.3 Dark Ages and the 21 cm signal

After recombination and decoupling, the Universe had cooled enough to allow light to travel long distances, but there were no light-producing structures such as stars and galaxies. Stars and galaxies are formed when dense regions of gas form due to the action of gravity, and this takes a long time within a near-uniform density of gas and on the scale required, so it is estimated that stars did not exist for perhaps hundreds of millions of years after recombination. This period is known as Dark Ages and had last between redshift $z \sim 1100$ and redshift $z \sim 10$. Due to the absence of sources of light, a different way to probe this epoch the Universe has to be used. At this stage, the Universe was mainly composed of neutral hydrogen, thus the 21 cm line is what is used to investigate the Dark Ages.

The 21 cm refers to the electromagnetic radiation spectral line that is created by a change in the energy state of neutral hydrogen atoms. This electromagnetic radiation is at the frequency

of 1420.4 MHz which correspond the the wavelength of 21.1 cm that falls within the microwave region of the electromagnetic spectrum. This line represents till now the only tool to probe the Dark Ages and has potentially two applications, it provides:

- a very precise picture of the matter power spectrum in the period after recombination
- a picture of how the Universe was reionized

This line arises due to a spin flip process in the hydrogen atom (in the ground state). The excited triplet state is a state in which the spins are parallel whereas the spins at the singlet state are antiparallel, this generate a spontaneous hyperfine transition between the two (Scott & Rees, 1990; Madau et al., 1997). The 21 cm line should be a forbidden one given the extremely low value of the Einstein coefficient $A_{1\to0} = 2.85 \times 10^{-15}$ s^{-1}. This correspond to a lifetime of the triplet state of $1.1 \cdot 10^7$ years for spontaneous emission. Despite the extremely low rate the lines remains a powerful tool simply due to the vast amounts of hydrogen in the Universe.

The intensity of the 21 cm radiation is controlled by one parameter, the spin temperature T_{spin} (Madau, Meiksin & Rees, Zar):

$$\frac{n_1}{n_0} = 3exp(-T_*/T_{spin}), \tag{1.34}$$

where n_0 and n_1 are the number densities of electrons in the triplet and in the singlet state of the hyperfine level respectively, and $T_* = 0.0681$ K is the temperature corresponding to the 21 cm wavelength. The spin temperature is then another way to express the ratio between the occupation number of the two hyperfine levels. This ratio establishes the intensity of the radiation emerging from a cloud of neutral hydrogen. In the measurement of such radiation one has to take into account the level of background being transmitted through a given cloud as well as the amount of absorption and emission within the cloud, this can be done with the radiative transfer equation. This is usually expressed in terms of the brightness temperature of the radiation I_ν. Following the description by Rybicki & Lightman 1986, this quantity is defined as the intensity per differential frequency element in the form

$$I_\nu = \frac{dI}{d\nu}. \tag{1.35}$$

The radiative transfer equation for thermally emitting material at temperature T can be written in terms of the optical depth for absorption as

$$\frac{dI_\nu}{d\tau\nu} = -I_\nu + B_\nu(T), \tag{1.36}$$

where τ_ν is the optical depth for absorption through the cloud at a given frequency and B_ν is the Planck function. In cosmology the intensity I_ν is often expressed by its equivalent brightness temperature, $T_b(\nu)$. This is convenient because at the Rayleigh-Jeans low energy limit, the relation between the brightness temperature and specific intensity is given by (Madau, Meiksin & Rees, Zar):

$$T_b(\nu) \approx \frac{I_\nu c^2}{2K_B\nu^2}. \tag{1.37}$$

Expressing the radiative transfer equation in terms of the brightness temperature gives it a particularly simple form

$$\frac{dT_b}{d\tau_\nu} = -T_b + T_{\rm CMB}, \tag{1.38}$$

where the CMB temperature is chosen as background temperature. The solution of the previous equation give us an expression for the emergent radiation at frequency ν

$$T_b(\nu) = T_{\rm spin}(1 - e^{-\tau_\nu}) + T_{\rm CMB}(\nu)e^{-\tau_\nu}, \tag{1.39}$$

where $T_{\rm spin} = T_b(0)$ is the brightness temperature in the absorbing cloud. Notice that in the case in which $T_{\rm spin} = T_{\rm CMB}$ the brightness temperature gives exactly the CMB temperature. This is simply because in this case there is a prefect balance between the absorption and emission at every frequency. Therefore, the measurement in this case does not reveal any additional information about the intervening cloud. The spin temperature plays a key role in the process, so its definition is crucial. $T_{\rm spin}$ is the sum of three elements and their coefficients:

- absorption of CMB photons,
- collisions with other hydrogen atoms, free electrons, and protons,
- scattering of Lyα photons through excitation and de-excitation.

The spin temperature can be expressed as

$$T_{spin} = \frac{T_{CMB} + x_{kin}T_{kin} + x_\alpha T_\alpha}{1 + x_{kin} + x_\alpha}, \tag{1.40}$$

where x_{kin} and x_α are the kinetic and Lyα coupling terms respectively. The kinetic coupling term x_{kin} is due to collisional excitations of the 21 cm transitions. The Lyα coupling term x_α is due to the so called Lyα pumping mechanism, also known as the Wouthyusen-Field effect.

As we mentioned above the measured quantity in radio astronomy is the brightness temperature, or more accurately the so called differential brightness temperature $\delta T_b \equiv T_b - T_{\rm CMB}$. The behavior of this key quantity can be obtained from the previous equations:

$$\delta T_b = 27{\rm mK}(1+\delta)\bar{\rm x}_{\rm HI}\left(\frac{\Omega_{\rm b}{\rm h}^2}{0.023}\right)\sqrt{\frac{1+{\rm z}}{10}\frac{0.15}{\Omega_{\rm m}{\rm h}^2}}\left(1 - \frac{{\rm T_{CMB}} + {\rm T_{rad}}}{{\rm T_{spin}}}\right), \tag{1.41}$$

where $\bar{x}_{HI}$ is the volume averaged ionized fraction (Mirocha & Furlanetto, 2019).

1.2.4 Structures formation

Observations of the CMB show that at the time of hydrogen recombination the Universe was extremely uniform, with spatial fluctuations in the energy density and gravitational potential of roughly one part in 10^5. These small fluctuations grew over time during the matter-dominated era as a result of gravitational instability, and eventually led to the formation of galaxies and larger-scale structures observed today. In order to describe the perturbation growth over the matter-dominated era ($z \ll 3.3 \times 10^3$), let us consider small perturbations $|\delta| \ll 1$ from the uniform background density ρ_0 of cold non collisional matter (i.e. clod dark matter):

$$\delta(x,\tau) = \frac{\rho(x,t)}{\rho_0(t)} - 1 \tag{1.42}$$

We can then use the equations of fluidodynamics (the continuity, Poisson and Euler equations) to describe the evolution of cold dark matter. The fluid approximation is valid until the

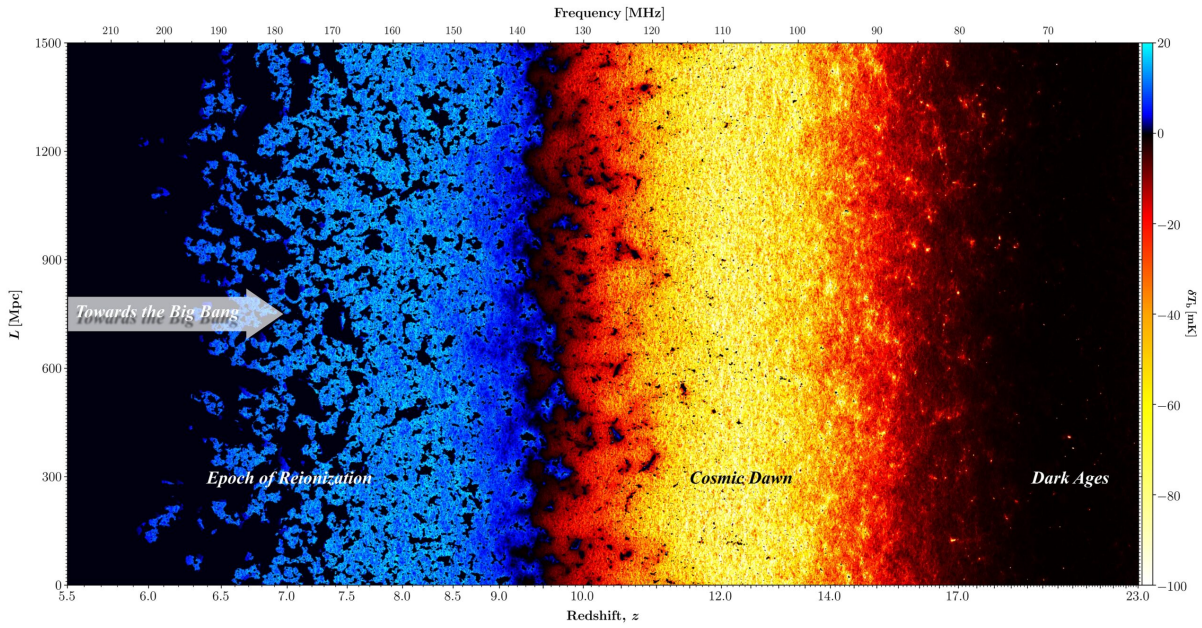

Figure 1.3: Redshift evolution of the 21 cm signal computed with the code 21cmFast (Mesinger et al., 2011). Credit: Andrei Mesinger.

perturbations become non linear. The combination of the above equations yields to leading order in δ (Loeb, 2010):

$$\frac{\partial \delta^2}{\partial t^2} + 2H\frac{\partial \delta}{\partial t} = \delta 4\pi G\rho_0. \tag{1.43}$$

The initial perturbation amplitude varies with spatial scale. Large-scale regions have a smaller perturbation amplitude than small-scale regions. The statistical properties of the perturbations as a function of spatial scale can be captured by expressing the density field as a sum over a complete set of periodic Fourier modes, each having a sinusoidal (wave-like) dependence on space with a comoving wave number k. Mathematically, we write:

$$\delta_k = \frac{1}{V}\int \delta(x) e^{-ikx} d^3x, \tag{1.44}$$

with x being the comoving spatial coordinate.

Inflation generates perturbations in which different k-modes are statistically independent, and each with a random phase constant in its sinusoid. The statistical properties of the fluctuations are determined by the variance of the different k-modes given by the so-called power spectrum:

$$P(k) = V\langle|\delta_k|^2\rangle, \tag{1.45}$$

where the angular brackets denote an average over the entire statistical ensemble of modes. In the standard cosmological model, inflation produces a primordial power-law spectrum $P(k) \propto k$. This spectrum has the special property that gravitational potential fluctuations of all wavelengths have the same amplitude at the time when they enter the horizon (namely, when their wavelength matches the distance traveled by light during the age of the Universe), and so this spectrum is called "scale invariant".

For modes with random phases, the probability of different regions with the same size to have a perturbation amplitude between δ and $\delta + d\delta$ is Gaussian with a zero mean and the above variance:

$$P(\delta) = \frac{1}{\sqrt{2\pi}\sigma} e^{-\delta^2/2\sigma^2}. \tag{1.46}$$

The small density fluctuations observed in the CMB gradually increase over time until the perturbation δ reaches the order of unity. At this point, the problem becomes fully non-linear and requires a complete gravitational analysis. This change in the regime of the perturbation is used to describe the formation of dark matter halos. A dark matter halo is a spherical distribution of dark matter particles that envelops galaxies, dominating their mass and influencing their gravitational potential. DM halos affect the rotation curves of galaxies and the dynamics of galaxy clusters, playing a crucial role in the formation and evolution of cosmic structures. When a density perturbation crosses the threshold value $\delta_c(z) = 1.686/D(z)$, the dark matter enclosed in that region stops expanding with the Universe to collapse into an halo. The growth factor $D(z)$ is used to compute the evolution with redshift of the critical density (δ_c) that was computed at $z = 0$ (Peebles, 1993).

An halo of mass M_h collapsing at redshift z is described by a virial radius (Barkana & Loeb, 2001):

$$r_{\rm vir} = 0.784 \left(\frac{M_{\rm vir}}{10^8\ h^{-1}\ M_\odot}\right)^{1/3} \left[\frac{\Omega_m}{\Omega_m^z}\frac{\Delta_c}{18\pi^2}\right]^{-1/3} \left(\frac{1+z}{10}\right)^{-1} h^{-1}\ {\rm kpc}, \tag{1.47}$$

where

$$\Omega_m^z = \frac{\Omega_m(1+z)^3}{\Omega_m(1+z)^3 + \Omega_\Lambda + \Omega_k(1+z)^2}, \tag{1.48}$$

and $\Delta_c = 18\pi \simeq 178$ is final overdensity relative to the critical density at the collapse redshift. This correspond to a circular velocity:

$$V_c = 23.4 \left(\frac{M_{\rm vir}}{10^8\ h^{-1}\ M_\odot}\right)^{1/3} \left[\frac{\Omega_m}{\Omega_m^z}\frac{\Delta_c}{18\pi^2}\right]^{1/6} \left(\frac{1+z}{10}\right)^{1/2} h^{-1}\ {\rm km/s}, \tag{1.49}$$

and consequently a virial temperature:

$$T_{\rm vir} = 1.9 \times 10^4 \left(\frac{\mu}{0.6}\right) \left(\frac{M_{\rm vir}}{10^8\ h^{-1}\ M_\odot}\right)^{2/3} \left[\frac{\Omega_m}{\Omega_m^z}\frac{\Delta_c}{18\pi^2}\right]^{1/3} \left(\frac{1+z}{10}\right) {\rm K}, \tag{1.50}$$

where μ is the mean molecular weight.

Besides the characterization of the properties of single dark matter halos, it is also possible to predict the number density of halos as a function of mass and redshift. This quantity is called halo mass function (HMF), and it is obtained in the framework of a Gaussian random field for the density perturbations. To compute the abundance of halos, it is used the density field smoothed on a mass scale M (δ_M). The probability that δ_M is greater then the critical density for collapse (δ_c) can be computed as (Barkana & Loeb, 2001):

$$\int_{\delta_c}^{\infty} d\delta_M \frac{1}{\sqrt{2\pi}\sigma_M} \exp\left[-\frac{\delta_M^2}{2\sigma_M^2}\right] \tag{1.51}$$

where σ_M represent the standard deviation of the Gaussian random field. Integrating this expression results in the mass fraction of the Universe contained in halos with mass greater then a given mass M:

$$F(>M|z) = {\rm erfc}\left(\frac{\delta_c(z)}{\sqrt{2}\sigma}\right). \tag{1.52}$$

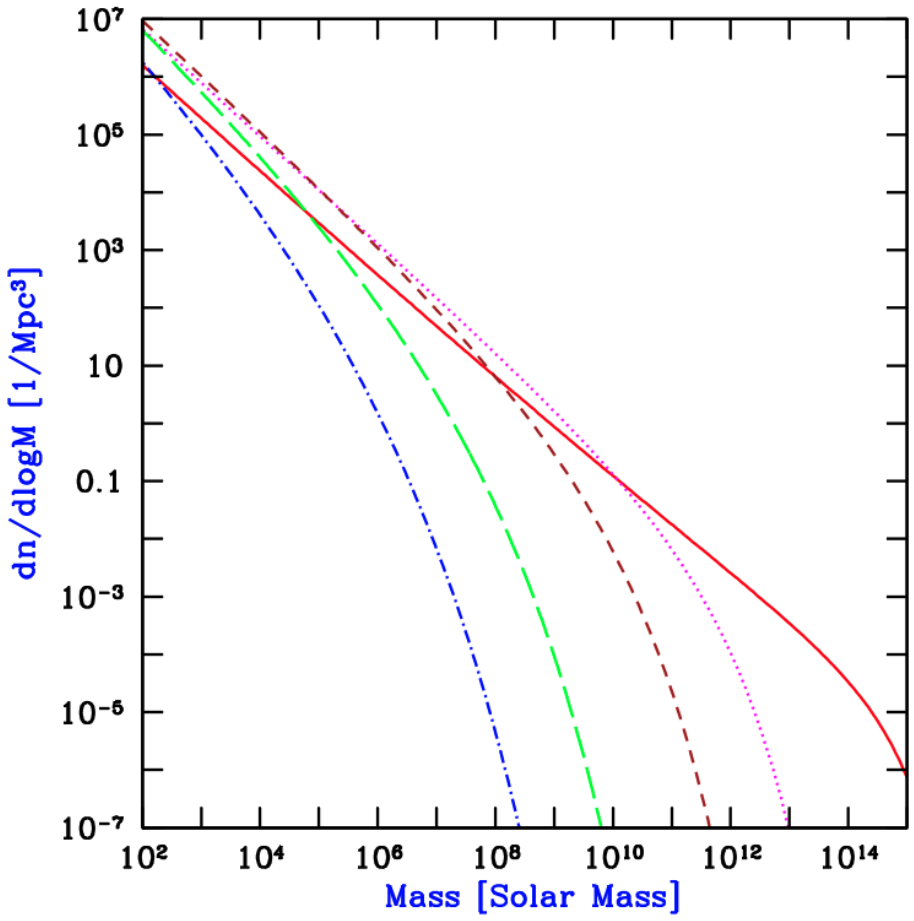

Figure 1.4: Halo mass function. Different lines show different redshift: $z = 0$ (red), $z = 5$ (magenta), $z = 10$ (brown), $z = 20$ (green), $z = 30$ (blue). Credit: Barkana & Loeb 2001.

Differentiating the fraction of dark matter in halos above a given mass, results in the abundance of halos in the mass interval M and $M + dM$:

$$\frac{dn_H}{dM} = \sqrt{\frac{2}{\pi}} \frac{\rho_m}{M} \frac{-d(\ln \sigma)}{dM} \nu_c e^{-\nu_c/2}, \tag{1.53}$$

where $\nu_c = \delta_c(z)/\sigma_M$ is the number of standard deviations which the critical collapse overdensity represents on mass scale M.

After the formation of the first dark matter halos, gas started to fall inside their gravitational potential. This process ultimately gave rise to the formation of the first stars and thus galaxies. The mass of the first baryonic structure can be predicted starting from the Jean's lenght, which represent the fundamental scale at which a perturbation can collapse:

$$\lambda_J = \frac{c_s}{\sqrt{\rho G}}, \tag{1.54}$$

where c_s is the sound speed of the gas, and ρ the gas density. This quantity translate into a mass (Barkana & Loeb, 2001):

$$M_J = 5.7 \times 10^3 \left(\frac{\Omega_m h^2}{0.15}\right)^{-1/2} \left(\frac{\Omega_b h^2}{0.022}\right)^{-3/5} \left(\frac{1+z}{10}\right)^{3/2} M_\odot, \tag{1.55}$$

where Ω_m is the matter energy density of the Universe, Ω_b is the baryon energy density of the Universe, and h is the reduced Hubble's constant. This quantity represent the minimum mass for baryonic structures in the Universe as a function of redshift.

In order to further collapse and form stars, baryons need to lose kinetic energy, and this is possible via radiative losses. Understanding the gas cooling processes in the primordial Universe is paramount in order to understand the birth of the first stars. We have different channels for primordial cooling:

1. radiative recombination: thermal energy loss of recombining proton and electron due to photon emitted in the process;

2. collisional ionization: thermal energy of electrons converted in ionization energy;

3. Bound-bound transition: thermal energy is converted into excitation energy of bound-states transitions;

4. thermal bremsstrahlung emission: radiation due to acceleration of a charge in a Coulomb field.

The effectiveness of these processes depends on the temperature (T) and density of the gas (n), as well as the chemical composition. In the primordial Universe, the gas is almost metal free, thus composed of hydrogen and helium. The first structures formed with a virial temperature of $T \sim 10^4$ K. Around this temperature range, hydrogen represent the most important coolant, as we show in Fig. 1.5. Below 10^4 K, the cooling function (red curve) present a sharp drop. To continue cooling the gas, and reach the temperature needed for star formation another mechanism is needed. This new channel is provided by molecular hydrogen (H_2, blue dashed curve). The two most important channels for H_2 formation in the early Universe are:

$$\begin{aligned} H + e &\rightarrow H^- + \gamma \\ H^- + H &\rightarrow H_2 + e, \end{aligned} \tag{1.56}$$

and

$$\begin{aligned} H + H^+ &\rightarrow H_2^+ + \gamma \\ H_2^+ + H &\rightarrow H_2 + H^+. \end{aligned} \tag{1.57}$$

When the condition for H_2 formation are met, the gas can cool below to $T \sim 10^3$ K to start the first star formation.

The first stars formed around $z \sim 30$. These are the Population III stars, which were very massive (upper limit $M_* < 10^3 \mathrm{M}_\odot$) and short-lived (few million years, Loeb 2010). Currently we have no direct observational constraints on first stars, in contrast to the wealth of observational data we have on the subsequent star formation history.

As soon as these first stars appeared the situation became more complex due to their feedback on the environment. In particular, supernova explosions dispersed the heavy elements produced inside the first generation of stars into the surrounding gas. Atomic and molecular cooling became much more efficient after the addition of these metals.

The youngest stars in the Milky Way galaxy, with the highest abundance of elements heavier than helium (referred to by astronomers as metals) were historically categorized as Population I stars. Older stars, with much lower metallicity, were called Population II stars, and the first metal-free stars are referred to as Population III. Early metal enrichment was likely the dominant effect that brought about the transition from Population III to Population II star formation.

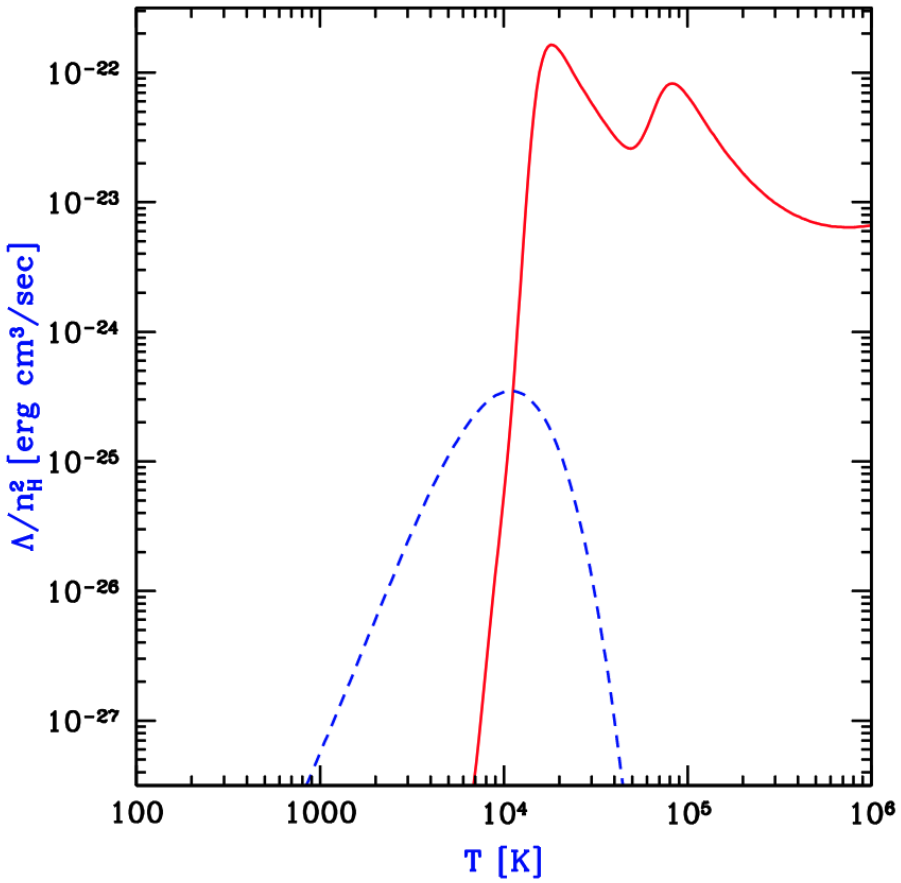

Figure 1.5: Cooling rate for primordial gas. The red continuous line represent the cooling for a gas composed of atomic hydrogen and helium. The blue dashed line shows the cooling rate for molecular hydrogen. Credit: Barkana & Loeb 2001.

Since massive stars produce ionizing photons much more effectively than low-mass stars (such as the Population II stars), the transition from Population III to Population II stars had important consequences for the ionization history of the cosmic gas.

1.2.5 Cosmic reionization

The Epoch of Reionization (EoR) refers to the period in the history of the Universe during which the predominantly neutral intergalactic medium was ionized by the emergence of the first luminous sources. These sources may have been stars, galaxies, quasars, or some combination of the above. By studying reionization, we can find the evolutionary links between the remarkably smooth matter distribution at early times revealed by CMB studies, and the highly structured Universe of galaxies and clusters of galaxies at redshifts $z \sim 6$ and below. In considering the process of ionization, in order to estimate the neutral fraction in the intergalactic medium, we have to take into account the two processes (Peebles, 1993):

- radiative transitions

$$H + \gamma \longleftrightarrow p + e \tag{1.58}$$

- ionization process

$$H + e \longrightarrow p + e + e \tag{1.59}$$

Let's first compute the electron capture rate $H + \gamma \longrightarrow p + e$. We have to imagine that a proton and an electron are placed in a dissipationless box and consider the probability of finding that the box contains a hydrogen atom and a photon. We can consider the kinetic of the proton to be negligible with respect to the one of the electron. The ratio of the probabilities P_h and P_p that the box is found to contain a hydrogen atom and photon, or proton and electron, is the ratio of the number of quantum states available to each case:

$$\frac{P_h}{P_p} = \frac{2p_\gamma^2 dp_\gamma}{p_e^2 dp_e} = \frac{\sigma_r \nu_e}{\sigma_{pi} c} \tag{1.60}$$

In the last expression there is the ratio of rates of recombination (σ_r) and ionization(σ_{pi}):

$$\frac{\sigma_r}{\sigma_{pi}} = \frac{2p_\gamma^2}{p_e^2} = \frac{\hbar^2 \omega^2}{c^2 p_e^2} \tag{1.61}$$

In astrophysics this expression is known as the Milne relation (Peebles, 1993). The rate of recombination reaction per unit volume is

$$\frac{dn_I}{dt} = \alpha n_e n_p \tag{1.62}$$

where, taken n_e and n_p as the number densities of electrons and protons, α is the recombination coefficient, the product of the electron capture cross section σ_r and the electron velocity averaged over a thermal distribution. At temperature $T \sim 10^4$ K the recombination coefficient is:

$$\alpha = 4 \cdot 10^{-13} T_4^{-0.7} [cm]^3 [s]^{-1}. \tag{1.63}$$

We now proceed to compute ionization rate. Two effects participate into this process: collisional ionziation and photoioniziation . The cross section for collisional ionization reaches its maximum value, $\sigma_{ci} \cong 2a_0^2$, where a_0 is the Bohr radius, at electron energy $\epsilon \sim 100$ eV (Peebles, 1993)). The equilibrium neutral fraction n_I/n_P thus is at its minimum value at $\epsilon \sim 100$ eV, corresponding to temperature $T \sim \epsilon/k \sim 10^6$ K, where

$$\sigma_{ci} \nu = 3 \cdot 10^{-8} \mathrm{cm}^3 \mathrm{s}^{-1}. \tag{1.64}$$

If the matter temperature were well below 100 eV, the dominant source of ionization could be electromagnetic radiation due to the presence of high redshift bright sources.

High redshift galaxies are expected to be the main cause for the reionization process. Ionizing photons escaping from the galaxies form ionized bubble (HII regions) in the surrounding IGM. The gas in the bubble is heated to the temperature of 10^4 K, and as time passes these bubbles expand. They grow until encounter each other, typically at $z \sim 6$, marking the end of the reionization epoch. Thus, given a number of ionizing photon that escape each galaxy ($N_{\rm ion}$), the evolution of the fraction of volume filled by ionized bubble ($Q_{H_{II}}$) can be estimated as (Barkana & Loeb, 2001):

$$\frac{dQ_{H_{II}}}{dt} = \frac{N_{\rm ion}}{0.76} \frac{dF_{\rm coll}}{dt} - \alpha_B \frac{C}{a^3} \bar{n}_H^0 Q_{H_{II}}, \tag{1.65}$$

where $F_{\rm coll}$ is the collapse fraction, C is the clumping factor, and $\bar{n}_H^0$ is the present days number density of hydrogen. In Fig. 1.6, we show the evolution of this quantity with redshift for different assumptions of the clumping factor.

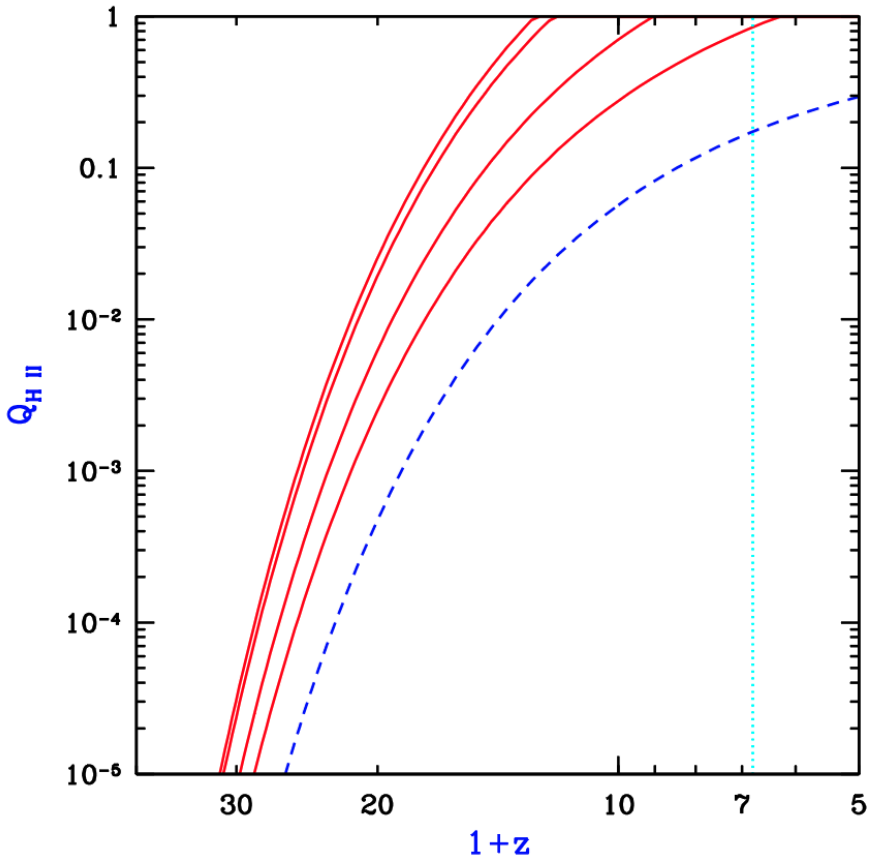

Figure 1.6: Filling factor ($Q_{H_{II}}$) evolution with redshift. Different lines show different assumption for the clumping factor. The vertical blue dotted line shows redshift $z = 5.8$ as a reference value for the end of the reionization. Credit: Barkana & Loeb 2001.

Cosmological backgrounds 2

In the previous chapter, we have discussed the Cosmic Microwave Background (CMB), resulting from the recombination process occurred at $z \sim 1100$. In this chapter, with the term "cosmological background" we refer to the integrated emission of all the extragalactic sources in a given energy band. In particular, we focus on the X-ray (CXB), radio (CRB) and near infrared (NIRB) backgorunds. Cosmological backgrounds retain important information about the large-scale structures of the Universe, and the properties of the sources from which they are originated.

2.0.1 X-ray background

The X-ray background (XRB) was first discovered by Riccardo Giacconi and colleagues in 1962. This discovery was part of a pioneering experiment that aimed to detect X-ray sources beyond the Sun. The experiment involved launching a rocket equipped with a Geiger counter to measure X-ray radiation. During the data analysis process, the team found a significant level of X-ray radiation coming from all directions in the sky, suggesting the presence of a diffuse background of X-rays. This discovery was groundbreaking as it indicated that X-rays were not only emitted by known celestial sources, such as the Sun, but also by a pervasive background radiation.

The findings from this experiment were published in the paper by Giacconi et al. 1962, which provided the first evidence of the CXB. This work laid the foundation for the field of X-ray astronomy, opening up a new window for observing the Universe. In recognition of his contributions to the discovery of cosmic X-ray sources and the X-ray background, Riccardo Giacconi was awarded a share of the Nobel Prize in Physics in 2002. His work has had a lasting impact on astrophysics, leading to numerous advances in our understanding of high-energy processes in the Universe.

The X-ray background (XRB) is an isotropic and diffuse radiation detected across the entire sky, consisting of X-rays with energies ranging from a few hundred eV to several hundred keV. The spectral intensity of the XRB, $I(E)$, as a function of energy E, can be approximated by a power-law distribution with an exponential cutoff at higher energies:

$$I(E) = I_0 \left(\frac{E}{E_0} \right)^{\Gamma} \exp \left(\frac{E}{E_c} \right), \tag{2.1}$$

where I_0 is the normalization constant, E_0 is a reference energy, Γ is the photon index (typically around 1.4 for the soft X-ray background), and E_c is the cutoff energy (often in the range of 30-40 keV for the high-energy background). The total intensity of the XRB can be integrated over the energy range to obtain the total flux:

$$F = \int I(E) dE. \tag{2.2}$$

The XRB is largely isotropic, but slight anisotropies are observed, indicating contributions from both resolved and unresolved sources. Deep surveys with X-ray telescopes such as Chandra and XMM-Newton have resolved a significant fraction of the XRB into discrete sources, primarily active galactic nuclei (AGNs, Fabian & Barcons, 1992; Moretti et al., 2003). The XRB can be decomposed into contributions from different types of sources, each dominating at different energy ranges. At low energies (0.5-2 keV), the XRB is primarily from unresolved distant AGNs and emission from hot gas in the intergalactic medium. In the medium energy range (2-10 keV), the XRB is a combination of AGNs, galaxy clusters, and hot gas in large-scale structures, with contributions from starburst galaxies and normal galaxies. At high energies (> 10 keV), the XRB includes contributions from more energetic processes, including non-thermal emissions from supernova remnants and black hole accretion, as well as X-ray binaries and other compact objects (Gilli et al., 2007). The distribution of source contributions can be modeled using population synthesis models, which combine the luminosity functions and evolution of different source populations to match the observed XRB spectrum (Brandt & Hasinger, 2005).

AGNs are some of the most powerful and luminous sources in the Universe, powered by the accretion of material onto supermassive black holes located at the centers of galaxies. This accretion process releases vast amounts of energy, including X-rays. AGNs contribute significantly to the soft X-ray background due to their high X-ray luminosity and large numbers. Observations indicate that most of the soft XRB can be attributed to a population of faint, distant AGNs (Treister & Urry, 2006) that are not individually resolvable. The X-ray spectra of AGNs typically exhibit a power-law form with a photon index $\Gamma \sim 1.4$ (Ueda et al., 2014). The intergalactic medium, which is the space between galaxies, contains hot, diffuse gas that emits X-rays through thermal bremsstrahlung and line emission from highly ionized atoms. This hot gas contributes to the soft X-ray background, particularly in regions of high-density gas associated with large-scale structures such as galaxy clusters and filaments. For example, studies like those by Nicastro et al. 2005 have highlighted the significance of the warm-hot intergalactic medium (WHIM) in contributing to the soft X-ray background, suggesting it could account for a significant portion of the missing baryons in the universe.

In the medium energy range, the X-ray background is a mix of contributions from AGNs, galaxy clusters, and hot gas in large-scale structures. Galaxy clusters, which are the largest gravitationally bound structures in the Universe, contain vast amounts of hot, intracluster gas that emits X-rays predominantly through thermal bremsstrahlung. These clusters contribute to the medium-energy XRB, particularly through the collective emission of numerous smaller, unresolved sources within the clusters. The X-ray spectrum of galaxy clusters is characterized by thermal emission with temperatures ranging from a few million to tens of millions of Kelvin, leading to a continuous spectrum with prominent emission lines (Voit, 2005).

At high energies, the X-ray background includes contributions from more energetic processes, including non-thermal emissions from supernova remnants and black hole accretion, as well as X-ray binaries and other compact objects. Supernova remnants are the remnants of exploded stars, containing shock-heated gas and accelerating particles to high energies. These remnants contribute non-thermal X-rays through synchrotron radiation and inverse Compton scattering. The spectrum from supernova remnants is typically characterized by a power-law distribution, reflecting the high-energy processes involved (Reynolds, 2008). Accretion onto stellar-mass black holes in X-ray binaries and onto supermassive black holes in AGNs produces high-energy X-rays. These processes dominate the hard X-ray background due to their extremely high luminosities and energetic emissions. The spectra of such sources are often power-law distributions with indices hardening at higher energies, sometimes featuring a high-energy cutoff (Mushotzky et al., 2000). X-ray binaries consist of a normal star and a compact object, such as

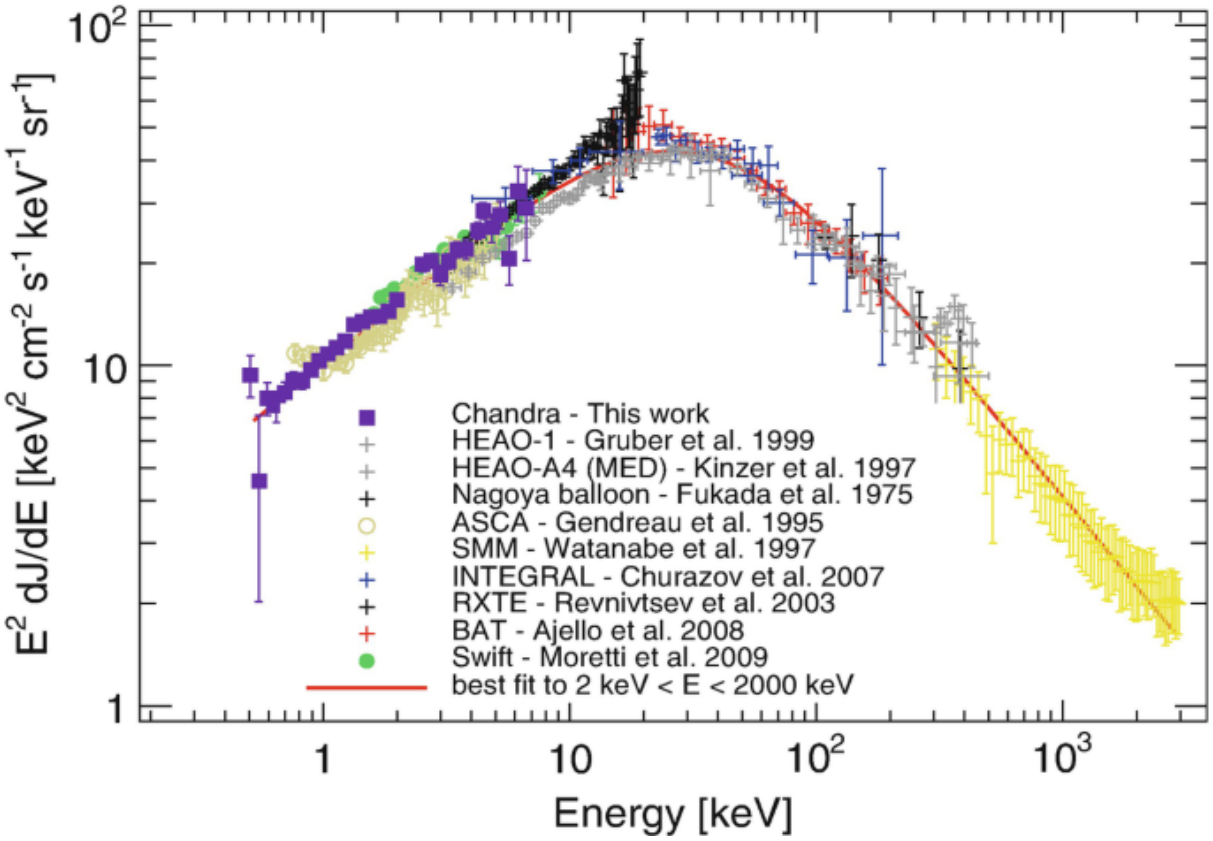

Figure 2.1: X-ray background intensity. Colored squares represent measurement from different works as described in the figure. The red continuous line is the best fit for the data. Credit: Cappelluti et al. 2017.

a neutron star or black hole, where material from the star is accreted onto the compact object, emitting X-rays. These binaries contribute to the high-energy XRB through their bright, variable X-ray emissions. The X-ray spectrum of binaries is typically complex, often showing thermal components from the accretion disk and non-thermal components from Comptonized coronae (Remillard & McClintock, 2006).

The observation of the cosmic X-ray background (CXB) excess, particularly in the hard X-ray band, has been a significant focus of high-energy astrophysics. This excess refers to the portion of the X-ray background that cannot be fully explained by the known populations of X-ray sources, such as active galactic nuclei (AGNs), galaxy clusters, and star-forming galaxies Cappelluti et al. 2017. After subtracting the population of known sources, observation of the X-ray background with Chandra reported an ammount of total light from unresolved soruces of $I_{0.5-2\ \mathrm{keV}} = 2.90 \times 10^{-12}\mathrm{erg\ s^{-1}\ cm^{-2}\ deg^{-2}}$ in the soft X-ray band, and $I_{2-10\ \mathrm{keV}} = 6.47 \times 10^{-12}\mathrm{erg\ s^{-1}\ cm^{-2}\ deg^{-2}}$ in the hard band. This represent roughly $10\ \%$ of the total XRB, while another $1\ \%$ can be attributed to unkown sources: $I_{0.5-2\ \mathrm{keV}} = 0.97 \times 10^{-12}\mathrm{erg\ s^{-1}\ cm^{-2}\ deg^{-2}}$ in the soft X-ray band, and $I_{2-10\ \mathrm{keV}} = 3.45 \times 10^{-12}\mathrm{erg\ s^{-1}\ cm^{-2}\ deg^{-2}}$ in the hard band.

Typically, this excess is attributed to a population of high-redshift accreting BHs not yet detected. Deep surveys and population synthesis models suggest that there may be a population of AGNs that remain undetected or unresolved in current observations. These AGNs could contribute significantly to the hard X-ray excess (Ueda et al., 2014; Cappelluti et al., 2017).

2.0.2 Radio Background

The cosmic radio background (CRB) refers to the diffuse radio emission observed across the universe, encompassing all radio wavelengths and arising from numerous astrophysical sources. This phenomenon is distinct from the cosmic microwave background (CMB), which specifically pertains to the relic radiation from the Big Bang. The study of the CRB began in the 1930s with Karl Jansky, who is often considered the father of radio astronomy. Jansky discovered radio waves emanating from the Milky Way, marking the first detection of cosmic radio emissions (Jansky, 1933). This groundbreaking discovery was followed by Grote Reber in the 1940s, who constructed the first dedicated radio telescope and created the first maps of the radio sky, identifying sources beyond our galaxy (Reber, 1944).

The advancement of radio telescopes has significantly enhanced our understanding of the CRB. Instruments like the Very Large Array (VLA), the Parkes Observatory, and the Atacama Large Millimeter/submillimeter Array (ALMA) have provided detailed observations of the radio sky (Condon et al., 1998; Norris et al., 2011). Extensive surveys, such as the Westerbork Northern Sky Survey (WENSS) and the Low-Frequency Array (LOFAR), have mapped the radio background with high precision, revealing the complexity and richness of the CRB (Rengelink et al., 1997; van Haarlem et al., 2013). The CRB includes contributions from a variety of astrophysical sources. Galaxies, particularly active galactic nuclei (AGN) and star-forming regions, are significant contributors to the CRB (Condon, 1992). Additionally, supernova remnants and pulsars emit radio waves that add to the background (Green, 2019). There is also a theoretical possibility that annihilations or decays of dark matter particles contribute to the CRB (Hooper & Goodenough, 2011). Cosmic rays interacting with interstellar matter also produce diffuse radio emissions. One of the significant challenges in studying the CRB is distinguishing it from local radio emissions, known as the foreground. Techniques such as multi-frequency observations and modeling of known foreground sources are employed to isolate the true CRB (de Oliveira-Costa et al., 2008).

In 2012, Fixsen et al. 2011 identified an unexpected excess in the CRB, which suggested that the observed radio background is significantly higher than what can be accounted for by known sources. This excess was detected using data from the ARCADE2 (Absolute Radiometer for Cosmology, Astrophysics, and Diffuse Emission) balloon experiment and other radio surveys. In (Condon et al. (2012)) is analyzed a balloon measurement of absolute sky brightness that reported a value of $T_b = 54 \pm 6\mathrm{mK}$ at $\nu = 3.3\mathrm{GHz}$. This result was used, together with previous ones, to fit this radio-excess with a power-law spectrum between 22 MHz and 10 GHz

$$T_b = (24 \pm 2.1\mathrm{K}) \times \left(\frac{\nu}{310\mathrm{MHz}}\right)^{-2.599\pm0.036} . \tag{2.3}$$

This power-law gives 480 mK at 1.4 GHz(Condon et al., 2012). This value is in strong disagreement with its theoretical prevision from the model given in the work by Condon 1984. This is an evolutionary model for the total source count at 1.4 GHz in which radio source are primarily powered by AGNs elliptical galaxies. The prevision that this model gives is $T_b \approx 100$ mK, roughly 5 times lower then the observed value. This excess can again be explained with an early population of accreting black holes.

The EDGES experiment

EDGES's (The Experiment to Detect the Global Epoch of Reionization Signature) observations are single dipole measurements of the sky-averaged global signal of the 21 cm radiation, in order to trace the volume-averaged ionization and thermal histories in time. The experiment has

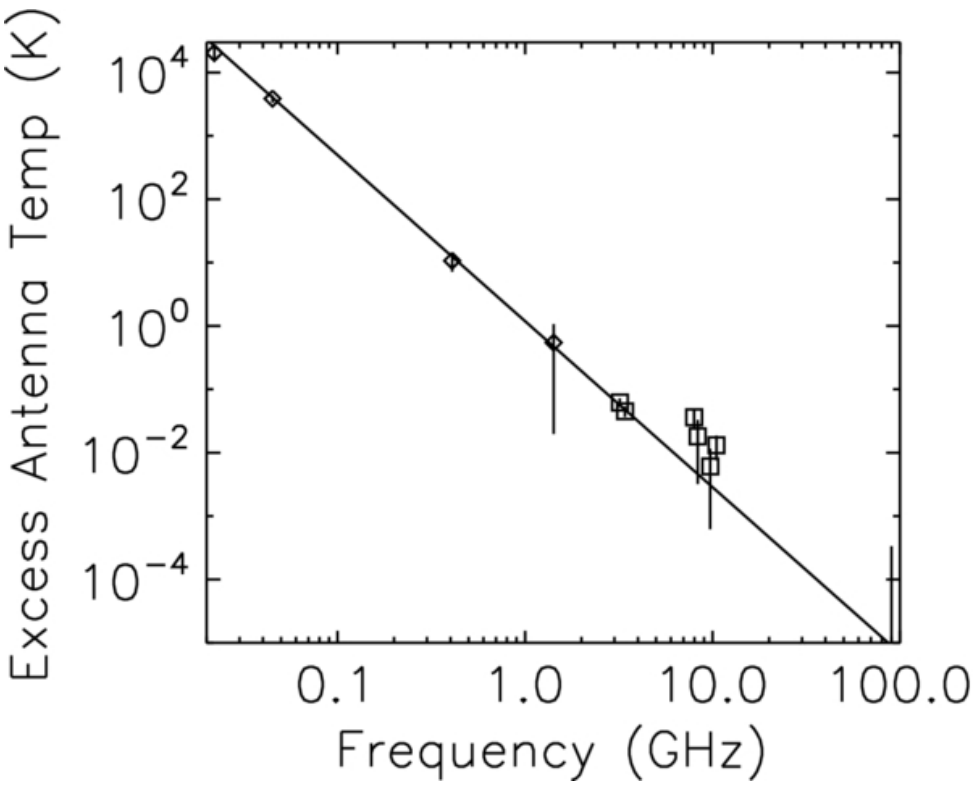

Figure 2.2: Temperature background intensity in the radio band. Empty squares represent the measurements conducted with the ARCADE2 experiment. The black continuous line is the best fit for the data. It shows a spectral index $\nu = -2.62$ typical of the synchrotron emission. Credit: Fixsen et al. 2011.

reported the detection of a strong absorption signal (see Fig. 2.3) that raised a strong interest in the community.

There are 3 unexpected and extremely interesting aspects of this observation:

- the depth of the signal
- the redshift at which the signal is centered
- the regular flat shape at the bottom

The observed depth of the signal is almost twice as deep as if the only contribute present in the background is given by the CMB. Recalling the expression for δT_b:

$$\delta T_b \propto \left(1 - \frac{T_{\rm CMB} + T_{\rm rad}}{T_{\rm spin}}\right) \tag{2.4}$$

there are two alternative in trying to justify this evidence: the first one is that $T_{\rm spin}$ has a lower value then expected at the redshift $z \sim 17$, an hypothesis explored in different works (Barkana, 2018; Muñoz & Loeb, 2018; Fialkov et al., 2018); the second one is the presence of different contribution in the radio background beside the CMB, hypothesis suggested already in the original paper regarding EDGES from (Mirocha & Furlanetto, 2019) and other works (Ewall-Wice et al. (2018), Ewall-Wice et al. (2019)).

2.0.3 Near Infrared Background

The Near Infrared Background (NIRB) is the diffuse radiation of cosmological origin observed after subtracting the local foregrounds in the band 1–10 μm (Kashlinsky et al., 2018). Since

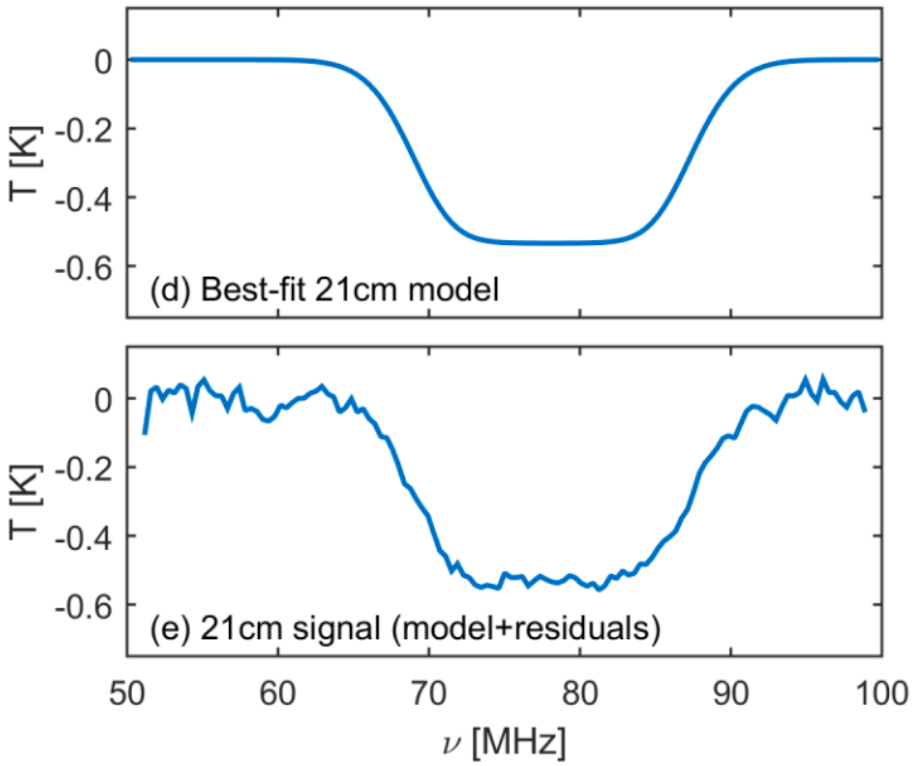

Figure 2.3: Upper panel: best fit model for the brightness temperature of the 21-cm radiation measurement reported by the EDGES experiment. Lower panel: best fit model, including residuals, for the brightness temperature of the 21-cm radiation measurement. Credit: Bowman et al. 2018.

early studies by Partridge & Peebles (1967), the NIRB has been considered a valuable tool to investigate the emission from the first stars and galaxy populations, as ultraviolet (UV) and optical light from high-z sources is redshifted to the near-infrared band.

Actual measurements of the mean NIRB intensity (Tsumura et al., 2013; Matsumoto et al., 2015; Sano et al., 2015; Matsuura et al., 2017) give a lower bound $I \gtrsim 10$ nW m^{-2}sr^{-1}, in excess with respect to the contribution of known galaxy populations derived from galaxy number counts (Driver et al., 2016). However, direct measurements of the NIRB suffer from large uncertainties due to the subtraction of foregrounds (Leinert et al., 1998), namely interplanetary dust emission (zodiacal light), galactic stars light and galactic interstellar medium radiation (cirrus).

Being foregrounds smooth, a more robust technique is computing the power spectrum of NIRB fluctuations (Kashlinsky et al., 1996; Kashlinsky & Odenwald, 2000), to which foregrounds contribution is limited. Moreover, from the power spectrum measurements, a lower limit to the I_ν contribution from unknown sources can be derived (Kashlinsky et al., 2007). The latest measurements of the NIRB power spectrum (Cooray et al., 2012a; Kashlinsky et al., 2012) established an excess power on scales larger then $\gtrsim 1$ arcmin, irreconcilable with emission from known galaxies up to $z \sim 5$ (Helgason et al., 2012). The origin of such a signal is still unknown.

Population III stars (PopIII) were one of the first hypothesis proposed about the sources of the NIRB excess (Santos et al., 2002; Salvaterra & Ferrara, 2003). Although intriguing, this idea was soon after discarded because of the very high formation efficiency required (Madau & Silk, 2005) and since it would overpredict the number of high-z dropout galaxies (Salvaterra & Ferrara, 2006). Several works explored the possibility of high redshift galaxies ($z \gtrsim 5$) being the sources of the NIRB excess, but models failed to reproduce the required levels of fluctuations (Fernandez et al., 2010; Cooray et al., 2012b; Yue et al., 2013; Helgason et al., 2016).

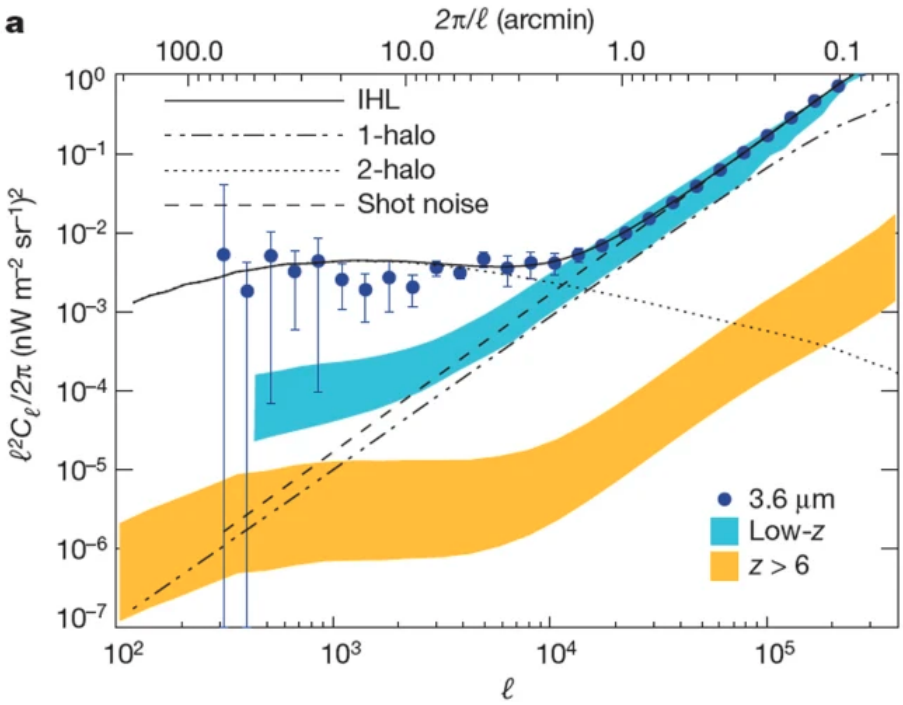

Figure 2.4: Near infrared background angular power spectrum. Blue dots show measurements reported by the experiment Spitzer. Credit: Cooray et al. 2012a.

An alternative solution was the intrahalo light (IHL), i.e light from stars stripped from their parent galaxy (Cooray et al., 2012a; Cheng & Bock, 2022). Despite its success in reproducing observations, such idea has to rely on poorly understood abundance of intrahalo stars (Ferrara, 2012). Moreover, this model cannot account for the observed cross-correlation of the NIRB with the soft-X background (SXB) (Cappelluti et al., 2013; Cappelluti et al., 2017). Such a feature is difficult to explain even with galaxies spectra, but could be naturally justified by X-ray emission from accretion disks around black holes. Yue et al. (2013) developed a model to explain both NIRB fluctuations and NIRB-SXB cross correlation with accreting direct collapse black holes (DCBHs), even though it is unclear whether the specific conditions of DCBHs formation are actually realized during cosmic evolution (Latif & Ferrara, 2016).

Supermassive black holes 3

Understanding the origin of supermassive black holes (SMBHs), namely BHs with masses $10^6 - 10^{10} M_\odot$, located at the centers of massive ($M_* \sim 10^9 - 10^{13} M_\odot$) galaxies is one of the hottest topics in Astrophysics. The existence of BHs with masses $> 10^6 M_\odot$, were firstly suggested in the 1960s (Salpeter, 1964). A key milestone was the discovery of Sagittarius A* (Eckart & Genzel, 1996), the SMBH at the Milky Way's center, through radio astronomy. Through the measurements of high-velocity orbits of nearby stars, the mass of Sagittarius A* was predicted to be about $4 \times 10^6\ M_\odot$ (Ghez et al., 2008; Gillessen et al., 2009). The presence of SMBHs in the center of galaxies is now supported by a variety of observational techniques that have provided robust evidence for their existence.

3.1 Observations in the local Universe

The existence of SMBHs can be inferred in several ways. One of the primary methods used to detect SMBHs is stellar dynamics. This technique involves the analysis of the motions of stars near the galactic center. In many galaxies, stars are observed to orbit around a central object with velocities that can only be explained only by the presence of a SMBH. Similarly to the case of Sagittarius A*, these methods have been employed in other galaxies, confirming the presence of SMBHs based on the gravitational influence they exert on nearby stars (Gebhardt et al., 2000; Gültekin et al., 2009; Kormendy & Ho, 2013).

Gas dynamics is another powerful tool for identifying SMBHs. This approach is based on the analysis of the dynamics of gas clouds within galaxies. Similarly to stars, gas clouds exhibit high-velocity motions when they are close to an SMBH. By measuring these velocities and modeling the gravitational influence required to explain them, the presence and mass of the central black hole can be inferred (Onken et al., 2004; Peterson et al., 2004; Ferrarese & Ford, 2005). For example, observations of emission lines arising from ionized gas in the cores of galaxies have shown velocities indicating the influence of massive central black holes on the surrounding medium (Kormendy & Ho, 2013).

The direct confirmation of the existence of SMBHs has been obtained recently thanks to the Event Horizon Telescope (EHT), an array of radio telescopes located in different parts of the globe. In the 2019, the EHT collaboration achieved one of the most recent groundbreaking results in this field, by releasing the first direct image of the event horizon surrounding the SMBH hosted by the galaxy M87. This results provided the first visual evidence of a black hole and its surrounding accretion disk (Event Horizon Telescope Collaboration et al., 2019). This image showed the "shadow" of the black hole, surrounded by a glowing ring of accreting matter, marking a significant milestone in black hole astronomy.

The exploration of SMBHs began with the discovery of quasars in the early 1960s. Quasars are the extremely luminous centers of galaxies powered by accretion onto SMBHs. The identification of the first quasar, 3C 273, by Maarten Schmidt in 1963 marked a significant milestone, revealing objects with exceptionally high redshifts, indicating they were both distant and ancient (Schmidt, 1963). The immense luminosity of quasars, some of which outshine entire galaxies, was soon attributed to the presence of SMBHs at their cores. Subsequent observations in the 1980s and 1990s, utilizing advancements in telescope technology and spectroscopy, allowed to measure the masses of these SMBHs. Surveys like the Palomar Sky Survey and the early stages of the Sloan Digital Sky Survey (SDSS) played crucial roles in discovering these distant quasars. These efforts provided the first hints that SMBHs with masses exceeding $10^9\ M_\odot$ existed within the first billion years after the Big Bang (Matthews & Sandage, 1963; Schmidt, 1963). Further groundbreaking work in the 1990s and early 2000s by Magorrian et al. 1998 and Gebhardt et al. 2000 established the correlation between SMBHs and their host galaxies.

3.1.1 The local $M_{\rm BH} - M_\star$ relation

The correlation between the mass of supermassive black holes (SMBHs) and the stellar mass of their host galaxies, particularly the bulge component, is crucial to understand galaxy formation and evolution. This relationship, often referred to as the $M_{\rm BH} - M_\star$ relation, provides critical insights into the co-evolution of galaxies and their central black holes.

Several observational works show a relation between the central SMBH and its host galaxy (Magorrian et al., 1998; Gebhardt et al., 2000; Kormendy & Ho, 2013). This relation also provide an useful way to measure the SMBH mass using an observational quantity which is much easier to measure. The scaling relation has a typical functional form (Ferrarese & Merritt, 2000):

$$\log(M_{\rm BH}/M_\odot) = \alpha + \beta \log(M_\star) \tag{3.1}$$

where α and β, are determined observationally.

Reines & Volonteri 2015 provide a comprehensive study of quasars masses in the local Universe ($z \leq 0.055$), and their stellar counter-parts. This study represent the state of the art for the local $M_{\rm BH} - M_\star$ relation, and is based on a sample of 262 AGNs and 79 galaxies with dynamical BH mass measurements. In Fig. 3.1, we show the plot from their original work. Fitting the data gave the relation:

$$\log(M_{\rm BH}/M_\odot) = 7.45(\pm 0.08) + 1.05(\pm 0.11) \log(M_\star/10^{11}\ M_\odot). \tag{3.2}$$

From this result, it is clear that in the local Universe the central SMBH is always undermassive ($\sim 0.1\%$) with respect to the stellar counterpart.

3.2 Observations at the epoch of reionization

The observational confirmation of the presence quasars during the epoch of reionization is a milestone for modern cosmology. High-z quasars provide insights into the formation and growth of supermassive black holes in the early Universe and help investigate the processes that ionized the intergalactic medium, shaping the large-scale structure of the cosmos.

3.2.1 Quasars at $z \sim 6$

Between 2006 and 2010, the field of cosmological exploration underwent a transformative period due to significant advancements in observational technology and large-scale surveys. The

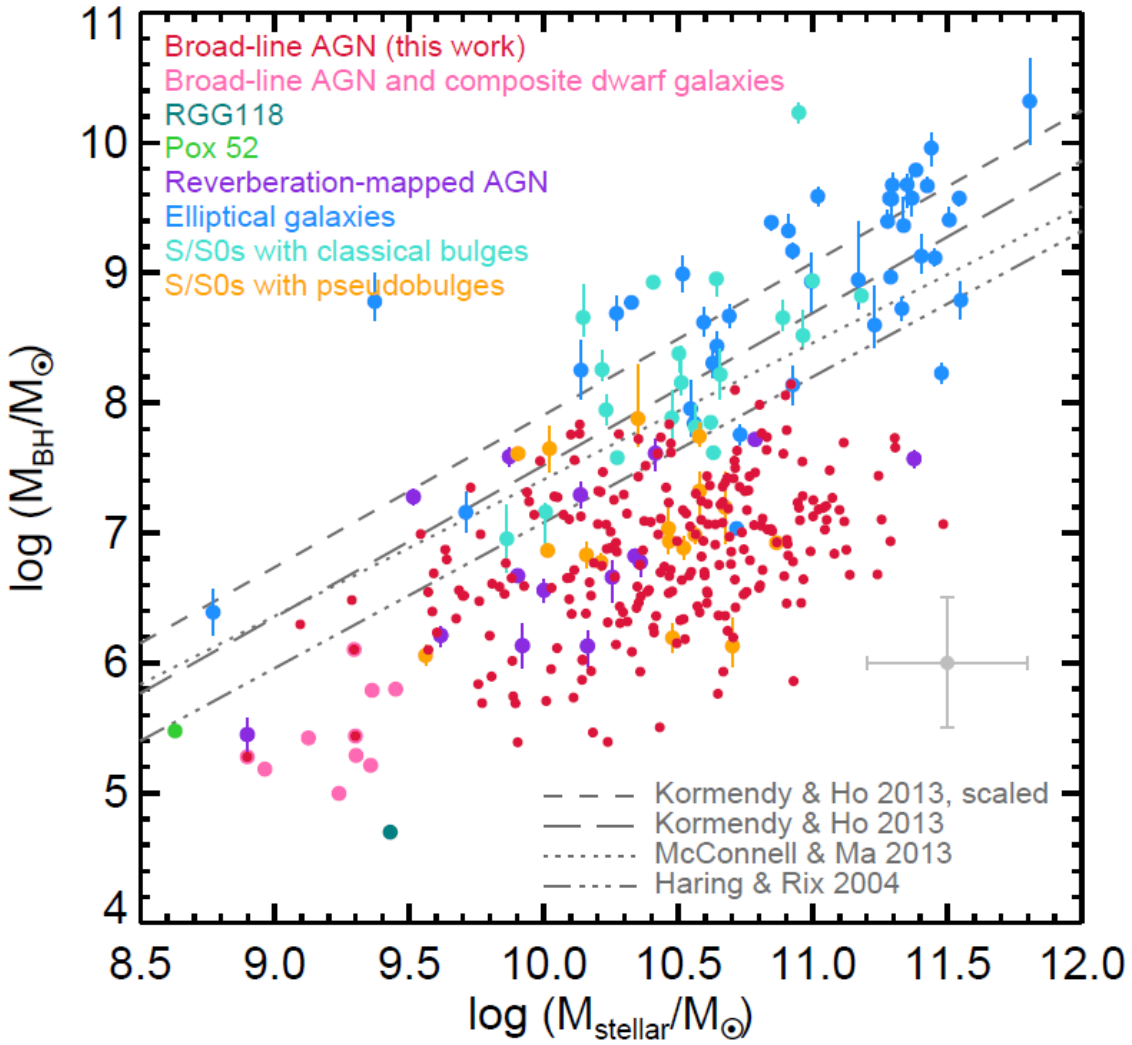

Figure 3.1: Black hole mass versus host galaxy stellar mass. Each color represent a different measurement method, as described in the legend. The grey lines show previously existing $M_{\rm BH} - M_\star$ relations. Credit: Reines & Volonteri 2015.

Sloan Digital Sky Survey (SDSS) was particularly instrumental during this era. The SDSS, with its large-scale imaging and spectroscopic surveys, enabled the identification of numerous high-redshift quasars, pushing the boundaries of known cosmic distances. In a landmark paper, Fan et al. 2006 presented a sample of 19 quasars at redshifts up to $z \sim 6$, showcasing the existence of SMBHs in the early Universe. These quasars, observed less than a billion years after the Big Bang, provided crucial insights into the early growth and evolution of SMBHs. Follow-up studies with ground-based telescopes, such as the Keck Observatory and the Very Large Telescope (VLT), confirmed the existence of SMBHs in these high-redshift quasars, providing further evidence for their early formation. These observations also included detailed spectroscopic analyses that revealed the chemical composition and physical conditions of the early Universe (Kurk et al., 2007; Willott et al., 2007). The success of the SDSS inspired additional surveys, such as the Canada-France High-z Quasar Survey (CFHQS) and the UKIRT Infrared Deep Sky Survey (UKIDSS), further expanding the catalog of high-redshift quasars. These surveys employed advanced imaging techniques and deep spectroscopy to uncover even more distant quasars, enhancing our understanding of SMBH demographics and their environments in the early universe Willott et al. (2010); Mortlock et al. (2011).

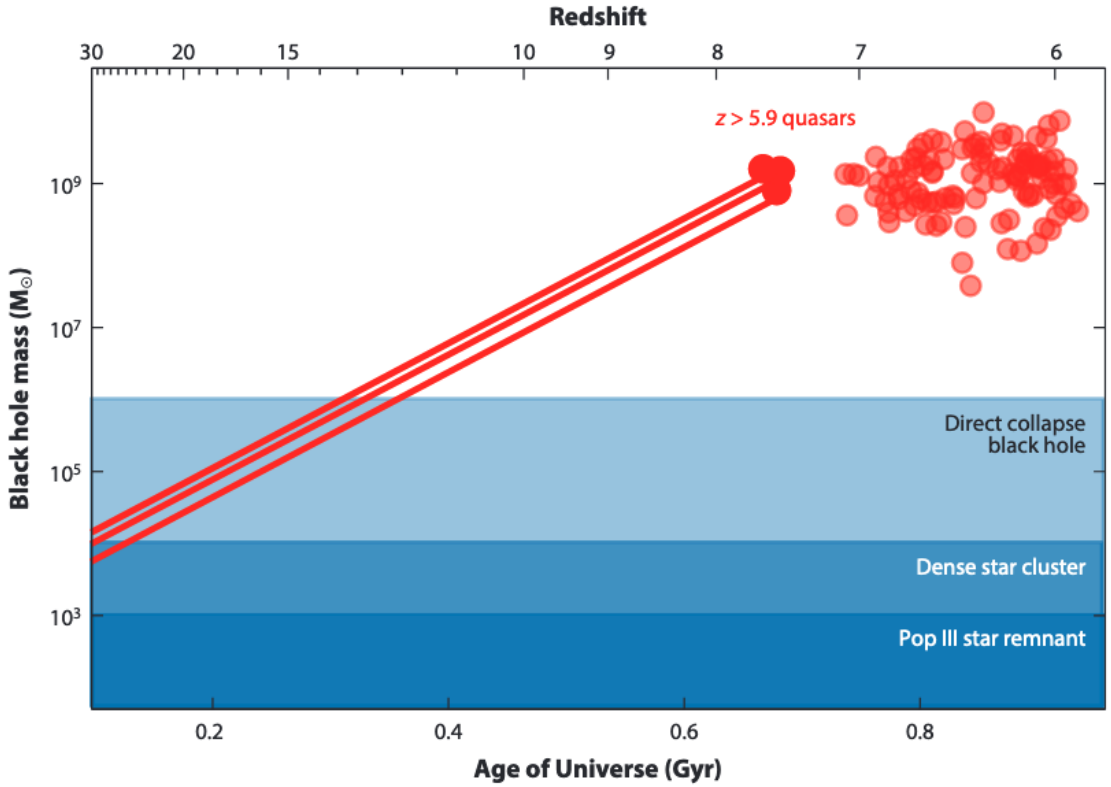

Figure 3.2: Supermassive black holes mass growth. Red circles represent observed $z \geq 5.9$ quasars. The red continuous lines represent the BH mass assembly assuming a constant Eddington accretion. The shaded blue regions show different seeding scenarios. Credit: Fan et al. 2023.

In the years leading up to the launch of the James Webb Space Telescope (JWST), continued to make significant strides in observing high-redshift SMBHs. Ground-based telescopes, such as the Very Large Telescope (VLT) and the Keck Observatory, played crucial roles in these discoveries. Through meticulous observational campaigns and spectroscopic analyses, researchers expanded the catalog of high-redshift quasars, providing valuable insights into the early Universe's SMBH population. A notable discovery during this period was the identification of quasar J1342+0928 at redshift $z = 7.54$, the most distant quasar known at the time. This quasar, powered by an SMBH with a mass of approximately $8 \times 10^8\ M_\odot$, was observed just 690 million years after the Big Bang (Bañados et al., 2018). The discovery of such distant quasars underscored the rapid growth of SMBHs in the early Universe and highlighted the importance of pre-JWST observations in advancing our understanding of SMBH formation and evolution. Additionally, other notable discoveries included the detection of several quasars at redshifts $z > 6.4$ by the UKIRT Infrared Deep Sky Survey (UKIDSS) and the Canada-France High-z Quasar Survey (CFHQS). These discoveries provided crucial data points for understanding the early growth and demographics of SMBHs (Willott et al., 2010; Mortlock et al., 2011). In Fig. 3.3, we show a compendium of the high redshift observed quasars in the last 20 years.

3.2.2 SMBH in the JWST era

The James Webb Space Telescope (JWST) has revolutionized our understanding of supermassive black holes (SMBHs) in the early universe. By observing the most distant and ancient quasars, JWST has provided critical data that challenge existing theories of black hole formation and growth. Recent JWST findings have identified SMBHs at redshifts $z \geq 10$, suggesting that

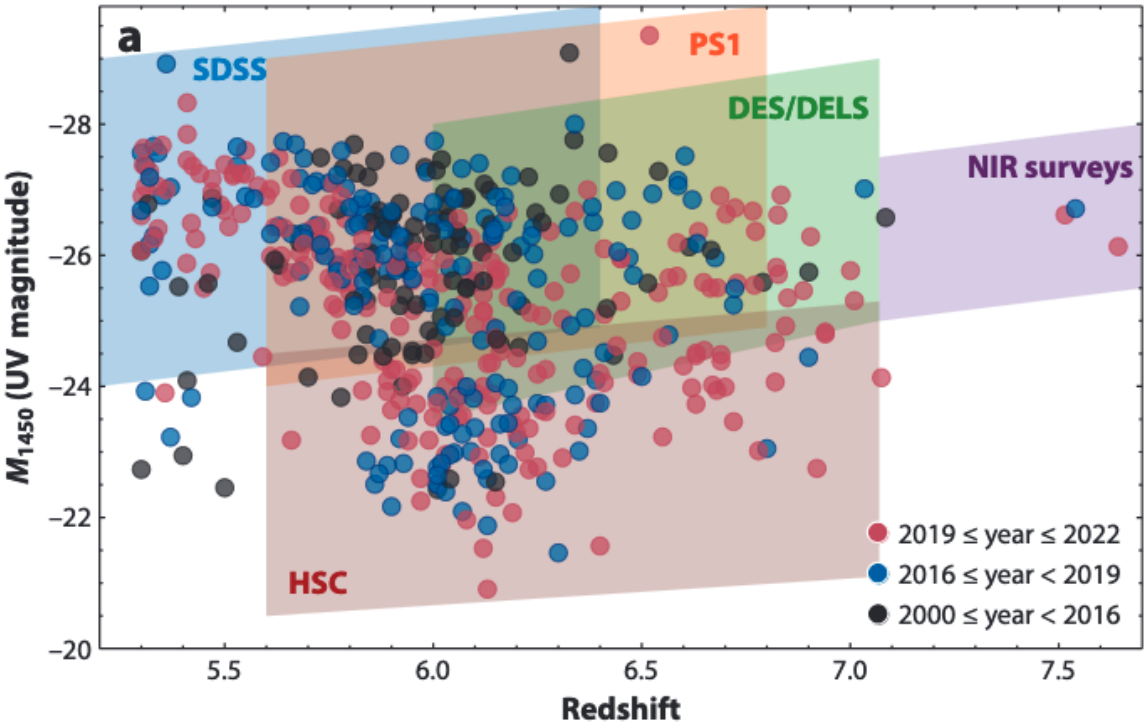

Figure 3.3: Distribution of all known Quasars at $z \geq 5.3$. Shaded region represent the parameter space probed by different quasar survey programs. Credit: Fan et al. 2023.

these massive objects were already in place within the first few hundred million years after the Big Bang. One of the landmark discoveries by JWST is the detection of SMBHs powering quasars at redshifts as high as $z \geq 10$. These observations indicate that SMBHs with masses of $M_{\rm BH} \geq 10^6\ M_\odot$ existed when the universe was less than 500 million years old, such as (GNz11 Maiolino et al., 2023).

In a groundbreaking study, Bogdan et al. 2023b reported the discovery of a quasar at $z = 10.3$, featuring an SMBH with a mass of approximately $10^8\ M_\odot$. The study reported the analyisis of X-ray data obtained with the Chandra instrument of a gravitationally lensed galaxy observed with JWST. X-ray data suggested the presence of an heavily obscured quasar with a bolometric luminosity of $L_B \sim 10^{45}\ {\rm erg\ s^{-1}}$. Moreover, previous JWST photometric data reported a stellar mass of $M_\star \simeq 10^8\ M_\odot$ for the galaxy, implying a BH to stellar mass ratio of order $O(1)$. This seems an unprecedented occurrence, and suggest a BH-stellar mass relation which is completely different to the one observed in the local Universe. Locally, the ratio $M_\bullet/M_\star$ is typically of order $0.1\ \%$ (Reines & Volonteri, 2015). The combination of the extremely high mass and high redshift challenges existing models of black hole growth due to the rapid accumulation of mass required to reach such sizes so early. It suggests that SMBH formation and growth must have been extremely efficient, possibly involving mechanisms such as direct collapse black holes (DCBHs) or super-Eddington accretion rates.

Kovacs et al. 2024a extended the previous work by identifying a second quasar at redshifts $z \geq 10$. This study reinforced the idea that the formation of SMBHs was not an isolated event. With a deep Chandra observation, the authors detected a candidate X-ray AGN which is spatially coincident with the JWST observed galaxy GHZ9. Similarly to the previous detection, the BH appear extremely massive ($\sim 10^(\ M_\odot$) given the observational redshift ($z \simeq 10.1$). The mass was inferred from the observed luminosity ($L_B \sim 10^{46}\ {\rm erg\ s^{-1}}$), assuming an Eddington accretion rate. In the last part of their study, the authors try to built the first AGN luminosity

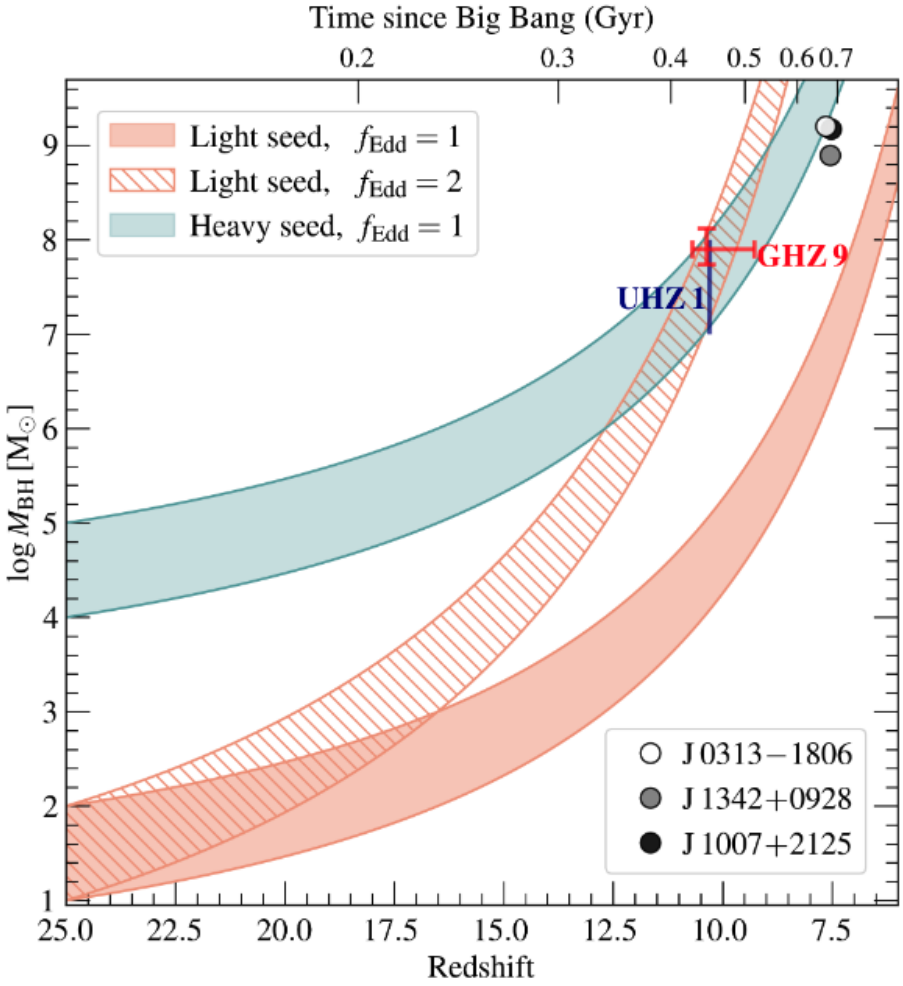

Figure 3.4: BH mass assembly for different seeding scenarios, and accretion rate. The two JWST observed black holes are showed in red and blue. The white, grey, and black dot represent the pre-JWST highest redsfhit ($z \sim 7.5$) quasars. Credit: Kovacs et al. 2024b.

functions at redshift $z \sim 10$. Despite the extremely small sample, this represent a starting point for future studies. By comparing their results with theoretical models of BH mass assembly, the author are able to claim that AGN number density at redshift $z \simeq 6.5 - 8$ is exceed theoretical prediction. Moreover, the discrepancy becomes even more noticeable at redshift $z \sim 10$, where the difference between theory and observations span several orders of magnitude. In Fig. 3.4, we show the mass of the two observed BH, as long few possible mass assembly scenario.

3.2.3 The $M_{\rm BH} - M_\star$ relation at high-z

Evidence for an evolution of the BH-stellar mass relation, pointing in the direction of overmassive black holes, has already been proposed (Pacucci et al., 2023). The authors suggest the possibility of a $M_{\rm BH}/M_\star$ ratio much higher at high-z, up to 10%. We show the collection of high-z ($4 < z < 7$) JWST data in Fig. 3.5. Their analysis results in the relation:

$$\log(M_{\rm BH}) = -2.43(\pm 0.08) + 1.06(\pm 0.09)\log(M_\star). \tag{3.3}$$

As this hypothesis remains speculative at the moment, due to the lack of a complete and unbiased sample, more and more evidence pointing in that direction are piling up. The presence of $\sim 10^{7-8}\ M_\odot$ black holes at such early epochs poses significant challenges to current models

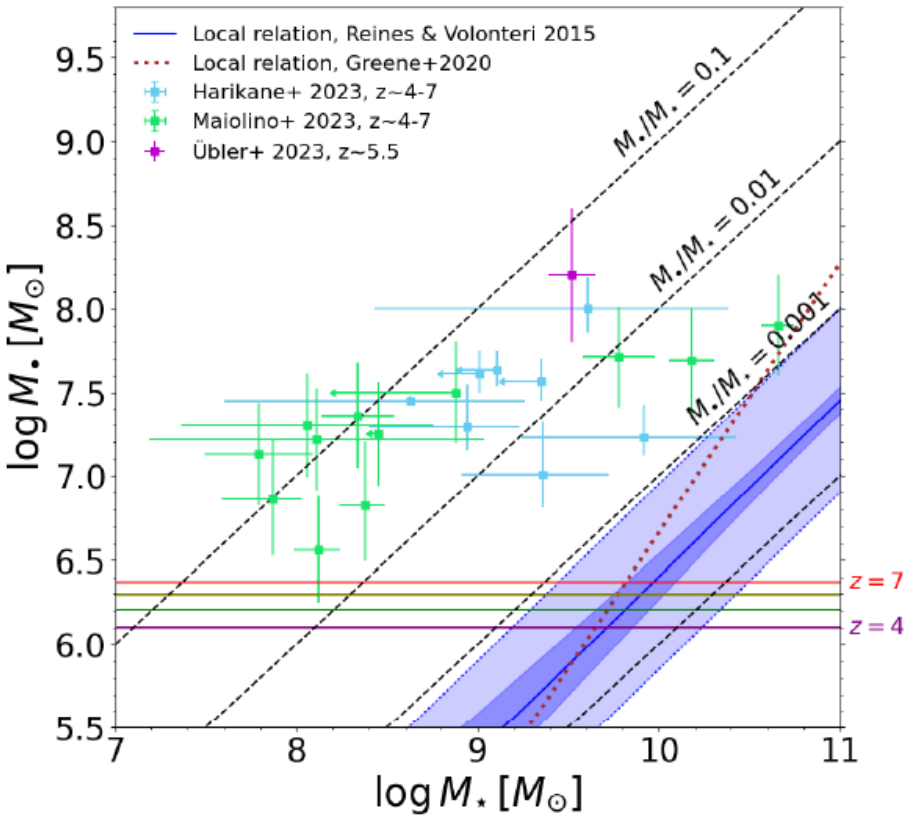

Figure 3.5: $M_{\rm BH} - M_\star$ relation at $z \geq 4$ in light of the new JWST data. Credit: Pacucci et al. 2023.

of black hole formation. Traditional scenarios, which propose that SMBHs grow from the remnants of Population III stars with masses around $10^2 - 10^3\ M_\odot$, are difficult to reconcile with the rapid growth rates implied by JWST observations. To achieve such massive growth within a few hundred million years, these black holes would need to accrete material at or near the Eddington limit continuously. The discoveries made by JWST are just the beginning. Future observations will aim to further characterize these early SMBHs and their host galaxies. JWST's extended mission will include monitoring quasar variability, which can provide insights into the accretion processes and the structure of the accretion disks. Additionally, studying the host galaxies in greater detail will help understand the relationship between SMBH growth and galaxy formation. JWST will also continue to push the observational frontier, potentially discovering even earlier SMBHs and providing a more complete picture of black hole formation in the first billion years of the universe. These observations will be crucial for refining theoretical models and understanding the feedback mechanisms that regulate black hole growth and galaxy evolution.

3.3 Supermassive black holes theoretical models

The discovery of supermassive black holes (SMBHs) at high redshifts presents significant challenges to our understanding of black hole formation and growth in the early Universe. The presence of SMBHs with masses exceeding $10^9\ M_\odot$ within the first billion years after the Big Bang demands an explanation of how these massive objects could form and grow so quickly. This has spurred a plethora of theoretical models and simulations, each grappling with the constraints imposed by the limited time available for their formation and the observed properties of the universe.

One of the primary constraints on SMBH growth is the Eddington limit, which describes the balance between the outward radiation pressure from accretion and the inward pull of gravity. The Eddington luminosity L_E is given by:

$$L_E = \frac{4\pi G M_{\rm BH} m_p c}{\sigma_T}, \tag{3.4}$$

where G is the gravitational constant, $M_{\rm BH}$ is the black hole mass, m_p is the proton mass, c is the speed of light, and σ_T is the Thomson scattering cross-section.

For a black hole of mass $M_{\rm BH}$, the Eddington accretion rate $\dot{M}_E$ can be derived using the radiative efficiency ε, which is the fraction of the accreted mass energy that is converted into radiation:

$$\dot{M}_E = \frac{L_E}{\varepsilon c^2}. \tag{3.5}$$

Assuming a typical radiative efficiency of $\varepsilon = 0.1$, the Eddington accretion rate becomes:

$$\dot{M}_E \simeq 2.2 \times 10^8 \left(\frac{M_{\rm BH}}{M_\odot}\right) M_\odot {\rm yr}^{-1}. \tag{3.6}$$

For a black hole, to grow from a stellar mass (typically associated to Population III stars remnant) to a supermassive scale (on the order of $10^9\ M_\odot$ within a few hundred million years, it would require sustained, near-Eddington or super-Eddington accretion rates. The growth of a black hole through accretion can be described by the equation:

$$M_{\rm BH}(t) = M_{\rm seed} {\rm exp}\left(\frac{1-\varepsilon}{\varepsilon}\frac{t}{t_E}\right), \tag{3.7}$$

where $M_{\rm seed}$ is the initial seed mass, and t_E is the Eddington timescale, given by:

$$t_E = \frac{\sigma_T c}{4\pi G m_p} \simeq 450 {\rm Myr}, \tag{3.8}$$

3.3.1 Seeds of SMBHs

Several scenarios have been proposed for the formation of SMBH seeds: *light seeds* ($M_{\rm seed} \sim 10 - 100\ M_\odot$), remnants of massive, metal-free (Population III) stars, originated in early ($z \sim 30$) mini-halos ($M_h \sim 10^6\ M_\odot$, e.g. Madau et al., 1998; Heger et al., 2003; Yoshida et al., 2006); *intermediate seeds* ($M_{\rm seed} \sim 10^{2-4}\ M_\odot$), produced by nuclear star clusters (NSC) in high redshift ($z \sim 15 - 20$) galaxies (e.g Devecchi & Volonteri, 2009; Davies et al., 2011; Lupi et al., 2014); *heavy seeds* ($M_{\rm seed} \sim 10^{4-6}\ M_\odot$), also called direct collapse black holes (DCBHs), formed through the collapse of atomic, pristine gas in high redshift ($z \sim 8 - 17$) atomic cooling ($M_h \gtrsim 10^8\ M_\odot$) halos (e.g. Eisenstein & Loeb, 1995; Silk & Rees, 1998; Ferrara et al., 2014).

Light seeds consist in the formation of a stellar black hole remnant at the end of the life of a POPIII star. Population III stars are born massive ($M_\star \simeq 10^2_\odot$), at extremely high redshift ($z \sim 30$). Due to the high mass, their life time is extremely short, and at the end they can form a black hole with stellar masses ($10 - 10^2\ M_\odot$). These early black holes could accreet into a SMBHs, but to reach $10^9\ M_\odot$ at redshift $z = 6$ a sustained Eddington accretion is required for their entire lifetime. This hypothesis seems to be unrealistic, due to the presence of accretion feedback which regulates the mass assembly. Volonteri & Rees 2005 also explored the possibility of super-Eddington accretion in the early Universe. Their work suggested that under certain conditions, such as dense gas environments and high inflow rates, black holes could exceed the

Eddington limit, allowing for rapid growth. However, sustaining such high accretion rates over long periods remains a challenge due to feedback mechanisms that can expel gas and modulate accretion.

Intermediate seeds are formed in NSCs. These environment are found in the centers of many galaxies, are dense aggregations of stars and provide a fertile ground for black hole formation through various processes. One prominent theory suggests that SMBH seeds form through the direct collapse of massive stars within NSCs. Stars with masses exceeding a few hundred solar masses are unable to sustain nuclear fusion, leading them to collapse directly into black holes. This process indicates that the high density and frequent star formation in NSCs can result in the creation of massive stars that rapidly form black hole seeds without going through supernova explosions (Lupi et al., 2014). A different pathway involves the growth of stellar-mass black holes through accretion and mergers within NSCs. Stellar-mass black holes in dense stellar environments can gather in a core of the cluster and consequently collapse into a SMBH seed (Davies et al., 2011).

Another proposed solution to the rapid growth of SMBHs is the "direct collapse" scenario or *heavy seeds* (Eisenstein & Loeb, 1995; Ferrara et al., 2014). This model posits that SMBHs could form from the direct collapse of massive gas clouds in the early Universe, bypassing the intermediate stages of stellar-mass black holes. The direct collapse model involves the formation of massive black holes through the collapse of gas clouds under specific conditions that prevent fragmentation and star formation. These conditions consist in:

1. The host halo should me massive ($T_{\rm vir} \geq 10^4$ K),
2. The Lyman-Werner external background should be able to prevent H_2 formation,
3. the gas must be metal free.

Thus, Bromm & Loeb 2003; Ferrara et al. 2014 suggested that in regions with low metallicity, where cooling is inefficient, massive primordial gas clouds could collapse directly into black holes with masses of $10^4 - 10^6\ M_\odot$. In a metal-free environment, the lack of efficient cooling mechanisms keeps the gas temperature high, leading to a higher Jeans mass and potentially a direct collapse into a massive black hole.

Moreover, Latif et al. 2013 conducted simulations showing that under high inflow rates and strong ultraviolet radiation fields, which inhibit fragmentation, gas clouds can collapse directly into massive black holes. These findings highlight the importance of specific environmental conditions in enabling the formation of massive seed black holes. The direct collapse black hole (DCBH) formation pathway has been modeled in various simulations. For example, Agarwal et al. 2014 conducted cosmological simulations that incorporated detailed treatments of radiative feedback, gas dynamics, and chemical processes to study the conditions leading to DCBH formation. They found that under the influence of a strong Lyman-Werner (LW) radiation background, which dissociates molecular hydrogen (H2) and suppresses cooling, massive gas clouds can collapse without fragmenting, leading to the formation of a DCBH with a mass of $10^4 - 10^6\ M_\odot$. In Fig. 3.2, we show the mass assembly for high redshift quasars, assuming a Eddington accretion rate. We also show the mass and redshift range at which different seeding scenarios are effective.

Primordial black holes

4

Primordial black holes (PBHs) are expected to have formed in the shortly after the Big Bang from the direct gravitational collapse of large density perturbations, amplified by the inflation process. Initially predicted by Zel'dovich & Novikov 1966, it was soon realised that PBHs are promising DM candidates (Hawking, 1971; Chapline, 1975). Any DM candidates must fulfill the following requirements: (i) they must be "cold", otherwise their velocity dispersion could have disrupted galaxy formation, and present in the Universe for its entire lifetime, namely they must be produced early on and still present nowadays. The formation of PBHs is expected to occur in the radiation dominated era and they are expected to be stable, since PBHs with mass $> 5\times10^{14}$ g have a lifetime longer than the age of the Universe; (ii) they must be non-baryonic, since they must not interact with the electromagnetic force and they must be in the right abundance ($\sim 25\%$ of the Universe critical density), while the Big-Bang Nucleosynthesis (BBN) theory constrains the baryons abundance to be at most 5% of the critical density (Cyburt et al., 2003).

For a long time, weakly interacting particles (WIMPs) have represented the most popular candidates for DM, as predicted in certain extensions of the standard model of particle physics. However, experiments such as the Large Hadron Collider (LHC) at CERN, the Cryogenic Dark Matter Search (CDMS), and Fermi, have not found any evidence of WIMPs. The LIGO-VIRGO detection of gravitational waves (Abbott et al., 2016) has rejuvenated the interest in considering PBHs as DM candidates (Kashlinsky, 2016a; Kohri & Terada, 2018), since it is difficult to reconcile the inferred masses of merging BHs ($\sim 30\ \mathrm{M}_\odot$) with current stellar evolution models.

4.1 PBHs formation

There are several processes that could lead to the formation of PBHs (Carr et al., 2016). In this Thesis, we only consider the direct collapse of large density perturbations. The collapse of an overdense region in the early Universe is facilitated by the high densities typical of that epochs. For a first order calculation, we can assume that all the mass inside the particle horizon collapses into a PBH:

$$M_{\mathrm{PBH}} \simeq \frac{c^3 t}{G} 10^{15} \left(\frac{t}{10^{-23}\mathrm{s}}\right) \mathrm{g}. \tag{4.1}$$

Based on this relation, the mass spectrum of PBHs can be very wide: PBHs formed at the Planck time (10^{-43} s) would have $M \sim 10^5$ g; the ones formed 1 second after the Big Bang would have $M \sim 10^5\ M_\odot$. For a more realistic estimate, it must be taken into consideration the possibility

that only a fraction, γ, of the mass inside the horizon collapse into a PBH:

$$M_{\rm PBH} = \gamma M_H \approx 2.03 \times 10^5 \gamma \left(\frac{t}{1s}\right) M_\odot, \tag{4.2}$$

γ depends on the details of the collapse. A first analytical calculation suggested $\gamma \approx 0.2$ during the radiation era (Carr & Kuhnel, 2021). More precise and recent calculations find $\gamma = 0.4$ (Green et al., 2004).

The initial abundance of PBHs is set by the mass fraction of the Universe that collapsed into PBHs. This fraction $\beta(M)$ depends on the mass-scale involved (M), namely on the epoch at which PBHs were formed, and can be estimated using the Press-Schechter formalism. The probability that a region with a given mass $M_{\rm PBH}$ has a density contrast exceeding the critical threshold for collapse (δ_c) is given by:

$$\beta(M_{\rm PBH}) = \int_{\delta_c}^{\infty} \frac{1}{\sqrt{2\pi}\sigma(M)} \exp\left(-\frac{\delta^2}{2\sigma(M)^2}\right) d\delta. \tag{4.3}$$

For a Gaussian distribution, the integral can be approximated as:

$$\beta(M_{\rm PBH}) \simeq \frac{1}{2}{\rm erfc}\left(\frac{\delta_c}{\sqrt{2}\sigma(M)}\right), \tag{4.4}$$

where $\sigma(M)$ is the standard deviation of the density fluctuations smoothed on the mass scale M. Being $\beta(M) = \frac{\Omega_{\rm PBH}}{\Omega_{\rm rad}}$, we can estimate the PBHs density parameter as:

$$\Omega_{\rm PBH} = \beta\Omega_{\rm rad}(1+z)10^6\beta\left(\frac{\rm t}{\rm 1s}\right)^{-1/2} 10^{18}\beta\left(\frac{\rm M}{10^{15}{\rm g}}\right)^{-1/2} ({\rm M} > 10^{15}{\rm g}), \tag{4.5}$$

where the factor $(1+z)$ arises because the PBH density scales as $\propto (1+z)^3$, while the radiation density $\propto (1+z)^4$. The lower limit on the PBH mass ($M > 10^{15}$g) follows from the condition of non evaporating PBHs, as discussed in Sec. 4.2. For a region to collapse into a PBH, its density must be large enough for the gravitational force to overcome both the pressure gradient and the expansion of the Universe. The critical threshold for the collapse of a density fluctuation into a BH is a key parameter for the formation of PBHs, and it depends both on the dynamics of the early Universe and the nature of the perturbations. During the radiation dominated era, the energy density of the Universe is dominated by radiation. In a radiation-dominated Universe the critical threshold is found to be approximately $\delta_c \simeq 0.45$ (Carr & Hawking, 1974).

Numerical simulations has been used to strengthen and refine this result. Initial conditions are based on a model of primordial density fluctuations, typically assumed to follow a Gaussian random field. The power spectrum $P(k)$ of these fluctuations is derived from cosmological observations and theoretical models, providing the distribution of perturbation amplitudes across different scales. For PBH formation studies, initial density contrasts $\delta(\vec{x})$ are sampled from this Gaussian distribution. The fluctuations are then evolved forward in time to observe their behavior under the influence of gravity and pressure forces. A set of fully relativistic hydrodynamical simulations developed by Niemeyer & Jedamzik (1999) has initially confirmed the Carr & Hawking (1974) result ($\delta_c \simeq 0.45$). By using general relativistic hydrodynamics simulations, Shibata & Sasaki 1999 found a slightly lower value for the critical threshold ($\delta_c = 0.42$). This small difference in the threshold can strongly impact the PBH initial abundance, but follow up works brought the critical density estimation back to its initial value (Musco et al., 2005, 2009; Harada et al., 2013). Finally, more recent works have considered the possibility of having a density threshold that varies depending on the shape of the initial power spectrum ($\delta_c \simeq 0.4 - 0.5$, Germani & Musco, 2019).

4.1.1 The mass function of PBHs

The mass function of PBHs is still a topic of debate. Its functional form depends on the conditions in the early Universe, including the nature of density fluctuations and the dynamics of gravitational collapse. Various forms of the mass function have been proposed, each based on different assumptions about the initial conditions and PBH formation processes. Understanding the PBH mass function is crucial to correctly predict their abundance and, consequently, their observational signatures.

The most simplistic assumption is a monochromatic distribution:

$$\psi(M) = \delta(M - M_0). \tag{4.6}$$

This indicates that all PBHs have the same mass, simplifying the study of their cosmological and observational effects. This model is often used for specific theoretical studies and makes the analysis more tractable. Such an assumption provides us with a starting point to understand the influence of PBHs on our Universe. The function $\psi(M)$ can be interpreted as the number density of PBHs in a mass range $(M, M + dM)$:

$$\psi(M) = M\frac{dn}{dM} = \frac{dn}{dlnM}, \tag{4.7}$$

and allows us to define the corresponding PBHs mass density $\rho_{\rm PBH}$ and dark matter fraction $f_{\rm PBH}(M)$:

$$\rho_{\rm PBH}(M) = M^2\frac{dn}{dM}, \tag{4.8}$$

$$f_{\rm PBH}(M) = \frac{\rho_{\rm PBH}}{\rho_{\rm CDM}}. \tag{4.9}$$

If $f_{\rm PBH}(M)$ is close to unity, PBHs could represent a good candidate for the dark matter, thus a good esteem of this value, which heavily depends on the mass spectrum, would be crucial in verifying this hypothesis.

One of the simplest and most studied scenarios is the scale-invariant power spectrum, also known as the Harrison-Zel'dovich spectrum. In this case, the power spectrum of primordial density fluctuations is proportional to the wavenumber k, which means it is the same on all scales. For a scale-invariant power spectrum, the density fluctuations are evenly distributed across different scales, leading to a specific form of the mass function. The power spectrum $P(k)$ is given by:

$$P(K) \propto k. \tag{4.10}$$

To derive the mass function, we start by considering how these fluctuations evolve over time. The variance $\sigma^2(M)$ of the density fluctuations on a mass scale M is related to the power spectrum through an integral involving a smoothing window function. For a scale-invariant spectrum, this variance is constant across scales, leading to a mass function that follows a power-law distribution. The resulting mass function $\psi(M)$ describes the number density of PBHs with a given mass M:

$$\psi(M) \propto M^{-\frac{3}{2}}. \tag{4.11}$$

This form implies a broad distribution of PBH masses, reflecting the scale invariance of the initial perturbations (Carr, 1975).

Another more flexible model that can describe various inflationary scenarios involves a power-law spectrum, where $P(k) \propto k^n$. In this case, the variance $\sigma^2(M)$ on a mass scale

M depends on the spectral index n. This leads to a mass function that also follows a power-law distribution but with a different exponent, reflecting the influence of the spectral index. The mass function $\psi(M)$ for a power-law spectrum is:

$$\psi(M) \propto M^{-\frac{3+n}{2}}. \tag{4.12}$$

This form shows how different values of n result in different slopes for the mass distribution, capturing a range of possible scenarios for PBH formation (Niemeyer & Jedamzik, 1999).

Another possible choice for the PBHs mass function is a log-normal distribution. A log-normal distribution is often used when the initial perturbations have a characteristic scale. It is a function of the characteristic mass (M_c) and the variance σ around the peak:

$$\psi(M) \propto \frac{1}{M} \exp\left(\frac{(\ln M - \ln M_c)^2}{2\sigma^2}\right). \tag{4.13}$$

Besides the aforementioned cases, more complicated forms for the mass function have been recently proposed (García-Bellido & Ruiz Morales, 2017; Franciolini et al., 2022). The first work proposed a double-peaked mass function, which can arise from a spectrum with two distinct peaks, often motivated by features in the inflationary potential. The double-peaked mass function can be modeled as a sum of two log-normal distributions:

$$\psi(M) \propto \frac{A_1}{M} \exp\left(\frac{(\ln M - \ln M_{c1})^2}{2\sigma_1^2}\right) + \frac{A_2}{M} \exp\left(\frac{(\ln M - \ln M_{c2})^2}{2\sigma_2^2}\right). \tag{4.14}$$

This form allows for a more complex structure in the PBH mass distribution, potentially reflecting multiple formation mechanisms or features in the inflationary potential. Moreover, it seems to avoid the majority of existing constraints on the abundance of PBHs ($f_{\rm PBH}$), leaving open the possibility that PBHs constitute a non-negligible fraction of dark matter. Finally, Franciolini et al. (2022) proposed a different extended mass function exploring different values of the tilt (n_s) of the curvature power spectrum. Different choices of n_s result in broad mass distributions peaking at different PBH masses.

4.2 PBHs as Dark Matter candidates

Several experiments have been carried out in the last 20 years to constrain the fraction of DM in PBHs, hereafter $f_{\rm PBH}$. This can be done by exploring the impact of PBHs on several astrophysical phenomena (see Carr & Kühnel 2020), such as gamma rays emission from evaporating PBHs (Laha, 2019; Coogan et al., 2021), microlensing effects (Niikura et al., 2019; Blaineau et al., 2022) and disruption of wide binaries or ultra-faint dwarfs (Monroy-Rodríguez & Allen, 2014; Brandt, 2016). Furthermore, signatures of accreting PBHs are expected to be left on the CMB spectrum and its anisotropies (Poulin et al., 2017), the 21 cm power spectrum (Mena et al., 2019), and the X-ray/radio/infrared backgrounds (Cappelluti et al., 2022; Ziparo et al., 2022; Manzoni et al., 2024). Although current constraints on $f_{\rm PBH}$ are quite stringent (typically $f_{\rm PBH} \lesssim 10^{-2} - 10^{-3}$ for $10^{-10} < M_{\rm PBH} < 10^{15}$ $M_\odot$, see Fig. 10 by Carr et al., 2021), this does not question that PBHs could have formed in the early Universe and affect the subsequent evolution of structure formation (e.g. Inman & Ali-Haïmoud, 2019).

In this section we will summarize the constraints already collected on the dark matter fraction, $f_{\rm PBH}$, which are schematically shown in fig 4.1, taken from Carr & Kuhnel (2021). Note that all of these constraints are obtained with the underlying assumption that the PBHs mass spectrum is represented by a delta function.

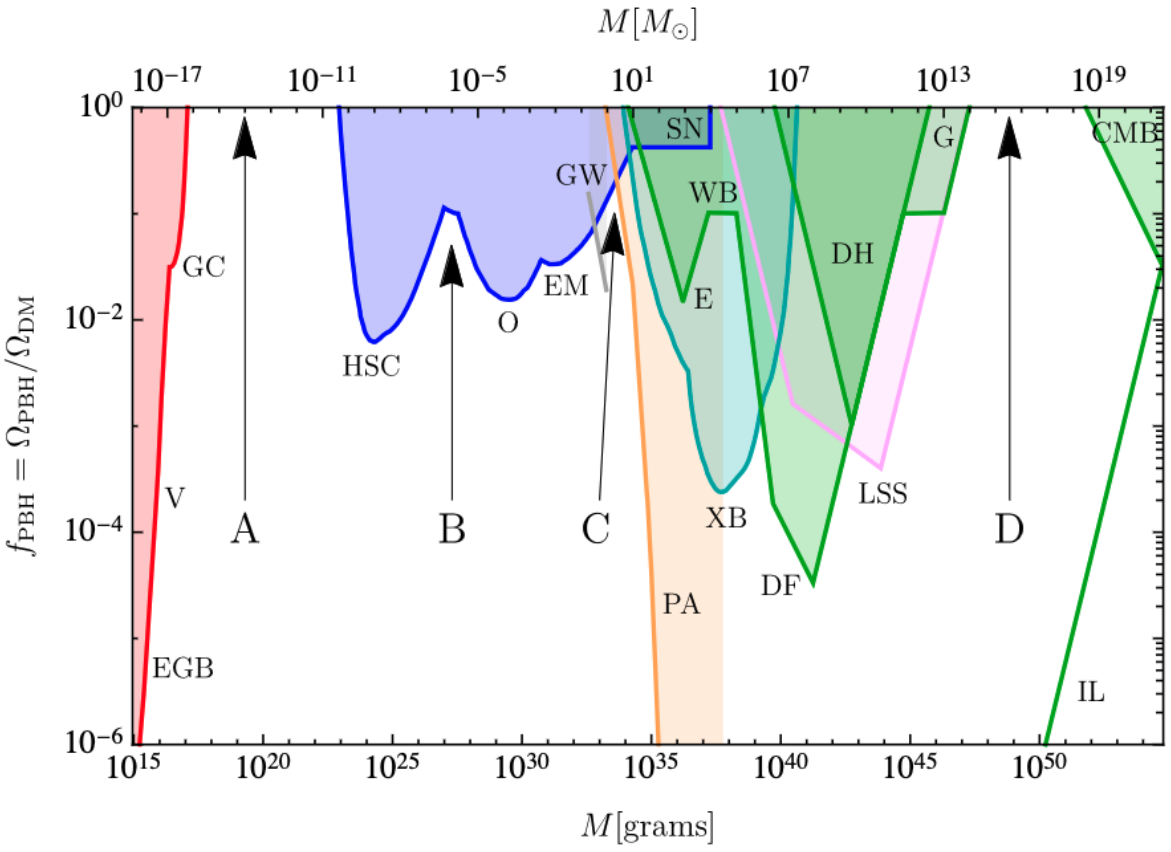

Figure 4.1: Current major constraints on $f_{\rm PBH}$. Different shaded regions indicate different physical effects used to probe PBHs abundance: evaporation (red), lensing (blue), CMB distortions (orange), accretion (cyan), dynamical (green). The four arrows point out the mass windows where PBHs could still account for a non-negligible fraction of DM. Credit: Carr & Kühnel 2020.

Constraints from Hawking evaporation In eq. (4.5) the value $M_{lim} = 10^{15}$ g represents the lower limit for the initial mass of an observable PBH (at the present time). Indeed, below this mass PBHs would have evaporated due to Hawking radiation emission in the lifetime of the Universe. Hawking introduced this process in the 1974 combining results from thermodynamics, quantum mechanics and general relativity (Hawking, 1974) . Thus, black holes radiate thermally with a temperature:

$$T = \frac{\hbar c^3}{8\pi G M k} \simeq 10^{-7} \left(\frac{M}{M_\odot}\right)^{-1} \text{K}. \tag{4.15}$$

We can set a lower limit for the PBH mass, by considering the evaporation rate:

$$\frac{dM}{dt} \propto -M^{-2}. \tag{4.16}$$

Integrating this equation and substituting the relation for the mass in eq. (4.1), we can find the PBH lifetime:

$$t \approx 10^{71} \left(\frac{M}{M_\odot}\right)^{3} \text{s}. \tag{4.17}$$

We can see that PBHs whit a mass smaller than M_{lim} would be evaporated in the age of the universe. PBHs evaporating at the present days would emit observable radiation in the X-ray and γ-ray bands. The absence of detection of these contributions to the X-ray and γ-ray backgrounds

allowed to constrain the lower mass range ($M_{\rm PBH} \leq 10^{17}$ g) for non-evaporated PBHs. This constraint is represented by the red shaded area in Fig. 4.1.

Constraints from lensing Constraints on massive astrophysical compact halo object (MACHOs) with very low M come from the femtolensing of γ-ray burst. Assuming the bursts are at range $z \sim 1$ the non detection of femtolensing effects give us the limits on M. This constraint was set by Barnacka et al. 2012:

$$f_{\rm PBH}(M) < 0.1 \ (5 \times 10^{16}{\rm g}) < {\rm M} < 10^{19}{\rm g}. \tag{4.18}$$

Microlensing observations of stars in the Large and Small Magellanic Clouds (LMC, SMC) can probe the fraction of the Galactic halo in MACHOs. The optical depth of the halo towards LMC and SMC, defined as the probability that any given star is amplified by at least 1.34 at a given time, is related to the fraction $f_{\rm PBH}(M)$ by

$$\tau_L^{(SMC)} = 1.4\tau_L^{(LMC)} = 6.6 \times 10^{-7} f \tag{4.19}$$

following the halo model in (Alcock et al., 2000). The EROS experiment obtained more stringent constraints by arguing that some of the MACHO events were due to self-lensing excluding $6 \times 10^{-8} M_\odot < M < 15 M_\odot$ MACHOs from be a substantial part of the halo. The latest constraints from MACHO and EROS experiments can be summarized as follow:

$$f_{\rm PBH}(M) < \begin{cases} 0.1\,(6 \times 10^{-8}\ M_\odot < M < 15\ M_\odot), \\ 0.1\ \ (6 \times 10^{-6}\ M_\odot < M < 1\ M_\odot), \\ 0.4(6 \times 10^{-3}\ M_\odot < M < 0.1\ M_\odot). \end{cases} \tag{4.20}$$

The Optical Gravitational Lensing Experiment (OGLE) placed different constraints in the high mass range:

$$f_{\rm PBH}(M) < \begin{cases} 0.2\ (0.1\ \ M_\odot < M < 20\ M_\odot), \\ 0.09\ (0.4\ \ M_\odot < M < 1\ M_\odot), \\ 0.06\ (0.1 M_\odot < M < 0.4\ M_\odot). \end{cases} \tag{4.21}$$

For the low mass range Kepler has improved substantially the existing limits (Griest et al., 2014):

$$f_{\rm PBH}(M) < 0.3(2 \times 10^{-9} M_\odot < M < 10^{-7} M_\odot). \tag{4.22}$$

Millilensing of compact radio sources gives limits in the high mass range:

$$f_{\rm PBH}(M) < \begin{cases} (M/2\ \times 10^4\ M_\odot)^{-2} (M < 10^5\ M_\odot), \\ 0.06\quad (10^5\ M_\odot < M < 10^8\ M_\odot), \\ (M/4 \times 10^8\ M_\odot)^2\ \ (M > 10^8\ M_\odot). \end{cases} \tag{4.23}$$

These constraints are shown in Fig. (4.1) as a blue shaded region.

Dynamical constraints Dynamical constraints on primordial black holes (PBHs) arise from their gravitational interactions with other objects and structures in the Universe. If PBHs were a significant component of dark matter, their gravitational effects would have observable consequences on the dynamics of stars, galaxies, and galaxy clusters. Various studies have used these effects to place stringent limits on the mass and abundance of PBHs.

It has been suggested that halo PBHs could be captured and swallowed by stars in the Galactic disk (Roncadelli et al., 2009). The black hole would accrete the star producing a sensible amount of radiation and a population of subsolar black holes. In the paper it is pointed out that if the dark matter were in PBHs smaller than 3×10^{26} g, every disc star would contain such a black hole. The constraint is placed since the population of subsolar black holes and the accretion process are not observed. The time scale, τ_{cap}, of a PBH capture from a star scales as $\tau_{cap} \propto n_{PBH}^{-1} \propto M\ f_{\rm PBH}(M)^{-1}$, and imposing this value to be high than age of the Galactic disc gives:

$$f_{\rm PBH}(M) < (M/3\ \times\ 10^{26})\ \mathrm{g}. \tag{4.24}$$

A similar analysis of the collisions of PBHs with white dwarf and neutron stars was carried out in Capela et al. (2013). Since this process of accretion for white dwarf and neutron stars is not observed, this sets another limit on $f_{\rm PBH}(M)$:

$$f_{\rm PBH}(M) < \frac{M}{4.7 \times 10^{24}\ \mathrm{g}} \left(1 - exp\left[-\frac{M}{2.9 \times\ 10^{23}\ \mathrm{g}}\right]\right)^{-1}\ (2.5\ \times\ 10^{18}\ \mathrm{g} < \mathrm{M} < 10^{25}\ \mathrm{g}). \tag{4.25}$$

The disruption of binary star systems with wide separation represents another possible way to probe the abundance of halo PBHs. By comparing the results of simulations with observations it has been shown that

$$f_{\rm PBH}(M) < \begin{cases} (M/500 M_\odot)^{-1} (500\ M_\odot < M < 10^3\ M_\odot), \\ 0.4 \qquad\quad (10^3\ M_\odot < M < 10^8\ M_\odot). \end{cases} \tag{4.26}$$

In the high mass range we have constraints placed with a similar argument to the previous one, but applied on the globular cluster. They would have been disrupted by the tidal force of PBHs passing nearby, unless:

$$f_{\rm PBH}(M) < \begin{cases} (M/3\ \times\ 10^4\ M_\odot)^{-1}\ (3\ \times\ 10^4\ M_\odot < M\ < 10^6\ M_\odot) \\ 0.03 \qquad\qquad\quad (10^6\ M_\odot\ < M\ < 10^{11}\ M_\odot) \end{cases} \tag{4.27}$$

Note that this strongly depends on the mass and the radius of the cluster. It is interesting to note that each of these dynamical constraints corresponds to an upper limit on the mass of the objects which dominate the halo in the mass range $500\ -\ 2\ \times\ 10^4\ M_\odot$, the binary-disruption limit being the strongest. These constraints are shown in Fig. (4.1) in green.

Accretion constraints It has been pointed out that PBHs cannot grow significantly during the radiation dominated era (Carr & Hawking, 1974; Gundlach, 2000). Even if this does not occur, PBHs in the high mass range can accrete also in a period after decoupling. This process would have lead to emission of radiation that could have a profound impact on the thermal history of the universe. This possibility has been examined in depth in the work by Ricotti et al. (2008a). The emitted X-rays would produce measurable effects in the spectrum and anisotropies of the CMB. By comparing FIRAS and WMAP data with theoretical calculations, the following constraints have been obtained:

$$f_{\rm PBH}(M) < \begin{cases} (M/30\ M_\odot)^{-2}\ (30\ M_\odot\ <\ M\ <\ 10^4\ M_\odot) \\ 10^{-5} \qquad (10^4\ M_\odot\ < M\ <\ 10^{11}\ M_\odot) \end{cases} \tag{4.28}$$

from WMAP data, and:

$$f_{\rm PBH}(M) < \begin{cases} (M/1\ M_\odot)^{-2} & (1\ M_\odot\ <\ M\ <\ 10^3\ M_\odot) \\ 0.015 & (10^3\ M_\odot\ <\ M\ <\ 10^{14}\ M_\odot) \end{cases} \tag{4.29}$$

from FIRAS data. These constraints are shown in Fig. (4.1) in orange and cyan.

To finish, we want to underline that the constraints presented above are derived assuming a monochromatic PBH mass distribution. This non-physical assumption is used to simplify calculations. The constraints presented in Fig. 4.1 change in the presence of an extended mass function. Here, we discuss the formalism presented in (Carr et al., 2017) to derive constraints on $f_{\rm PBH}$ valid in the case of an extended mass function, starting from the ones derived with a monochromatic mass functions. The PBH extended mass function has a typical functional form:

$$\psi(M) \propto M\frac{dn}{dM}, \tag{4.30}$$

and it can be normalized to have the total fraction $f_{\rm PBH}$:

$$f_{\rm PBH} = \int_{M_{\rm min}}^{M_{\rm max}} dM\psi(M). \tag{4.31}$$

The mass function is determined by the mean and variance of the log$M$ distribution:

$$\log M_c = \langle \log M \rangle_\psi\,, \tag{4.32}$$

$$\sigma^2 = \langle \log^2 M \rangle_\psi - braket \log M_\psi^2. \tag{4.33}$$

If the constraint in the monochromatic case is given by $f_{\rm PBH}(M) \leq f_{\rm max}(M)$, at the same mass we obtain:

$$\int dM \frac{\psi(M)}{f_{\rm max}(M)} \leq 1. \tag{4.34}$$

Given a mass range (M_1, M_2) and a particular mass function $\psi(M)$, by computing the integral given in Eq. 4.34 over the mass range, a new constraint is obtained. This constraint is a function of the mean and variance of the mass distribution.

4.3 PBHs spatial distribution

PBHs are discrete objects and they are expected to be Poissoninanly distributed, due to the absence of correlation on causal distances at formation. The Poisson distribution results in a shot-noise term in the power spectrum that can be expressed as (Villanueva-Domingo & Ichiki, 2021):

$$P_{\rm poi} = \frac{f_{\rm PBH}^2}{n_{\rm PBH}}, \tag{4.35}$$

where $n_{\rm PBH}$ is the number density of PBHs, and in the case of a monochromatic mass distribution can be written as:

$$n_{\rm PBH} = \frac{f_{\rm PBH}\Omega_{\rm dm}\rho_0}{M_{\rm PBH}}. \tag{4.36}$$

This extra term in the power spectrum correspond to isocurvature fluctuations (Afshordi et al., 2003; Chisholm, 2006), thus resulting in a power spectrum which is a combination of isentropic and isocurvature perturbations. The extra term due to PBHs, can be written as:

$$P_{\rm iso} = T_{\rm iso}^2 P_{\rm poi} = \frac{9}{4}(1+z_{\rm eq})^2 \frac{f_{\rm PBH}M_{\rm PBH}}{\Omega_{\rm DM}\rho_c}, \tag{4.37}$$

where $T_{\rm iso}$ is the transfer function for isocurvature modes that can be expressed as (Peacock, 1998):

$$T_{\rm iso} = \frac{3}{2}(1 + z_{\rm eq}). \tag{4.38}$$

To fully understand why the PBHs spatial distribution is Poissonian, the two point correlation function has to be computed:

$$\langle \delta_{\rm PBH}(x)\delta_{\rm PBH}(0)\rangle = \frac{1}{n_{\rm PBH}}\delta_D(x) + \xi_{\rm PBH}(x), \tag{4.39}$$

where δ_D is the Dirac's delta, and $\xi_{\rm PBH}(x)$ is the reduced correlation function. In this formalism, $\xi_{\rm PBH}(x) = b_0^2\xi_r(r)$ is the product of the linear scale-independent PBH bias (b_0), and the radiation correlation function (ξ_r). The local PBHs number density perturbation can be expressed as:

$$\delta(x)_{\rm PBH} = \frac{P_1(>\nu|x)}{P_1(>\nu)} - 1, \tag{4.40}$$

where P_1 is the probability distribution function for the field density.

In the standard Gaussian framework for the density perturbation, no initial clustering is expected from PBHs. On the other hand, the introduction of small non-Gaussianities in the primordial power spectrum leads to PBH clustering at their formation epoch. The density contrast can be related to the curvature perturbation $\zeta(k)$ as:

$$\delta(k,a) \simeq \frac{4}{9}\left(\frac{k}{aH}\right)^2 \zeta(k), \tag{4.41}$$

where a is the scale factor, and $aH \sim R_H^{-1}$.

For the description of the PBHs initial spatial distribution, we follow the formalism presented in (Franciolini, 2021), adopting a notation similar to the one used for the "peak-background split" model, commonly used in the context of large scale structure. We will refer with k_s to the short-wavelength modes, namely the ones corresponding to the scale of PBHs formation, and with k_l to the large scale modes. In the Press-Schechter formalism, large scale modes can modulate the probability of small scale modes to collapse, impacting the critical density for collapse as: $\delta_c \to \delta_c - \delta_l$. When the collapse occurs in a region modulated by a long wavelength mode with density δ_l, the number density of PBHs is modified as:

$$\delta_{\rm PBH}(x) = \frac{\partial\delta_c}{\partial\delta_l}\frac{\partial \log P_1}{\partial\delta_c}\delta_l(x) \simeq \frac{\nu}{\sigma_s}\delta_l(x), \tag{4.42}$$

where in the last step we defined $\nu = \delta_c/\sigma_s \gg 1$. We can thus rewrite the scale independent bias as:

$$b_0 \simeq \frac{\delta_c}{\sigma_s^2} = \frac{\nu}{\sigma_s}, \tag{4.43}$$

and consequently write the PBHs correlation function on large scales as:

$$\xi_{\rm PBH}(x) = b_0^2\xi_r(x, a_H). \tag{4.44}$$

It has to be noted that the spatial modulation must be imprinted at the time of PBH collapse, which corresponds to the time of horizon crossing of the short modes $a_H \sim k_s$. Therefore, although a biasing factor ν/σ_s is of the order of $b_0 \sim 10^2$, $\delta_{\rm PBH}$ is still suppressed compared to

the ζ_l amplitude. This is related to the functional form of PBHs local number density at large scales:

$$\delta_{\rm PBH}(k_l) \simeq \frac{4}{9} b_0 \left(\frac{k_l}{k_s}\right)^2 \zeta_l \ll \zeta_l, \tag{4.45}$$

and by construction $k_l \ll k_s$. Ultimately, in a purerly Gaussian case, even if the amplitude of small density fluctuation is modulated by long-wavelength modes, there is no impact on the local PBHs density. Thus, the PBH spatial distribution is purely Poissonian.

The picture drastically change if local non-Gaussianities are introduced in the power spectrum of density fluctuations:

$$\zeta(x) = \zeta_G(x) + f_{\rm NL}[\zeta_G(x)^2 - \langle \zeta_G(x)^2 \rangle]. \tag{4.46}$$

In this case, the long-wavelength density perturbation δ_l not only effectively reduces the threshold for collapse δ_c, as in the Gaussian case, but it is also able to modulate the variance of short-wavelength perturbations, δ_s. This causes the bias parameter

$$b = \frac{d \log P1}{d\delta_l} \tag{4.47}$$

to be modified by an extra term, called scale-dependent bias (Tada & Yokoyama, 2015):

$$\delta b = \frac{\partial \log \sigma_s}{\partial \delta_l} \frac{\partial \log P_1}{\partial \log \sigma_s}. \tag{4.48}$$

In this framework, the field variance is modulated by long modes as:

$$\sigma_s(x) = (1 + 2 f_{\rm NL} \zeta_l(x)) \bar{\sigma}_s, \tag{4.49}$$

where $\bar{\sigma}_s^2$ denotes the average variance of δ_s. The scale dependent bias can thus be computed as:

$$\Delta b(k) = \frac{9}{2} \nu^2 f_{\rm NL} (k R_{\rm PBH})^{-2}. \tag{4.50}$$

In this framework the PBH local density is linearly modulated by the presence of long wavelength modes:

$$\delta_{\rm PBH} \simeq 2\nu f_{\rm NL} \zeta_l(k_l). \tag{4.51}$$

Ultimately, this effect implies that the presence of non-Gaussianities in the primordial power spectrum results in PBHs clustering at their formation epoch. We show a schematic description of this effect in Fig. 4.2.

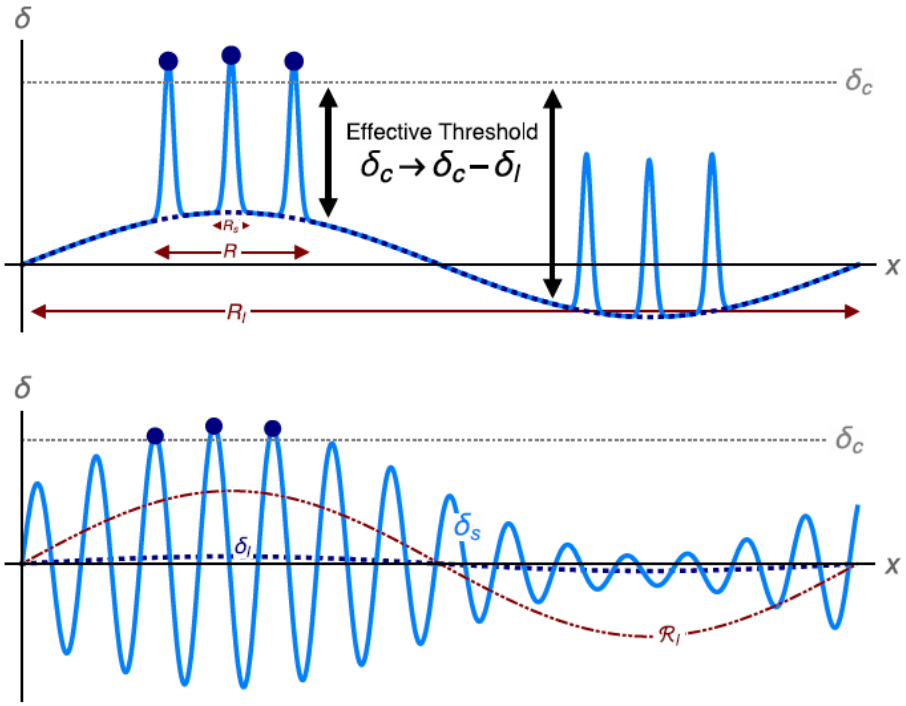

Figure 4.2: Schematic view of the effect of coupling between long- and short-wavelength modes. Top panel shows the effect of long wavelength modes effectively reducing the critical density for collapse (δ_c). This effect remains suppressed in a standard Gaussian scenario. Bottom panel shows that the short mode variance is modulated by the coupling of the long-wavelength mode in the presence of non-Gaussianities, leading to a spatial correlation between the peaks that will form PBHs. Credit: Tada & Yokoyama 2015.

Part II

Methods and results

Cosmic radiation backgrounds from primordial black holes

5

5.1 Introduction

The discovery of gravitational waves from black hole mergers detected with the LIGO/VIRGO interferometers provided us with a new channel to study astrophysical black holes. Interestingly, the generally high mass/low spin values inferred by these experiments (Abbott & Collaboration, 2016) are consistent with primordial black holes (PBHs) properties predicted by theoretical models (e.g. Sasaki et al. 2016; Bird et al. 2016; Clesse & García-Bellido 2017).

Primordial black holes (PBHs) are expected to be formed by gravitational collapse of overdense regions in the early Universe (Hawking, 1974), during the radiation dominated era. Given their early origin, PBHs can affect several properties of the Universe, such as the amplitude of primordial inhomogeneities (García-Bellido & Ruiz Morales, 2017), and the matter distribution in the early Universe (e.g., Afshordi et al. 2003; Inman & Ali-Haïmoud 2019). In addition, extra energy injection due to PBHs accretion or evaporation affects the thermal history of the Universe (Mena et al., 2019; Cang et al., 2021).

PBHs are non-baryonic Dark Matter candidates (Carr et al., 2016), and their abundance is described with the parameter $f_{\rm PBH} = \Omega_{\rm PBH}/\Omega_{\rm DM}$, i.e., the fraction of dark matter composed by PBHs. Under the standard assumption of a monochromatic PBH mass distribution, several constraints already exist on $f_{\rm PBH}$ from different astrophysical processes. The low-mass end of the PBH mass spectrum ($M < 10^{-16} M_{\odot}$) is constrained through PBHs evaporation using the out-coming radiation as an observable. For instance, an upper limit of $10^{-8} < f_{\rm PBH} < 1$ was found in the mass range $10^{-19}{\rm M}_{\odot} < M_{\rm PBH} < 10^{-16}{\rm M}_{\odot}$ by comparing the gamma-ray radiation expected from PBH evaporation with the observed gamma-ray background (Chen et al., 2022). Different constraints on $f_{\rm PBH}$ were set by the comparison between the BH merger rates detected by LIGO and the ones predicted by PBH models (Ali-Haïmoud et al., 2017; Ballesteros et al., 2018). In the subsolar mass range ($10^{-8}{\rm M}_{\odot} \leq M_{\rm PBH} \leq 1\ {\rm M}_{\odot}$), gravitational lensing has been the dominant process used to search for PBHs signature (e.g., Tisserand et al. 2007; Niikura et al. 2019; Smyth et al. 2020) allowing for only a small fraction ($f_{\rm PBH} \lesssim 10^{-2}$) of DM in the form of PBHs. The comparison between the CMB anisotropies value predicted when the contribution of accreting PBHs is accounted for and the observed one was used by Poulin et al. (2017) and Ali-Haïmoud & Kamionkowski (2017) to set constraints ($f_{\rm PBH} < 10^{-3}$) in the mass range $10^2 \leq M_{\rm PBH} \leq 10^5$. For higher masses, the dynamical effects induced by PBHs (e.g. tidal disruption of dwarf galaxies) dominate the constraints (e.g., Monroy-Rodríguez & Allen 2014; Carr & Silk 2018; Zoutendijk et al. 2020 allowing only a small fraction of DM ($f_{\rm PBH} \leq 10^{-5}$) to be comprised of PBHs.

The entire mass spectrum is thus widely constrained, leaving only one window (i.e., 10^{-16} –

$10^{-11} M_\odot$ (Carr et al. 2021, corresponding to the asteroid mass range) in which PBHs could constitute the entirety of dark matter. Although adopting a broader mass distribution allows the entirety of DM to be comprised of PBHs without exceeding existing constraints (Hasinger, 2020a), such an approach requires a physically unjustified fine-tuning of the mass distribution.

The presence of a (still unrecovered) population of accreting black holes at high redshift can be used to explain several observational results. For instance, a signal in excess of that produced by known sources was measured by several works (e.g. Hickox & Markevitch, 2006, 2007; Cappelluti et al., 2017) in the Cosmic X-ray Background (CXB) using the Chandra space telescope. The origin of such excess has been ascribed to the presence of still undiscovered, high-z BHs ($z > 6$, Salvaterra et al., 2012; Kashlinsky, 2016b; Ananna et al., 2020).

The Absolute Radiometer for Cosmology, Astrophysics, and Diffuse Emission (ARCADE2) experiment measured measured an absolute sky brightness of $T_b = 54 \pm 6$ mK at 3.3 GHz. This implies an excess in the Cosmic Radio Background (CRB) of $5\times$ with respect to prediction from theoretical models (Condon et al., 2012). In particular, the ARCADE2 results suggested the possibility that the CMB may not be the dominant source of the extragalactic radio background (Ewall-Wice et al., 2020). The measurement was used, together with previous ones, to fit the radio-excess with a power-law spectrum, finding a spectral dependence $\nu^{-0.6}$ typical of the synchrotron radiation. The power-law results in 480 mK at 1.4 GHz or 21 cm. PBHs can also explain the anomalous 21-cm absorption signal reported by the Experiment to Detect the Global EoR Signature (EDGES, Bowman et al., 2018).

In this work, we explore the possiblity that PBHs are the sources of the excess signals in the CXB and CBR, and can explain the EDGES absorption signal. A widely used approach to model PBH accretion in the eary Universe (e.g., Ricotti et al. 2008a,b; Mena et al. 2019; Hasinger 2020a) is to assume that PBHs are surrounded by a uniform gas distribution, thus neglecting accretion from denser gas, located in virialized structures. In this work we add this important ingredient, i.e. PBH accretion inside DM halos. A similar approach was undertaken by Gaggero et al. (2017) in a Milky Way context. We build up on that work, further modeling the PBH-gas interaction in a cosmological framework.

The paper is organized as follows. In Sec. 5.2 we describe the model[1] adopted in this work, in Sec. 5.3 we review the model implications for the IGM thermal history; Sec. 5.4 contains the main findings of this work. In Sec. 5.5 we compare our results with previous ones, and Sec. 5.6 presents a brief summary.

5.2 Model

In this section, we describe the theoretical model adopted to distribute PBHs in the Universe (Sec. 2.1), to compute their accretion (Sec. 2.2), the resulting X-ray and radio emission (Sec. 2.3), and the corresponding cosmic backgrounds (Sec. 2.4).

5.2.1 PBHs cosmological distribution

In this work, we assume that PBHs constitute a fraction of dark matter $f_{\rm PBH} = \Omega_{\rm PBH}/\Omega_{\rm DM}$. The PBH density distribution is assumed to track dark matter, which is in turn organised into virialized objects (halos) and a diffuse component at the mean cosmic density, i.e. the intergalactic

[1] We adopt a ΛCDM cosmology in agreement with Planck18 (Planck Collaboration et al., 2020) results: $\Omega_{\rm m} = 0.315$, $\Omega_\Lambda = 0.685$, $\Omega_{\rm b} = 0.049$, $\sigma_8 = 0.811$, $n_s = 0.965$, and $H_0 = 100\,h$ km s^{-1} Mpc^{-1} = 67.4 km s^{-1} Mpc^{-1}.

medium (IGM). The PBH number density, $n_{\rm PBH}$, at redshift z is then given by:

$$n_{\rm PBH}(z) = \frac{\Omega_{\rm DM}\rho_c f_{\rm PBH}(1+z)^3}{M_{\rm PBH}} = n^{\rm IGM}_{\rm PBH}(z) + n^{h}_{\rm PBH}(z), \tag{5.1}$$

where $\rho_c = 3H^2/8\pi G$ is the critical density of the Universe, $M_{\rm PBH}$ is the PBH mass, and $n^{\rm IGM}_{\rm PBH}$ ($n^{h}_{\rm PBH}$) represents the number density of PBHs in the IGM (DM halos). We assume a monochromatic PBH mass distribution, in the range $1 \leq M_{\rm PBH} \leq 1000\ {\rm M}_\odot$.

The relative abundance of PBHs in halos and IGM depends on the fraction of dark matter that collapses into virialized structures per comoving volume, that can be computed through the Press-Schechter formalism (Press & Schechter, 1974):

$$f_{\rm coll}(\ M_{\rm min}, z) = {\rm erfc}\left[\frac{\delta_c(z)}{\sqrt{2}\sigma_M}\right], \tag{5.2}$$

where $\delta_c = 1.686/D(z)$ is the critical density for collapse, $D(z) \propto (1+z)^{-1}$ is the growth factor, σ_M is the standard deviation of the linearly extrapolated matter power spectrum, and $M_{\rm min}$ is the minimum halo mass such that efficient cooling processes are triggered (see Sec. 5.2.4).

PBHs in the IGM

The number density of PBHs in the IGM is given by:

$$n^{\rm IGM}_{\rm PBH}(z) = \frac{\Omega_{\rm DM}\rho_c(1+z)^3(1-f_{\rm coll}(z))f_{\rm PBH}}{M_{\rm PBH}}. \tag{5.3}$$

This expression shows that $n^{\rm IGM}_{\rm PBH}$ decreases with decreasing redshift. Besides cosmic expansion, this redshift evolution is due to the on-going structure formation, as more dark matter falls onto virialized halos, more PBHs are locked into DM halos than in the IGM.

PBHs in dark matter halos

The total amount of PBHs inside dark matter halos can be expressed, as a function of redshift, as:

$$n^{h}_{\rm PBH}(z) = \frac{\Omega_{\rm DM}\rho_c(1+z)^3 f_{\rm coll}(z) f_{\rm PBH}}{M_{\rm PBH}}. \tag{5.4}$$

To distribute PBHs into a DM halo of mass $M_{\rm vir}$, we assume that they follow a Navarro, Frenk & White (NFW, Navarro et al., 1997) density profile:

$$\rho_{\rm DM}(r) = \frac{\rho_c \delta_c}{cx(1+cx)^2}, \tag{5.5}$$

where $x = r/r_{\rm vir}$ denotes the radial distance in units of the virial radius $r_{\rm vir}$ (Barkana & Loeb, 2001):

$$r_{\rm vir} = 0.784 \left(\frac{M_{\rm vir}}{10^8\ h^{-1}\ M_\odot}\right)^{1/3} \left[\frac{\Omega_m}{\Omega^z_m}\frac{\Delta_c}{18\pi^2}\right]^{-1/3} \left(\frac{1+z}{10}\right)^{-1} h^{-1}\ {\rm kpc}, \tag{5.6}$$

where the overdensity relative to ρ_c at the collapse redshift can be expressed as $\Delta_c = 18\pi^2 + 82d - 39d^2$, with $d = \Omega^z_m - 1$ and $\Omega^z_m = \Omega_m(1+z)^3/(\Omega_m(1+z)^3 + \Omega_\Lambda)$; Δ_c is related to δ_c through the following relation:

$$\delta_c = \frac{\Delta_c}{3} \frac{c^3}{ln(1+c) - c/(1+c)} = \frac{\Delta_c}{3} \frac{c^3}{F(c)}, \tag{5.7}$$

where c is the concentration parameter that depends on $M_{\rm vir}$:

$$\log c = 1.071 - 0.098(\log M_{\rm vir} - 12). \tag{5.8}$$

The last relation is the result of N-body simulations developed by Macciò et al. (2007); in Appendix A.1, we discuss its applicability to low-mass ($M < 10^8 {\rm M}_\odot$)and high-redshift ($z > 6$) objects.

The total number of PBHs inside the halo can be computed by imposing that the halo mass is constituted of a fraction $f_{\rm PBH}$ of PBHs:

$$N_{\rm tot} = f_{\rm PBH} \left(\frac{M_h}{M_{\rm PBH}} \right). \tag{5.9}$$

The number of PBHs within any given radial distance is then given by:

$$N_{\rm PBH}(r) = f_{\rm PBH} \frac{4\pi}{M_{\rm PBH}} \int_0^r \rho_{\rm DM}(r') r'^2 dr'. \tag{5.10}$$

Fig. 5.1 shows the baryonic and DM density distributions (left axis), and the number of PBHs normalized to their total number (right axis), as a function of the radial distance from the center of the halo. According to our formalism, at a given redshift, less massive halos ($M_{\rm vir} = 10^3 M_\odot$) are more concentrated than more massive ones ($M_{\rm vir} = 10^9 M_\odot$); thus, 50% of $N_{\rm PBH}$ reside at smaller radial distances in the less massive halos ($0.3\, r_{\rm vir}$ vs. $0.5\, r_{\rm vir}$). Similarly, at a given fixed virial mass (e.g. $M_{\rm vir} = 10^6 M_\odot$), low redshift ($z = 6$) DM halos are more concentrated than high redshift ($z = 20$) ones. As a result, 50% of $N_{\rm PBH}$ reside at smaller radial distances in the less massive halos ($0.4\, r_{\rm vir}$ vs. $0.6\, r_{\rm vir}$).

5.2.2 PBH accretion

We assume that, both in the IGM and in halos, PBHs accrete according to the Bondi-Hoyle-Lyttelton model:

$$\dot{M}_{\rm PBH} = \lambda \frac{4\pi G^2 M_{\rm PBH}^2 \rho_{\rm gas}}{(c_{\rm s}^2 + v_{\rm BH}^2)^{3/2}}, \tag{5.11}$$

where G is the universal gravity constant, $\rho_{\rm gas}$ is the gas density, c_s is the sound speed, $v_{\rm BH}$ is the relative velocity between the black hole and the gas, and $\lambda = 0.01$ is the accretion eigenvalue, that accounts for non-gravitational effects in the process (Xie & Yuan, 2012). We prevent the gas accretion to exceed the Eddington rate $\dot{M}_E = L_E/(\varepsilon\, c^2)$, where L_E is the Eddington luminosity:

$$L_E = \frac{4\pi G M m_p c}{\sigma_T} = 1.3 \times 10^{38} \left(\frac{M_{\rm PBH}}{M_\odot} \right) {\rm erg\ s^{-1}}, \tag{5.12}$$

and $\varepsilon = 0.1$ is the assumed radiative efficiency[2].

PBH accretion in the IGM and inside halos proceeds in a considerably different manner (Ricotti et al., 2008a; De Luca et al., 2020). In what follows we characterize $\rho_{\rm gas}$, c_s, and $v_{\rm BH}$ in these two cases, separately.

[2]The value of the radiative efficiency is strongly dependent on the geometry of accretion, and can vary from $\varepsilon < 10^{-4}$, in the case of spherically symmetric accretion to $\varepsilon < 0.43$ for disk accretion processes (Shakura & Sunyaev, 1973; Shapiro, 1973)

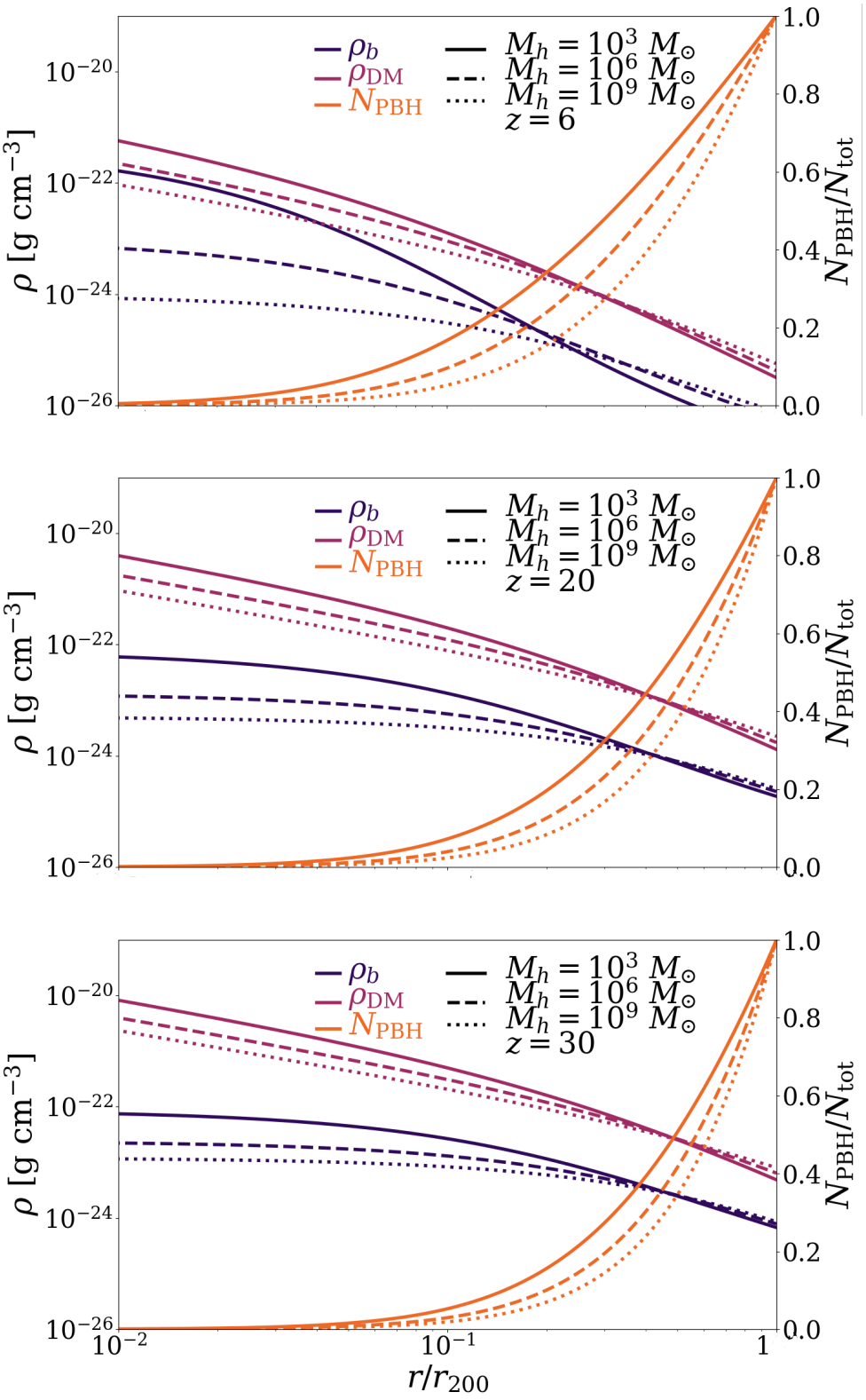

Figure 5.1: Baryon density, dark matter density, and PBHs integrated number as a function of the virial radius. Lines correspond to different halo masses. The solid, dashed, dotted line stays for a halo of mass $M_h = 10^3 \mathrm{M}_\odot$, $M_h = 10^6 \mathrm{M}_\odot$, $M_h = 10^9 \mathrm{M}_\odot$, respectively. Different colors represent different quantities: orange PBHs cumulative number, violet baryon density, purple dark matter density. The 3 panels present 3 redshifts: $z = 6, 20, 30$. PBHs mass is set at $30 M_\odot$.

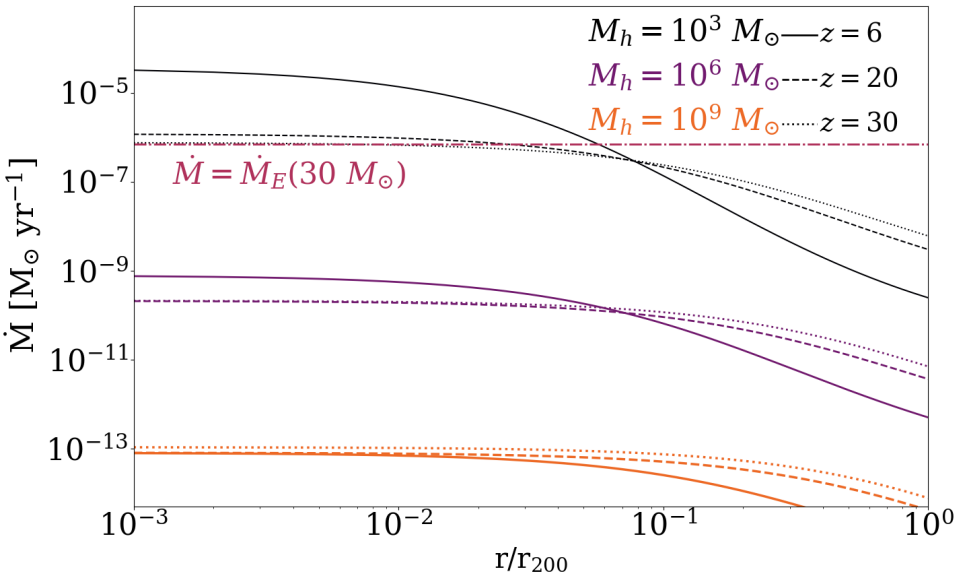

Figure 5.2: Accretion rate (for a single 30 $M_\odot$ black hole) as a function of the virial radius. The solid (dashed/dotted) line represents the redshift $z = 6$ ($z = 20/z = 30$). Different colors denote different halo masses: black $M_h = 10^3 \mathrm{M}_\odot$, violet $M_h = 10^6 \mathrm{M}_\odot$, and orange $M_h = 10^9 \mathrm{M}_\odot$. The horizontal purple line is the Eddington rate for a $30 M_\odot$ black hole.

PBH accretion in the IGM

Given the number density in eq. 5.4, the accretion from all the PBHs distributed in the IGM per comoving volume can be written as:

$$\dot{M}(z) = 4\pi\lambda G^2 M_{\rm PBH}^2 \frac{\rho_{\rm IGM}(z)}{[c_s(z)^2 + v_{\rm rel}(z)^2]^{3/2}} n_{\rm PBH}^{\rm IGM}(z), \tag{5.13}$$

where $\rho_{\rm IGM}$ is the gas density, c_s is the sound speed in the IGM, and $v_{\rm rel}$ is the relative velocity between dark matter and baryons. Following Ricotti et al. (2008b), we assume that PBHs in the IGM are surrounded by a uniform distribution of gas with density:

$$\rho_{\rm IGM} = 250\,\mu m_p \left(\frac{1+z}{1000}\right)^3 \ {\rm g\ cm^{-3}}, \tag{5.14}$$

where m_p is the proton mass and $\mu = 1.22$ is the mean molecular weight of a neutral gas of primordial composition. The IGM sound speed is

$$c_s = (k_B T_{\rm IGM}/\mu m_p)^{1/2}, \tag{5.15}$$

where k_B is the Boltzmann constant, and $T_{\rm IGM}$ is the gas temperature that depends on large scale effects, as discussed in Sec. 5.3.

For what concerns the relative velocity between dark matter and baryons, we adopt the relation proposed by Ali-Haïmoud & Kamionkowski (2017):

$$v_{\rm rel}(z) \simeq 30 \min\left[1, \left(\frac{1+z}{1000}\right)\right] {\rm km\ s^{-1}}. \tag{5.16}$$

PBH accretion in halos

Inside halos, the accretion rate strongly depends on the radial distance r:

$$\dot{M}_{\rm BHL}(r) = \lambda \frac{4\pi G^2 M_{\rm PBH}^2 \rho_{\rm gas}(r)}{(c_{\rm s}^2 + v_{\rm BH}^2)^{3/2}}. \tag{5.17}$$

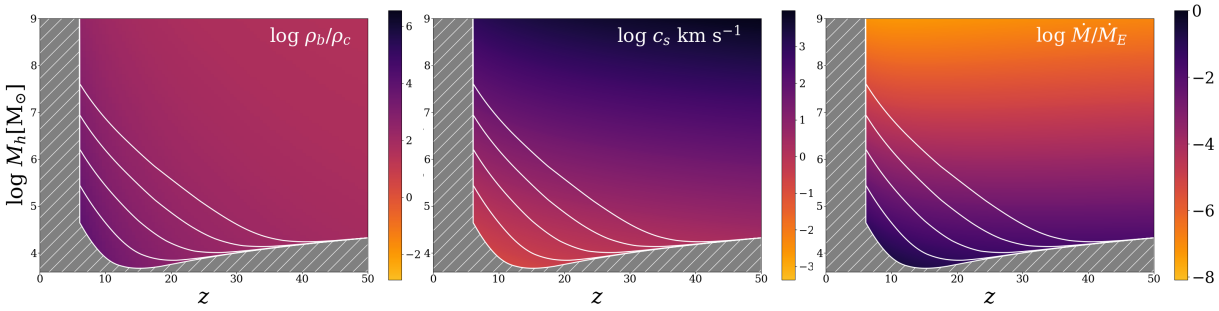

Figure 5.3: *Left panel*: baryon density (normalized to the critical density, ρ_c) as a function of halo mass, M_h, and redshift, z. *Middle*: same as left panel for sound speed, c_s. *Right*: same as left panel for the accretion rate of a 30 $M_\odot$ PBH (normalized to the Eddington rate). Note that accretion is more efficient in small halos at low redshift due to their higher density and lower sound speed. All values have been computed at $r = 0.01\, r_{\rm vir}$, where the baryon density and accretion rate reach their maximum. In each panel, the hatched grey regions represents the excluded region of the parameter space. The continuous white lines are an extension of the excluded region for the different $M_{\rm min}$ considered. We discuss how to select $M_{\rm min}$ in Sec. 5.3.

We adopt the gas density distribution from Makino et al. (1998):

$$\rho_{\rm gas} = \rho_0 \, \exp\left\{-\frac{\mu m_p}{2k_B T_{\rm vir}}[v_e^2(0) - v_e^2(r)]\right\}, \tag{5.18}$$

where $\rho_0(M)$ is the central gas density[3], $T_{\rm vir}$ is the virial temperature of the halo:

$$T_{\rm vir} = 1.98 \times 10^4 \left(\frac{\mu}{0.6}\right) \left(\frac{M_{\rm vir}}{10^8\, h^{-1}\, M_\odot}\right)^{2/3} \left[\frac{\Omega_m}{\Omega_m^z}\frac{\Delta_c}{18\pi^2}\right]^{1/3} \left(\frac{1+z}{10}\right) \, {\rm K}, \tag{5.19}$$

and v_e is the escape velocity that can be obtained through the following relations:

$$\begin{aligned} M(r) &= \int_0^r 4\pi\rho(r')r'^2 dr' = M_{\rm vir}\frac{F(cx)}{F(c)}, \\ v_c^2(r) &= \frac{GM(r)}{r} = v_{\rm c,vir}^2\frac{F(cx)}{F(c)}, \\ v_e^2(r) &= 2\int_r^{r_{vir}} \frac{GM(r')}{r'^2}dr' \approx 2v_c^2\frac{F(cx) + \frac{cx}{1+cx}}{xF(cx)}, \end{aligned}$$

where $F(c)$ is defined in Eq. 7.4, and $v_{\rm c,vir}^2 = GM_{\rm vir}/r_{\rm vir}$ is the circular velocity. We further assume that inside the halo the sound speed is constant and equal to:

$$c_s = (k_B T_{\rm vir}/\mu m_p)^{1/2} {\rm km\ s^{-1}} = 8.3\, T_{\rm vir,4}^{1/2}\ {\rm km\ s^{-1}}, \tag{5.20}$$

where $T_{\rm vir,4}$ is the virial temperature in units of 10^4 K. We finally set to zero the relative velocity between PBHs and baryons, assuming that dark matter and baryons are in hydrodynamical equilibrium.

[3]The constant ρ_0 is set such that $M_b = (\Omega_b/\Omega_m)M_h$.

In Fig. 5.2, we show how the accretion rate varies within the virial radius, for different halo masses and redshifts. For a fixed halo mass, the accretion rate is higher at low redshift; for a fixed redshift, the accretion rate is higher for less massive halos. To understand these trends, in the left and middle panels of Fig. 5.3 we plot the redshift and M_h dependence of the gas density and sound speed, which govern the PBH accretion rate (eq. 5.17). For illustration, both quantities are computed at $r = 0.01 r_{\rm vir}$. The baryon overdensity ρ_b/ρ_c inside halos remains almost constant around a value $\simeq 100$ along cosmic history, but slightly increases for low z and/or small DM halos. Instead, the sound speed decreases both with halo mass and redshift.

These two combined effects, explain the results shown in the right panel of Fig. 5.2, where the accretion rate at $r = 0.01\ r_{\rm vir}$ is shown as a function of M_h and z. Accretion is more efficient in the central region of low mass halos ($M \leq 10^6 M_\odot$), at any given z. In these objects, accretion is so efficient that it compensates the reduced total number of PBHs that scales linearly with M_h (Eq. 5.9). Given that small halos are also more numerous relative to more massive ones, we expect their PBH emission to be dominant.

5.2.3 X-ray and radio luminosity

Given the bolometric luminosity $L_{\rm B} = \varepsilon \dot{M} c^2$ of an accreting PBH, the X-ray luminosity (L_X) can be computed by means of a bolometric correction f_X, i.e.

$$L_X = f_X L_{\rm B}. \tag{5.21}$$

Following Ewall-Wice et al. (2018), we assume $f_X = 0.1$ in the $2 - 10$ keV band (see also Poulin et al., 2017; Mena et al., 2019; Villanueva-Domingo & Ichiki, 2021). We model the X-ray spectra of accreting PBHs with a power-law with an exponential cut-off at high energies (Poulin et al., 2017; Mena et al., 2019; Villanueva-Domingo & Ichiki, 2021), and compute the specific luminosity in the X-ray band ($L_{X,\nu}$) as:

$$L_{X,\nu} \propto \nu^{-\alpha} e^{(-\nu/\nu_{\rm cut})}, \tag{5.22}$$

where[4] $\alpha = 0.7$ is the spectral index in the X-ray band, and ν_{cut} is the cut-off frequency.

For what concerns the radio luminosity L_R, we assume the fundamental plane relation (Gallo et al., 2003; Merloni et al., 2003; Wang et al., 2006). In particular, following Hasinger (2020a), we adopt the relation found by Wang et al. (2006), based on the radio luminosity measured at 1.4 GHz and the X-ray luminosity in the 0.1-2.4 keV band:

$$\begin{aligned} &\log\left(\frac{L_R}{10^{40}\text{erg s}^{-1}}\right) = \\ &= 0.85 \log\left(\frac{L_X}{10^{44}\text{erg s}^{-1}}\right) + 0.12 \log\left(\frac{M_{\rm PBH}}{10^8 \text{M}_\odot}\right). \end{aligned} \tag{5.23}$$

We finally assume for the radio luminosity a typical spectral index of syncrothron emission, $L_{R,\nu} \propto \nu^{-0.6}$.

5.2.4 Background intensity

The comoving specific emissivity due to PBHs accreting in the IGM can be written as:

$$\dot{\rho}_{\rm IGM}(\nu, z) = L_\nu(z) n_{\rm IGM}(z)\ \text{erg s}^{-1}\ \text{Mpc}^{-3}\text{Hz}^{-1}. \tag{5.24}$$

[4]Typical values of spectral indices in the X-ray band are in the range $\alpha = [0.7, 1.3]$ (Yuan & Narayan, 2014)) and $\nu_{\rm cut}$ is the cut-off frequency, such that $h\nu_{\rm cut} = 200$ keV.

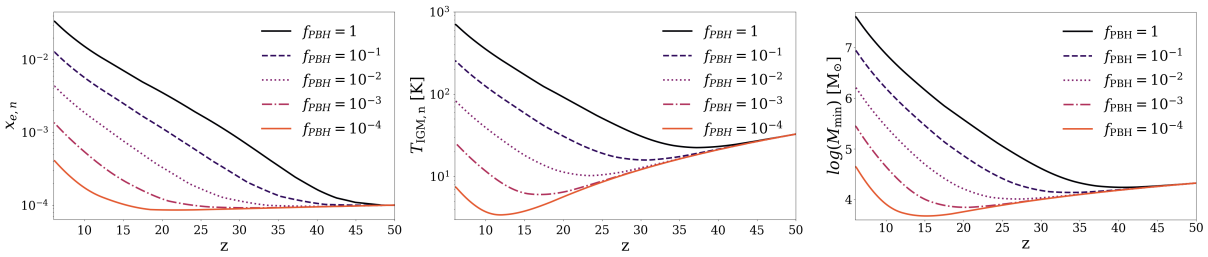

Figure 5.4: IGM ionized fraction (left panel), Temperature (middle panel), Minimum mass (right panel) evolution with redshift inside neutral regions. Different colors represent different $f_{\rm PBH}$ values: black continuous line $f_{\rm PBH} = 1$, violet dashed line $f_{\rm PBH} = 10^{-1}$, purple dotted line $f_{\rm PBH} = 10^{-2}$, red dashed-dotted line $f_{\rm PBH} = 10^{-3}$, and orange continuous line $f_{\rm PBH} = 10^{-4}$. We maintain this line style and color code thorough the rest of this paper. In all three panels a PBHs mass of 30 $M_\odot$ is assumed.

where ν is the (rest-frame) frequency, and L_ν represents the X-ray or radio specific luminosity computed with the formalism described in the previous section. For what concerns the emissivity from halos, $\dot{\rho}_h$, we first compute the integrated luminosity from a single object of mass $M_{\rm vir}$:

$$L_\nu(M_{\rm vir}) = \int_0^{r_{\rm vir}} L_\nu(r') n_{\rm PBH}(r') dr', \tag{5.25}$$

and then we integrate over the halo mass function (Murray et al., 2013):

$$\dot{\rho}_h(\nu, z) = \int_{\rm M_{min}}^{M_{\rm max}} L_\nu(M', z)\, n_h(M', z) dM', \tag{5.26}$$

where $n_h(M, z)$ gives the number of halos of mass M at redshift z, $M_{\rm max} = M_h(T_{\rm vir} = 10^4{\rm K})$ is the minimum DM halo mass for star formation to happen, and $M_{\rm min}$ is the minimum mass of DM halos that can virialise and form a baryon overdensity:

$$M_{\rm min}(T_{\rm IGM}, z) = 1.3 \times 10^3 M_\odot \left(\frac{10}{1+z}\right)^{3/2} \left(\frac{T_{\rm IGM}(z)}{1\ {\rm K}}\right)^{3/2}. \tag{5.27}$$

The latter depends on the IGM temperature evolution and will be computed in Sec. 5.3.2.

Finally, we proceed to compute the background intensity, $I_{\rm PBH}$, as follows:

$$I_{\rm PBH}(\nu, z) = \frac{c(1+z)^3}{4\pi\nu} \int_z^\infty \frac{\dot{\rho}(\nu, z')}{(1+z')H(z')} dz', \tag{5.28}$$

where $H(z)$ is the Hubble parameter. Usually, in the radio frequency range the background intensity, I, is more conveniently expressed in terms of the brightness temperature, T_b:

$$T_b(\nu, z) = \frac{I(\nu, z)c^2}{2k_B\nu^2}. \tag{5.29}$$

5.3 IGM Heating and Ionization by PBHs

Radiation emitted by accreting PBHs is injected into the IGM, thus heating and ionizing the gas. The background intensity described in the previous section can be used to self-consistently account for these large scale effects.

To compute the amount of energy injected into the IGM by the X-ray emission we follow the formalism described in Mesinger et al. (2013). The heating rate per baryon, $\epsilon_{\rm PBH}$, is a function of the X-ray background produced by PBHs, and can be expressed as:

$$\epsilon_{\rm PBH}(z) = \int_{\nu_{\rm min}}^{\infty} d\nu \frac{4\pi I_\nu}{h\nu}(h\nu - E^{th}) f_{\rm heat}\sigma_H(\nu), \tag{5.30}$$

where $h\nu_{\rm min} = 0.5$ keV, I_ν is the angle-averaged specific-intensity X-ray background, E^{th} is the ionization threshold, $f_{\rm heat} = 0.3$ is the fraction of primary electron energy going into heat (Furlanetto & Stoever, 2010), and σ_H is the hydrogen ionization cross section.

We then compute the impact of X-ray photons from accreting PBHs on the heating[5] and ionization of the IGM, following (Puchwein et al., 2019). The evolution of the IGM ionized fraction x_e and temperature $T_{\rm IGM}$ are computed by solving the following coupled differential equations:

$$\frac{dx_e}{dz} = \frac{dt}{dz}[\Gamma - \alpha_R(T) C x_e^2 n_b], \tag{5.31a}$$

$$\begin{aligned}\frac{dT_{\rm IGM}(z)}{dz} =& \frac{2}{3k_B(1+x_e)}\frac{dt}{dz}\sum_i \epsilon_i \\ &+ \frac{2T_{\rm IGM}}{3n_b}\frac{dn_b}{dz} - \frac{T_{\rm IGM}}{1+x_e}\frac{dx_e}{dz},\end{aligned} \tag{5.31b}$$

where Γ is the photoionization rate, α_R is the case A recombination coefficient , $C = 2$ is the clumping factor (Mesinger et al., 2013), n_b is the mean baryon density, and ϵ_i is the heating rate per baryon per process i.

To properly evaluate PBHs accretion in the pre-overlap phase of the cosmic reionization process, we solve the above coupled differential equations separately for the ionized and neutral regions. The assumption of volume-averaged values for the IGM temperature and ionized fraction would lead to a miss evaluation of the gas accretion onto PBHs, and subsequently of their emission.

5.3.1 Ionized regions

We fix the IGM temperature in the ionized regions to $T_{\rm IGM,ion} = 10^4$ K; the coupled differential equations then become:

$$\frac{dx_{\rm e,ion}}{dz} = \frac{dt}{dz}[\Gamma - \alpha_R C x_{\rm e,ion}^2 n_b], \tag{5.32a}$$

$$\frac{dT_{\rm IGM,ion}(z)}{dz} = 0. \tag{5.32b}$$

In the case of ionized regions, PBHs accretion is strongly suppressed because of the increased sound speed. The redshift evolution of the ionized fraction $x_{\rm e,ion}$ traces the evolution of the volume filling factor of ionised regions, namely the fraction of volume occupied by ionized regions. We rewrite the IGM number density of PBHs dividing the ionized and neutral components as follows:

$$n_{\rm IGM}(z) = n_{\rm IGM}(z) x_{\rm e,ion}(z) + n_{\rm IGM}(z)(1 - x_{\rm e,ion}(z)). \tag{5.33}$$

[5]We neglect the impact of UV ionizing radiation emitted by PBHs (see Appendix A.2)

5.3.2 Neutral regions

In the case of neutral regions, the coupled equations can be written as follows:

$$\frac{dx_{\rm e,n}}{dz} = \frac{dt}{dz}[\Gamma_{\rm PBH} - \alpha_R(T_{\rm IGM,n})Cx_{\rm e,n}^2 n_b], \tag{5.34a}$$

$$\begin{aligned}\frac{dT_{\rm IGM,n}(z)}{dz} =& \frac{2}{3k_B(1+x_e)}\frac{dt}{dz}\epsilon_{\rm PBH} \\ &+ \frac{2T_{\rm IGM,n}}{3n_b}\frac{dn_b}{dz} - \frac{T_{\rm IGM}}{1+x_e}\frac{dx_{\rm e,n}}{dz},\end{aligned} \tag{5.34b}$$

where $x_{\rm e,n}$ represents the fraction of free electrons in neutral regions, and $\Gamma_{\rm PBH}$ is the ionization rate due to PBH X-ray emission. PBHs accreting in neutral regions represent the main contributors to the cosmic backgrounds, because of their lower gas temperature that both lowers the sound speed (thus increasing the accretion rate) and allows mini-halos to virialise more easily. In neutral regions, the sole heating and ionizing contribution comes from X-ray photons, since UV photons are easily absorbed by neutral hydrogen, while X-rays can penetrate larger gas column densities before getting absorbed.

The resulting IGM ionized fraction and temperature evolution in the neutral regions is shown[6] in the left and middle panel of Fig. 5.4, respectively. This figure clearly shows that the impact of accreting PBHs on the global thermal and ionization history of the early Universe would be particularly relevant if dark matter were completely composed of PBHs ($f_{\rm PBH} = 1$): in this case, the IGM ionized fraction and temperature would increase by a factor of about 50 at $z \sim 6$; for lower values ($f_{\rm PBH} = 10^{-2}$) the increment of x_e and $T_{\rm IGM}$ would be limited to a factor of few.

Finally, in the right panel of Fig. 5.4, we show the $\rm M_{min}$ evolution with redshift taking into account the IGM temperature evolution before reionization[7]. As a consequence of X-ray heating by PBHs, also $M_{\rm min}$ increases. In particular, $M_{\rm min}$ appears to be more strongly affected by the presence of accreting PBHs: in the case of $f_{\rm PBH} = 1$ ($f_{\rm PBH} = 10^{-2}$), $M_{\rm min}$ increases by factor of 1000 (10). This trend is shaped by the following combined effects: on the one hand, the relation between $M_{\rm min}$ and $T_{\rm IGM}$ is nonlinear ($M_{\rm IGM} \propto T_{\rm IGM}^{3/2}$); on the other hand, an higher value of $M_{\rm min}$ shorten the integration interval in eq. 5.26, thus reducing the resulting PBH X-ray emission from eq. 5.28.

5.4 Results

In this Section, we constrain the fraction of dark matter in the form of PBHs by computing the contribution of PBHs to the CXB, the CRB, and the 21-cm signal. The PBH contribution to CXB and CRB can be evaluated at different epochs. Here, we compare our cumulative model predictions at $z = 0$ with the observed CXB and CRB to test to which extent the extra radiation from accreting PBHs can explain the observed excesses in the CXB and CRB. Furthermore, we constrain the possible contribution of PBHs to the CRB at $z = 17$, namely the epoch at which the H I21 cm signal detected by the EDGES experiment shows a deep absorption feature.

[6] We limit our analysis at redshift $z = 6$ since, according to our model (Puchwein et al., 2019), this epoch sets the end of the reionization process; thus at lower redshifts the IGM is completely ionized.

[7] The minimum halo mass after reionization is fixed to $M_{\rm min} = M_h(T_{\rm vir} = 10^4\ {\rm K})$.

5.4.1 X-ray background

About $\sim 70\%$ of the CXB arises from resolved sources (mostly AGN) both in the soft and hard bands (Cappelluti et al., 2017). The remaining contribution from unresolved sources can be attributed to a still unknown BH population (e.g., accreting BHs in heavily obscured conditions, Gilli et al. 2007; Treister et al. 2009) and additional unresolved sources (e.g., extended X-ray emission from galaxy clusters Gilli et al. 1999). To test the hypothesis that PBHs provide the origin of such unresolved background, we quantify their contribution to the X-ray background in the soft ($0.5-2$ keV) and hard ($2-10$ keV) X-ray bands by using Eq. 5.28.

In Fig. 5.5, we compare our predictions as a function of $f_{\rm PBH}$ with observational limits reported in Cappelluti et al. (2017). The authors analyzed Chandra data (COSMOS-Legacy survey, Elvis et al., 2009; Civano et al., 2016) finding a XRB intensity at 1 keV to be $10.91 \pm 0.16\,\mathrm{keV\ cm^{-2}s^{-1}deg^{-2}}$ and spectral index $\Gamma = 1.45 \pm 0.02$. After subtracting the X-ray detected sources they found that the unresolved CXB intensity in the soft band[8] ($I_{0.5-2\rm keV} = 2.90 \times 10^{-12}\,\mathrm{erg\,s^{-1}cm^{-2}deg^{-2}}$) is smaller than in the hard band ($I_{2-10\rm keV} = 6.47 \times 10^{-12}\,\mathrm{erg\,s^{-1}cm^{-2}deg^{-2}}$). We thus consider the soft band data to obtain the most stringent constraints on $f_{\rm PBH}$.

For high values of $f_{\rm PBH}(\gtrsim 0.1)$, the contribution of accreting PBHs to the soft CXB rises steeply at early epochs: for example, assuming $f_{\rm PBH} = 1$, the X-ray emission from $z > 40$ PBHs already overshoots the observed CXB. The integrated contribution of PBHs flattens below a critical redshift which depends on $f_{\rm PBH}$. For example, for $f_{\rm PBH} = 10^{-1}$ ($f_{\rm PBH} = 10^{-3}$) the PBHs cumulative emission reaches the value of 1 (10) $\mathrm{erg\ s^{-1}\ cm^{-2}\ deg^{-2}}$ at $z \sim 20$ ($z \sim 10$) and remains almost constant afterwards. This trend is related to the redshift evolution of $M_{\rm min}$ (right panel of Fig. 5.4), that rises more rapidly with $f_{\rm PBH}$, as a consequence of a more efficient X-ray heating from PBHs. We find that our predictions are consistent with Chandra data only if $f_{\rm PBH} \leq 3 \times 10^{-4}$. Independently from $f_{\rm PBH}$, the PBHs contribution to the XRB drops after the reionization epoch ($z < 6$), since both the high gas temperature ($> 10^4$ K), and the small filling factor of neutral regions make PBHs accretion extremely inefficient.

In Fig. 5.6 we present the redshift evolution of the ratio between the soft X-ray intensity arising from halos ($I_{X,h}$, black line) or from the IGM ($I_{X,\rm IGM}$, orange line) and the total intensity($I_{X,\rm tot}$). At very early epochs ($z > 40$), the total signal is always dominated by IGM contribution. At $z \sim 40$, the two curves cross each other, as density perturbations start to collapse into virialized structure. At later epochs, the total X-ray intensity is dominated by emission from PBHs in DM halos, whereas PBHs in the IGM provides only a minor contribution ($\lesssim 5\%$). We stress that 99% of the signal arises from mini-halos ($M_h \leq 10^6\ M_\odot$), whose X-ray emissivity peaks at $z \sim 6$. Independently from the value of $f_{\rm PBH}$ the total signal is dominated by the emission produced into halos, up to a maximal ratio of $I_h/I_{\rm IGM} \sim 50$ for $f_{\rm PBH} = 10^{-4}$. The contribution from PBH accreting in the IGM increases with $f_{\rm PBH} = 1$, although remaining subdominant, as a consequence of the X-ray heating feedback: as the minimum mass increases, $f_{\rm coll}$ decreases, thus raising the PBHs number density into the IGM.

In Table 5.1, we report our prediction for the background intensity in the soft and hard X-ray bands for different values of $f_{\rm PBH}$[9]. The predicted intensity appear to be stronger in the soft band for $f_{\rm PBH} \leq 10^{-3}$, and vice versa. We attribute this effect to the exponential cut-off (at 200 keV) in the X-ray spectrum that suppresses contribution from high redshift to the hard band. In the case of a shallower intensity evolution (high values of $f_{\rm PBH}$, see Fig. 5.5) a non-negligible

[8] In Cappelluti et al. (2017) two different values are reported for the CXB, one from *unresolved* sources and one called *non-source*. The latter one refers to the observed intensity obtained when both X-ray and HST-ACS observed sources are masked. We compare our predicted value with the *non-source* CXB intensity.

[9] As discussed in Sec. 5.2.3 the spectral index adopted for this work in the X-ray band is $\alpha = 0.7$, which is slightly steeper than the one corresponding to the background excess $\alpha = 0.57$.

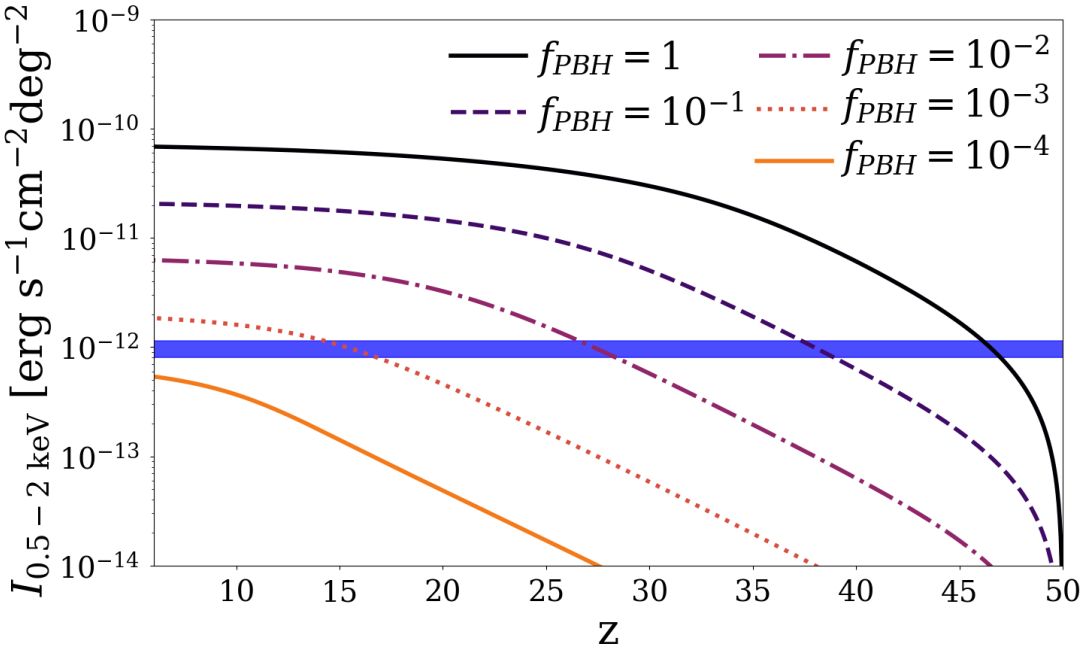

Figure 5.5: Integrated soft X-ray background intensity $I_{0.5-2\mathrm{keV}}$ cumulative evolution, for different values of f_{PBH} as reported in the legend. The blue shaded regions represent the observed excess background (Cappelluti et al., 2021). The background intensities are computed for $M_{\mathrm{PBH}} = 30 M_{\odot}$.

fraction of the total radiation in the hard band is produced in the redshift interval $20 \lesssim z \lesssim 30$. For $f_{\mathrm{PBH}} \leq 10^{-3}$ the radiation feedback is not strong enough to suppress the signal at early epochs ($20 \lesssim z \lesssim 30$) resulting in a steeper evolution of the CXB intensity, and consequently a lower contribution to the hard band from high redshift ($z > 20$).

5.4.2 Radio background

The observed background radio-excess is well fitted with a power-law spectrum between 22 MHz and 10 GHz (Condon et al., 2012):

$$T_b = (24 \pm 2.1\mathrm{K}) \times \left(\frac{\nu}{310\ \mathrm{MHz}}\right)^{-2.599 \pm 0.036} . \tag{5.35}$$

Table 5.1: X-ray background intensity in units of $10^{-12}\mathrm{erg\ s^{-1}\ cm^{-2}\ deg^{-2}}$. We report our predictions for soft ($0.5 - 2$ keV) and hard ($2 - 10$ keV) X-ray bands for the values of f_{PBH} considered in this work.

f_{PBH}	$I_{0.5-2\mathrm{keV}}$	$I_{2-10\mathrm{keV}}$
1	68.2	81.2
0.1	20.0	22.2
0.01	6.01	6.21
10^{-3}	1.80	1.74
10^{-4}	0.52	0.47

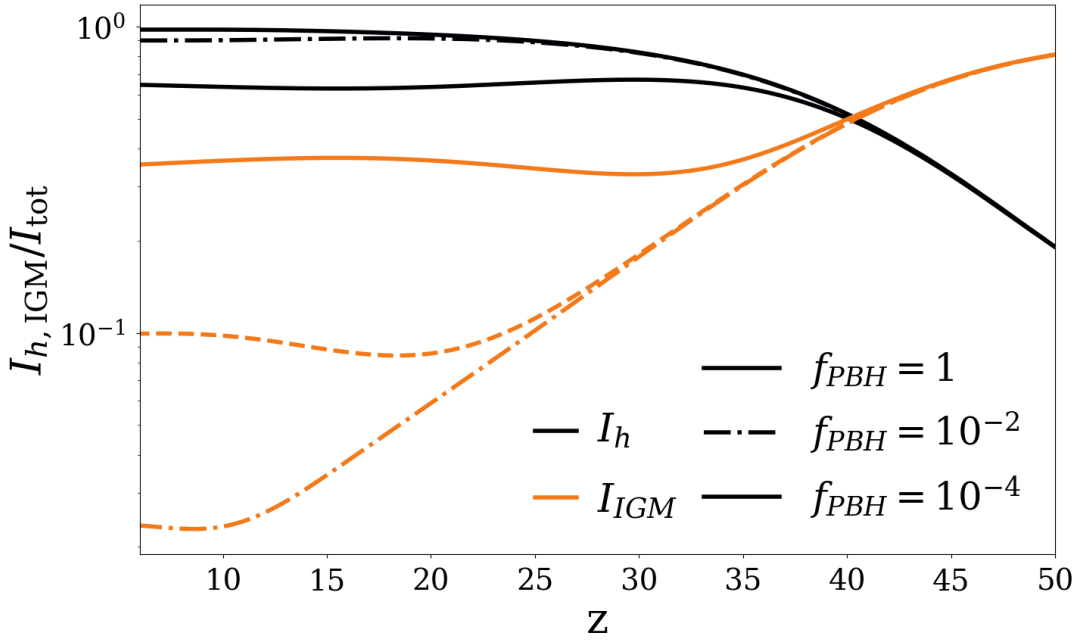

Figure 5.6: Redshift evolution of the relative contribution to the soft ($0.5 - 2$ keV) X-ray background from halos and IGM, $I_h/I_{\rm tot}$ and $I_{\rm IGM}/I_{\rm tot}$, respectively. Different line styles correspond to different $f_{\rm PBH}$, as shown in the label. Black (orange) lines correspond to the halos (IGM) contribution. The relative background intensities are computed for $M_{\rm PBH} = 30 M_\odot$.

In our model, the X-ray emission in the accretion process is associated to jet production and thus to radio emission (see Sec. 5.2.3). We thus compute the contribution of PBHs to the radio background at 1.4 GHz, at redshift $z = 0$, and compare our results with ARCADE2 data ($480\,\mathrm{mK}$). In Fig. 5.7, we show the brightness temperature of the radio background, as predicted by our calculations, at varying $f_{\rm PBH}$. The amplitude of the radio background increases sub-linearly with $f_{\rm PBH}$ (see also Tab. 5.2), while the shape assumed for synchrotron emission fairly reproduces observations, and does not depend on $f_{\rm PBH}$.

In the case $f_{\rm PBH} = 1$, the PBHs contribution to the CRB would represent 92% of the observed excess, thus explaining most of the unexplained signal. However, if we take into account CXB constraints, PBHs cannot explain the radio excess, since they would contribute only 1% to the CRB.

5.4.3 21 cm signal

The radio background due to accreting PBHs may affect the amplitude of the 21-cm global signal. The absorption depth of the signal can be computed as follows (Mesinger et al., 2013):

$$\begin{aligned}\delta T_b =& 27 x_{\rm HI}(1+\delta)\left(\frac{\Omega_b h^2}{0.023}\right)\left(\frac{0.15}{\Omega_m h^2}\frac{1+z}{10}\right)^{1/2} \\ & \frac{\partial_r v_r}{H(z) 1+z}\left(1-\frac{T_r}{T_s}\right),\end{aligned} \tag{5.36}$$

where $x_{\rm HI} = 1 - x_e$ is the neutral hydrogen fraction, $\partial_r v_r$ is the comoving gradient of the line of sight component of the comoving velocity, T_r is the radio background temperature, T_s is the spin temperature. Fialkov & Barkana (2019) pointed out that, given a radio background of amplitude

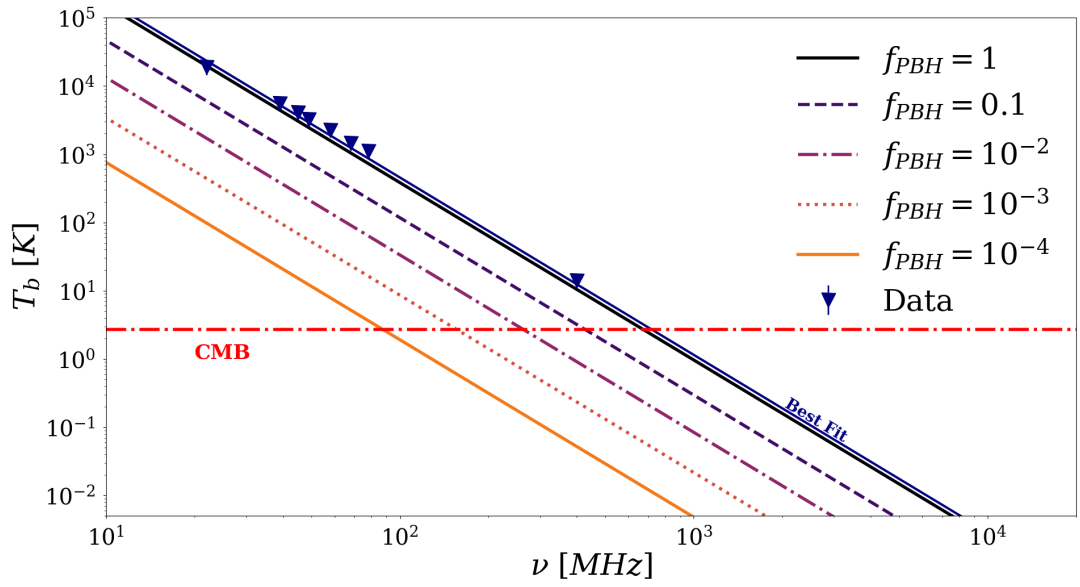

Figure 5.7: Radio background brightness temperature at $z = 0$ as a function of frequency for the values of $f_{\rm PBH}$ considered in the work. The blue triangles represent the data points (Condon et al., 2012); the continuous blue line is the best fit for the same data. The horizontal red dotted dashed line shows the CMB temperature. The brightness temperature is computed at 1.4 GHz for PBHs of 30 $M_\odot$.

$\rm A_r$ in addition to the CMB, the radio background temperature can be written as follows:

$$T_r = T_{\rm CMB}(1+z)\left[1 + A_r\left(\frac{\nu_{\rm obs}}{78\ \rm MHz}\right)^{-2.6}\right], \tag{5.37}$$

where $\nu_{\rm obs}$ is the observed frequency by the EDGES instrument at 78 MHz, which corresponds to $z = 17$. Thus, the presence of a radio background in addition to the CMB, may push the absorption signal to larger depths, possibly explaining the results obtained with the EDGES experiment (Mirocha & Furlanetto, 2019). In particular, to recover an absorption signal consistent with EDGES, an extra radio background with an amplitude $A_r > 1.9$ is required.

In Tab. 5.2, we report our predictions on the brightness temperature of the 21 cm at $z = 17$, as predicted by our calculations, varying $f_{\rm PBH}$: for $f_{\rm PBH} = 1$ ($f_{\rm PBH} = 10^{-4}$), we obtain $A_r = 10$ (0.01); in order to reproduce the entire EDGES absorption feature, $f_{\rm PBH} \gtrsim 4 \times 10^{-2}$ is required. However this value would exceed the constraints derived from the CXB. The maximum value allowed by the CXB provides $T_R = 0.59$ K: this radio background temperature can explain only 1% of the entire EDGES signal.

We point out that our result can be modified by further modeling the physics of the 21-cm signal (e.g. the impact of PBHs radiation on T_s via Lyman-α coupling). Even if our results only provide a first order of magnitude estimate, we do not expect the PBHs contribution to the 21-cm signal to be relevant even with further improvement of the model.

5.5 PBHs as dark matter: constraints

Fig. 5.8 summarises the main results of this work and compares them with previous ones in the literature. Dashed lines in the plot show existing constraints from the accretion process. The line labelled "dwarf galaxy heating" refers to the results obtained in Lu et al. (2021) through the analysis of gas heating due to PBHs accretion. Manshanden et al. (2019) modeled the X-ray and

Table 5.2: Predictions for the radio background brightness temperature (in units of [K]), both at $z = 0$, and $z = 17$ for the values of $f_{\rm PBH}$ considered in this work.

$f_{\rm PBH}$	$T_b(z = 0)$/K	$T_b(z = 17)$/K	A_r
1	0.402	579.67	11.80
0.1	0.123	174.42	3.55
0.01	0.035	42.81	0.87
10^{-3}	0.009	7.59	0.15
10^{-4}	0.002	1.10	0.02

radio emission from accreting PBHs in the Milky Way. Source counting in those bands only allows for a small fraction ($f_{\rm PBH} \leq 10^{-3}$) in the $10 \leq M_\odot \leq 100$ mass range.

The EDGES-21cm marks the constraints by Hektor et al. (2018), who evaluated the impact of heating and ionization from PBHs accreting in the IGM only[10], by imposing that $T_{\rm IGM}(z = 17) \leq 8$ K.

The most stringent constraint in the considered mass range ($1M_\odot \leq M_{\rm PBH} \leq 10^3 M_\odot$) has been set by Serpico et al. (2020), who evaluated the impact of PBHs energy production on CMB anisotropies. In their work they considered two different models for PBHs accretion, assuming either spherical or disk accretion, finding two different upper limits on $f_{\rm PBH}$. In the case in which PBHs are not the sole constituent of DM, $f_{\rm PBH} < 1$, the authors modeled PBH-DM interaction, and assumed a dark matter halo to form around each PBH. This effect was already discussed in Ricotti et al. (2008a), and it results in a time-increasing halo mass surrounding the PBH, $M_h(z) = (3000/1 + z)M_{\rm PBH}$. The result is a boost factor of PBH accretion rate of $\sim 10^2$ at ($z = 10$). We do not account for PBH-DM interaction in the case $f_{\rm PBH} < 1$, and note that accounting for it would strengthen our results, boosting PBHs accretion and consequently the CXB and CRB contributions. Even in the absence of PBH-DM interaction we can set the strongest constraint at $M_{\rm PBH} = 30M_\odot$.

We show in Fig. 5.8 the upper bound on $f_{\rm PBH}$ as a function of PBHs mass, and the new, strong constraint $f_{\rm PBH} \leq 3 \times 10^{-4}(30M_\odot/M_{\rm PBH})$ from the X-ray background. The dependence $M_{\rm PBH}^{-1}$ follows from the halo X-ray luminosity relation, $L_X \propto M_{\rm PBH}^2/M_{\rm PBH} \propto M_{\rm PBH}$, where the factor $M_{\rm PBH}^2$ $(1/M_{\rm PBH})$ arises from black hole accretion (number density of PBHs in the halo). In Fig. 5.8 we also show the lower limit required to recover the EDGES depth as a blue dashed line. We note that the entire region is excluded by the X-ray background constraint. We stress that we set the strongest constraint on $f_{\rm PBH}$ by comparing the predicted value of the soft CXB with the observed one. PBHs are thus unable to contribute significantly to the CRB at any epochs, and consequently their emission is unable to affect the global 21-cm signal.

We briefly comment on the implication of the new constraint on extended PBHs mass distributions (e.g. Carr et al. 2019; Jedamzik 2021). Several multi-peaked mass functions present their main peak at $\sim 1\ M_\odot$. Constraining the low-end of the solar mass window implies that we limit the height of the main peak at $f_{\rm PBH} \sim 10^{-2}$, value which is typically overshoot. This would imply a reconsideration of some properties (e.g height and location of the main peak) for those mass distributions. We stress that to properly evaluate the impact of our analysis on extended mass distributions the approximation of a monochromatic PBHs spectrum has to be relaxed.

[10] We underline that in our work we instead take into account PBH accretion in halos as well.

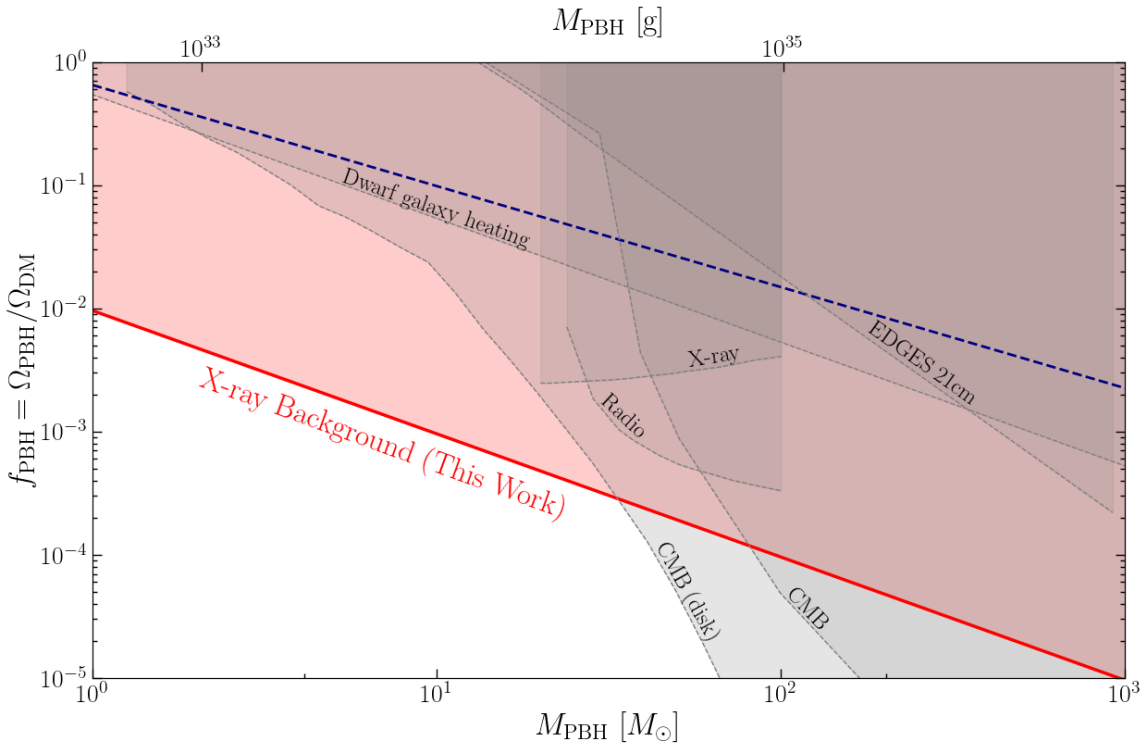

Figure 5.8: Constraints on $f_{\rm PBH}$ derived taking into account PBHs accretion. The red solid line represents the constraint obtained in this work from the cosmic X-ray background. The blue dashed line defines the minimum $f_{\rm PBH}$ value to recover the EDGES signal depth. Dashed gray lines correspond to existing constraints: (a) dwarf galaxy heating: derived by evaluating the impact of gas heating due to PBHs accretion in dwarf galaxies (Lu et al., 2021); (b) X-ray and radio: obtained through the comparison of the number of X-ray and radio emitters in the Milky way center and the predicted number by a PBHs accreting model from Manshanden et al. (2019); (c) CMB: derived by evaluating the impact of radiation emitted by PBHs on CMB anisotropies assuming spherical or disk accretion (Serpico et al., 2020); (d) EDGES 21cm: computed by considering the impact of heating feedback from PBHs accretion on the IGM, and comparing the results with the predicted value (Hektor et al., 2018). Figure created by modifying the publicly available Python code PBHbounds (Green & Kavanagh, 2021).

5.6 Summary

In this work, we presented a new semi-analytical model to compute the accretion rate and the relative luminosity of PBHs in dark matter halos and in the IGM, and explored the possibility that radiation emitted by accreting PBHs could contribute to the X-ray (CXB) and radio (CRB) backgrounds. Our main results are the following:

1. By comparing the cumulative X-ray emission from PBHs predicted by our model with the observed CXB, we set the strongest existing constraint on $f_{\rm PBH} \leq 3 \times 10^{-4}\ (30/M_{\rm PBH})$ in the mass range $1 - 1000\ M_\odot$.

2. We compare the PBH radio emission predicted by our model with the measured 21cm line feature and CRB. In the first case the extra radio background is able to recover only a fraction $f = 1\%$ of the absorption depth claimed by Bowman et al. (2018). Similarly, the allowed brightness temperature $T_b(1.4\ \text{GHz}) \sim 0.004$ K represents only a fraction $f \sim 1\%$ of the radio excess observed by ARCADE2.

3. Depending on the minimum halo mass considered, we show that the contribution from PBHs accreting into DM halos dominates over those accreting from the IGM ($60\% < I_h/I_{\rm tot} < 99\%$).

4. Most of the CXB/CRB emission is produced by PBHs in DM mini-halos ($M_h \leq 10^6\ M_\odot$) at early epochs ($z > 6$).

5. We also evaluated the impact of PBHs radiation on the thermal state of the IGM. We find that the X-ray heating impacts the IGM temperature in neutral regions and consequently the minimum halo mass. This effect introduces a nonlinear dependence of the background intensity on $f_{\rm PBH}$.

As a final caveat, we stress that we have assumed a monochromatic PBH mass function; in future work this assumption can be relaxed. An additional assumption concerns the use of a standard ΛCDM halo mass function. For consistency, one should include the modifications induced by the presence of a fraction $f_{\rm PBH}$ of dark matter in the form of PBHs. We do expect this inclusion to boost the number of mini-halos. As these are the major contributors to the CXB and CRB, we predict that the upper limits on $f_{\rm PBH}$ could be pushed to even smaller values.

Primordial black holes as Near Infrared background sources

6

6.1 Introduction

Given the puzzling nature of the NIRB excess, a new scenario has been recently suggested, invoking Primordial Black Holes (PBHs) (Kashlinsky, 2016b; Cappelluti et al., 2022). PBHs are black holes formed deep into radiation dominated era from the collapse of overdensity peaks (Zel'dovich & Novikov, 1966; Carr & Hawking, 1974) and interest on them have been rejuvenated after the first detection of gravitational waves from black holes merger (Abbott et al., 2016; Bird et al., 2016; Blinnikov et al., 2016; Sasaki et al., 2016). The primordial origin of LIGO/VIRGO black holes is a viable solution to explain their observed mass spectrum and merger rates (Raidal et al., 2017; Ali-Haïmoud et al., 2017; Wong et al., 2021). Moreover, they could justify why most of the measured effective spins are close to zero (Abbott et al., 2019; De Luca et al., 2020) and could accomodate for black holes with masses in the pair-instability supernovae mass gap (45–120 $M_{\odot}$) (Abbott et al., 2020a; De Luca et al., 2021; O'Brien et al., 2021) and in the low mass gap (2.5–5 $M_{\odot}$) (Abbott et al., 2020c,b; Clesse & García-Bellido, 2022). Finally, the recent evidence of a gravitational-wave background reported by the NANOGrav collaboration (Agazie et al., 2023) could directly probe PBH formation from high amplitude peaks of the primordial power spectrum (Clesse & García-Bellido, 2017; Vaskonen & Veermäe, 2021; Franciolini et al., 2023).

A key aspect about PBHs is that they were proposed as cold dark matter candidates (Chapline, 1975). This hypothesis has been investigated in a plethora of studies, providing constraints on the fraction of DM comprised by PBHs (see Carr & Kühnel (2020) for a review). The presence of PBHs would entail a variety of astrophysical phenomena, such as gamma rays emission from evaporating PBHs (Laha, 2019; Coogan et al., 2021), microlensing effects (Niikura et al., 2019; Blaineau et al., 2022) and disruption of wide binaries or ultra-faint dwarfs (Monroy-Rodríguez & Allen, 2014; Brandt, 2016). In addition, accreting PBHs would impact the CMB spectrum and anisotropies (Poulin et al., 2017; Serpico et al., 2020), the 21 cm power spectrum (Mena et al., 2019) and would produce radio and X-ray backgrounds (Cappelluti et al., 2022; Ziparo et al., 2022).

When deriving constraints on the abundance of PBHs, it is commonly assumed that PBHs have the same mass (i.e. a δ-function), although these constraints actually depend on the adopted PBH mass function (Kühnel & Freese, 2017). In particular, PBH formation models in slow-roll inflation predict an approximately lognormal mass function (Dolgov & Silk, 1993; Kannike et al., 2017), while latest simulations of PBH formation across the QCD epoch derived a mass function peaked around $M_{\rm PBH} \sim 1\ {\rm M}_{\odot}$, with a non-trivial shape departing from lognormal (Franciolini et al., 2022).

If PBHs constitute a fraction of dark matter, they would add a poissonian component to the matter power spectrum (Meszaros, 1975; Afshordi et al., 2003; Ali-Haïmoud, 2018), accelerating structure formation and consequently enhancing the abundance of haloes in which stars can form (Kashlinsky, 2016b). This effect on the star formation process is particularly relevant for what concerns the NIRB excess puzzle, since a higher star formation rate density at high-z can then provide the required levels of NIRB fluctuations (Cappelluti et al., 2022). Moreover, PBHs could directly contribute to the NIRB with the radiation emitted by accreting gas from their surroundings.

Hasinger (2020b, hereafter Hasinger 2020b) computed cosmic backgrounds from gas accretion onto PBHs and could recover only 0.3 per thousand of the NIRB with his model. However, Hasinger 2020b considered gas accretion only in the intergalactic medium (IGM), while PBHs could accrete matter also in dense virialized structures, i.e DM haloes. In particular, Ziparo et al. (2022, hereafter Ziparo et al. 2022) have shown that the contribution of PBHs accreting in DM haloes to X-ray and Radio backgrounds is > 60 per cent larger than those accreting in the IGM.

In this paper, following the model by Ziparo et al. 2022, we compute the NIRB produced by PBHs taking into account both PBH accretion in DM haloes and a self-consistent treatment of X-ray ionization and heating of the IGM. We further improve the Ziparo et al. 2022 model both considering the modification of the matter power spectrum induced by the presence of the PBHs, previously neglected, and generalizing the framework to extended mass functions. In Section 6.2 we summarize the basic model and present its extensions. In Section 6.3 we present the main results of this work. Finally, we state our conclusions in Section 6.4.

Throughout the paper we assume a flat Universe with the following cosmological parameters: $\Omega_m = 0.3075$, $\Omega_\Lambda = 1 - \Omega_m$, $\Omega_b = 0.0486$, $H_0 = 67.74$ km s^{-1}Mpc^{-1} , $n_s = 0.965$ and $\sigma_8 = 0.811$ (Planck Collaboration et al., 2016).

6.2 Methods

To investigate the contribution of PBHs to the NIRB we rely on the formalism described in Ziparo et al. 2022. We first revisit their model in order to introduce the framework (Section 6.2.1, 6.2.2). We then compute the intensity and angular power spectrum of the NIRB in Section 6.2.3. In the last two Sections we extend the model to account for the modification of matter power spectrum induced by PBHs (Section 6.2.4) and extended mass functions (Section 6.2.5).

6.2.1 Cosmological distribution of PBHs

Assume that a DM fraction $f_{\rm PBH}$ is made of PBHs of mass $M_{\rm PBH}$. DM distribution on cosmological scales can be described as a diffuse component with density equal to the mean DM density, and virialized regions where matter has collapsed into DM haloes. As PBHs are distributed as the DM, we decompose the number density of PBHs as

$$n_{\rm PBH}(z) = \frac{f_{\rm PBH}\Omega_{\rm DM}\rho_c(1+z)^3}{M_{\rm PBH}} = n^{\rm IGM}_{\rm PBH}(z) + n^{h}_{\rm PBH}(z), \tag{6.1}$$

where $n^{\rm IGM}_{\rm PBH}$ ($n^{h}_{\rm PBH}$) is the number density of PBHs in the intergalactic medium (haloes). The abundance of PBHs in haloes is related to the collapsed fraction of DM in haloes $f_{\rm coll}$, which can be computed as

$$f_{\rm coll}(M_h, z) = {\rm erfc}\left(\frac{\delta_{\rm crit}(z)}{\sigma_M}\right) \tag{6.2}$$

in the Press-Schechter formalism (Press & Schechter, 1974). Here $\delta_{\rm crit}(z) = 1.68/D(z)$ is the critical overdensity for collapse, $D(z)$ is the growth factor and σ_M^2 is the mass variance of the linearly extrapolated matter overdensity field. Thus, the number density of PBHs in the IGM and in haloes are

$$n_{\rm PBH}^{\rm IGM}(z) = (1 - f_{\rm coll}) n_{\rm PBH}(z), \quad n_{\rm PBH}^{h}(z) = f_{\rm coll} n_{\rm PBH}(z). \tag{6.3}$$

PBH distribution inside haloes

The distribution of PBHs inside haloes follows the DM density profile, here assumed to be NFW (Navarro et al., 1997):

$$\rho_{\rm DM}(x) = \frac{\rho_c \delta_c}{cx(1+cx)^2}, \tag{6.4}$$

where $x = r/r_{\rm vir}$ is the radial distance in virial radius units and c is the concentration parameter from Macciò et al. (2007). Following Ziparo et al. 2022, we model its redshift evolution as $c \propto (1+z)^{-1}$. The parameter δ_c is a function of both the concentration parameter and the overdensity at the collapse redshift Δ_c (Barkana & Loeb, 2001):

$$\delta_c = \frac{\Delta_c}{3} \frac{c^3}{\ln(1+c) - c/(1+c)}, \tag{6.5}$$

with $\Delta_c = 18\pi^2 + 82d - 39d^2$, $d = \Omega_m^z - 1$ and $\Omega_m^z = \Omega_m(1+z^3)/(\Omega_m(1+z^3) + \Omega_\Lambda)$. Being PBHs distributed as DM, the number of PBHs within radius r an $r + r$ is

$$N_{\rm PBH}(r) = \frac{f_{\rm PBH}}{M_{\rm PBH}} 4\pi r^2 \rho_{\rm DM}(r) r. \tag{6.6}$$

6.2.2 PBHs accretion

To estimate the accretion rate of gas onto PBHs, we adopt the Bondi–Hoyle–Lyttleton formula (Bondi, 1952; Edgar, 2004):

$$\dot{M} = \lambda 4\pi \frac{G^2 M_{\rm PBH}^2 \rho_b}{(c_s^2 + v_{\rm BH}^2)^{3/2}}, \tag{6.7}$$

where ρ_b and c_s are the density and sound speed of the accreting gas, respectively, $v_{\rm BH}$ is the relative velocity between the PBH and the gas, and λ is the accretion parameter that accounts for non gravitational effects (i.e radiative feedback, gas pressure, outflows). Following Poulin et al. (2017), we adopt the value $\lambda = 0.01$, which is a benchmark for an advection dominated accretion flow (ADAF, Yuan & Narayan, 2014).

Accretion conditions in the IGM and inside haloes differ substantially: in the following we describe the relevant physical quantities, i.e. ρ_b, c_s and $v_{\rm BH}$, separately for the two cases.

Accretion in the IGM

Following Ricotti et al. (2008a), we assume a uniform gas density in the IGM, equal to

$$\rho_{\rm IGM}(z) = 250\, \mu m_p \left(\frac{1+z}{1000}\right)^3 \text{g cm}^{-3}, \tag{6.8}$$

where $\mu = 1.22$ is the mean molecular weight for a gas of primordial composition and m_p is the proton mass. The sound speed of the gas is given by:

$$c_s = \sqrt{\frac{k_B T_{\rm IGM}}{\mu m_p}}, \tag{6.9}$$

where k_B is the Boltzmann constant and $T_{\rm IGM}$ is the IGM temperature. The relative velocity between baryons and PBHs is gaussianly distributed on linear scales, hence its modulus follows a maxwellian distribution, with variance given by (Ali-Haïmoud & Kamionkowski, 2017)

$$\sigma^2_{\rm rel}(z) \equiv \langle v^2_{\rm BH} \rangle = 30\ min\Big[1, (1+z)/1000\Big] \text{km s}^{-1}. \tag{6.10}$$

To properly account for the distribution of relative velocities, it is useful to define an effective velocity $v_{\rm eff}$ (Ricotti et al., 2008a), whose analytical expression is (Mena et al., 2019)

$$v_{\rm eff} = \sigma_{\rm rel}(z)\Big[\Big(\frac{3}{2}\Big)^{3/2} U\Big(\frac{3}{2}, 1, \frac{3}{2}\Big(\frac{\sigma_{\rm rel}}{c_s}\Big)^{-2}\Big)\Big]^{-1/3}, \tag{6.11}$$

where $U(a,b,z)$ is the confluent hypergeometric function of second kind. The accretion rate of PBHs in the IGM is finally obtained by substituting the relevant quantities computed above in equation (6.7).

Accretion within haloes

To model the internal structure of haloes, we assume that the gas is in thermal equilibrium at the virial temperature $T_{\rm vir}$. Moreover, we impose hydrostatic equilibrium between DM and gas. Given these assumptions, the density profile of gas is described by the following equation (Makino et al., 1998):

$$\rho_b(r) = \rho_{b,0} \exp\Big[-\frac{\mu m_p}{2k_B T_{\rm vir}}\Big(V^2_{\rm esc}(0) - V^2_{\rm esc}(r)\Big)\Big], \tag{6.12}$$

where $V_{\rm esc}$ is the escape velocity, given by:

$$V^2_{\rm esc}(r) = 2\int_r^{r_{\rm vir}} r' \frac{GM(r')}{r'^2}, \tag{6.13}$$

and $\rho_{b,0}$ is a normalization constant set by imposing:

$$4\pi \int_0^{r_{\rm vir}} r r^2 \rho_b(r) = \frac{\Omega_b}{\Omega_{\rm DM}} M_h, \tag{6.14}$$

where M_h is the halo mass, Ω_b and $\Omega_{\rm DM}$ are the total baryon and DM densities in units of the critical density. The sound speed in haloes can be computed via equation (6.9), substituting $T_{\rm IGM}$ with $T_{\rm vir}$. As a consequence of hydrostatic equilibrium assumption, we set $v_{\rm BH} = 0$.

6.2.3 NIRB

To compute the specific luminosity of PBHs we follow Ziparo et al. 2022. Given the accretion rate $\dot{M}$, the bolometric luminosity of a single PBH is $L = \varepsilon \dot{M} c^2$, where $\varepsilon = 0.1$ is the radiative efficiency. We assume that, as for astrophysical black holes, the spectrum of PBHs can be described by a double power-law with an exponential cut-off (Hasinger, 2020b):

$$L_\nu \propto \begin{cases} \Big(\frac{\nu}{\nu_c}\Big)^{\alpha_{\rm sync}} & \nu \leq \nu_c \\ \Big(\frac{\nu}{\nu_c}\Big)^{\alpha} & \nu > \nu_c \end{cases} \tag{6.15}$$

where the cut-off frequency is $\nu_{\rm cut} = 200$ keV and $\alpha = -0.7$. Below the critical frequency $\nu_c = \lambda_c/c$, with $\lambda_c = 0.45(M_{\rm PBH}/\text{M}_\odot)^{0.4}$, synchrotron emission dominates and the power law

index is $\alpha_{\rm sync} = 1.86$ (Hasinger, 2020b). The above spectral shape is consistent with an ADAF accretion model with accretion rates $\dot{m} = \dot{M}/\dot{M}_{\rm EDD} \gtrsim 10^{-2}$, which holds for those PBHs producing the bulk of the background radiation in our model. We fix the normalization of the spectrum by setting the bolometric correction in the 2–10 keV band to $f_X = 0.1$ (Hasinger, 2020b).

Given the specific luminosity, L_ν, the specific emissivity of a population of PBHs accreting in the IGM is

$$\dot{\rho}_{\rm IGM}(\nu, z) = n_{\rm PBH}^{\rm IGM}(z) L_\nu(z). \tag{6.16}$$

The specific luminosity of an entire halo can be computed by:

$$L_\nu^h(z) = \int_0^{R_{\rm vir}} r N_{\rm PBH} r L_\nu(r, z). \tag{6.17}$$

The specific emissivity of a population of PBHs accreting inside haloes is then given by integrating over the halo mass function (Murray et al., 2013):

$$\dot{\rho}_h(\nu, z) = \int_{M_{\rm min}}^{M_{\rm max}} M L_\nu^h(M) n M, \tag{6.18}$$

where $M_{\rm max} = M_h(T_{\rm vir} = 10^4)$ is the minimum mass of haloes inside which stars can form and $M_{\rm min}$ is the minimum mass of haloes required to form a baryon overdensity (Barkana & Loeb, 2001):

$$M_{\rm min}(T_{\rm IGM}, z) = 1.3 \times 10^3 \, {\rm M}_\odot \left(\frac{10}{1+{\rm z}}\right)^{3/2} \left(\frac{{\rm T_{IGM}}}{1\ {\rm K}}\right)^{3/2}. \tag{6.19}$$

Inside haloes with $M_h < M_{\rm min}$, the gas density is close to the mean IGM one and therefore we consider their contribution in the IGM emissivity.

The background intensity in a given band [ν_1,ν_2] is related to the specific emissivity by (Fernandez et al., 2010; Yue et al., 2013):

$$I^{[\nu_1,\nu_2]} = \frac{c}{4\pi} \int z \frac{\int_{\nu_1}^{\nu_2} \nu \varepsilon_{\nu'}(z)}{H(z)(1+z)}, \tag{6.20}$$

where $\nu' = (1+z)\nu$ and $H(z)$ is the Hubble parameter as a function of redshift. The angular power spectrum of NIRB fluctuations from PBHs can be decomposed in a two-halo and a shot-noise term:

$$C_l = C_l^{\text{2-halo}} + C_l^{\rm SN}. \tag{6.21}$$

The clustering component at frequency ν and for the multiple moment l is given by (Cooray et al., 2004; Fernandez et al., 2010)

$$C_l^{\text{2-halo}} = \frac{c}{4\pi} \int z \frac{\epsilon_{\nu'}^2(z)}{H(z) r^2(z) (1+z)^2} P\left(k = \frac{l}{r(z)}, z\right), \tag{6.22}$$

where $r(z)$ is the comoving distance and $P(k, z)$ is the power spectrum of the underlying matter distribution. PBHs in the IGM correspond to DM in the linear regime and therefore $P_{\rm IGM}(k, z) = P_{\rm lin}(k, z)$, where the right hand side is the linear matter power spectrum. Instead, haloes are biased tracers of the linear matter density field and their power spectrum can be written as $P^h(k, z) = b_{\rm eff}(z) P(k, z)$, where the effective bias $b_{\rm eff}$ is given by:

$$b_{\rm eff}(z) = \int_{M_{\rm min}}^{M_{\rm max}} M b_h(M, z) n M / \int_{M_{\rm min}}^{M_{\rm max}} M n M, \tag{6.23}$$

where $b_h(M,z)$ is the halo bias, as derived in Tinker et al. (2010).

The shot noise angular power spectrum is described by the following equation (Cooray et al., 2012a; Yue et al., 2013):

$$C_l^{\rm SN} = \frac{c}{(4\pi)^2}\int \frac{z}{H(z)r^2(z)(1+z)^2}\int_{M_{\rm min}}^{M_{\rm max}} ML_\nu^2(M)nM. \tag{6.24}$$

We note that in principle one should consider the one-halo term, given by (Cooray et al., 2012a):

$$C_l^{\text{1-halo}} = \frac{c}{(4\pi)^2}\int \frac{z}{H(z)r^2(z)(1+z)^2} \tag{6.25}$$

$$\int_{M_{\rm min}}^{M_{\rm max}} ML_\nu^2(M)nM\tilde{u}(k=l/r(z),M)^2, \tag{6.26}$$

where $\tilde{u}(k=l/r(z),M)$ is the Fourier transform of the NFW profile. For the redshift and halo mass range of interest, we checked that $\tilde{u}(k=l/r(z),M)\sim 1$ and therefore the one-halo term reduces to the shot noise term in equation (6.24).

6.2.4 Matter Power spectrum modified by PBHs

PBHs may constitute a fraction of DM, thus they would add a Poisson shot noise term to the linear matter power spectrum (Meszaros, 1975; Afshordi et al., 2003):

$$P_{\rm poiss} = \frac{f_{\rm PBH}^2}{n_{\rm PBH,0}}, \tag{6.27}$$

where $n_{\rm PBH,0}$ is the PBH number density at redshift $z=0$. The total matter power spectrum can be then written as (Villanueva-Domingo & Ichiki, 2021):

$$P_{\rm PBH-\Lambda CDM}(z,k) = P_{\Lambda\rm CDM}(k,z) + D^2(z)T_{\rm iso}^2(k)P_{\rm poiss}, \tag{6.28}$$

where $D(z)$ is the linear growth factor and $T_{\rm iso}$ is the isocurvature transfer function. An approximate expression for $T_{\rm iso}$ is given by (Peacock, 1998):

$$T_{\rm iso} = \begin{cases} \frac{3}{2}(1+z_{\rm eq}), & k \geq k_{\rm eq} \\ 0, & k < k_{\rm eq} \end{cases} \tag{6.29}$$

where $z_{\rm eq}$ is the redshift of radiation-matter equality and $k_{\rm eq} = c^{-1}H(z_{\rm eq})/(1+z_{\rm eq})$. The contribution to the power spectrum from PBHs can be recast in the form (Villanueva-Domingo & Ichiki, 2021):

$$P_{\rm PBH} = T_{\rm iso}^2 P_{\rm poiss} = 2.5\times 10^{-2}\, f_{\rm PBH}\left(\frac{M_{\rm PBH}}{30\ {\rm M}_\odot}\right)\ {\rm Mpc}^3. \tag{6.30}$$

The PBH modification to the power spectrum affects the variance of the matter overdensity field and thus the halo mass function.

Hereafter we will refer to a PBH-ΛCDM cosmology whenever adopting the power spectrum described by equations (6.28)–(6.30). In particular we consider a PBH-ΛCDM cosmology in our models and (see Sec. 6.3). In Fig. 6.1 we show the Press–Schechter halo mass function at $z=20$ in the standard ΛCDM scenario and including the modification induced by PBHs, for different values of the parameter $f_{\rm PBH}M_{\rm PBH}$. At $z=20$, when including the extra power on small scales due to PBHs, the halo mass function is a factor of 3 (40) higher for $M_h = 10^5\ {\rm M}_\odot$

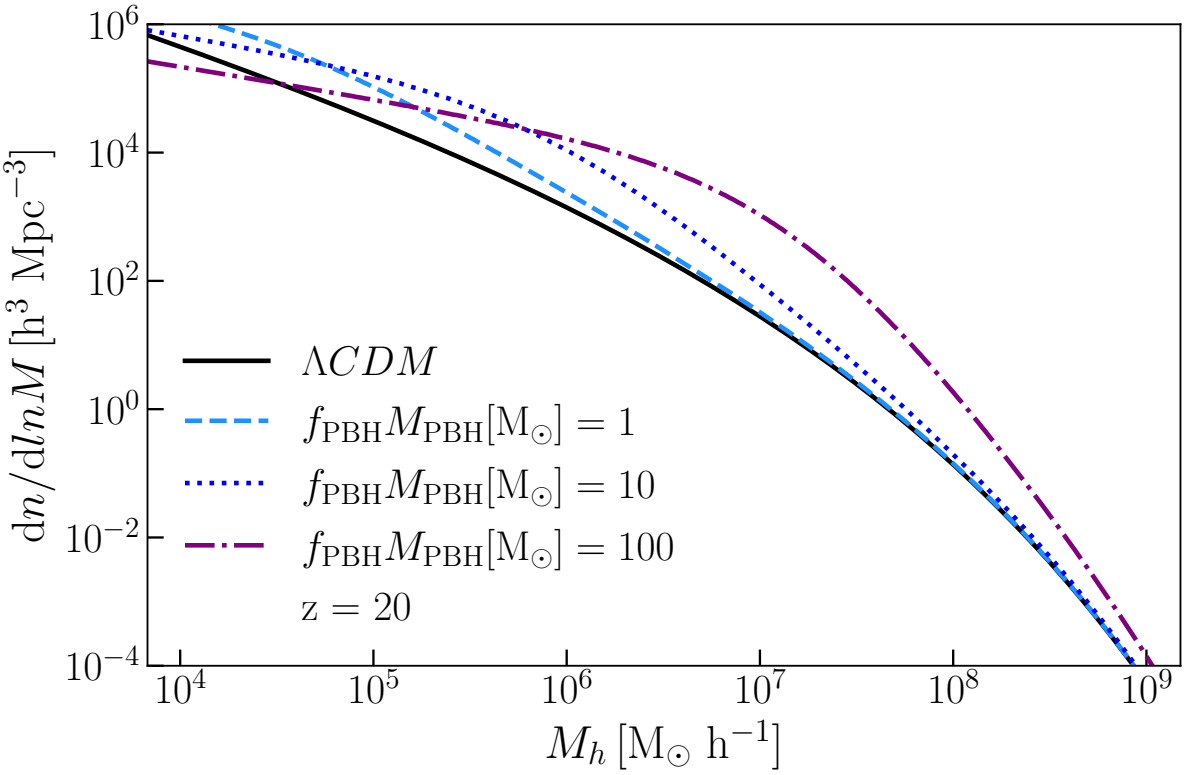

Figure 6.1: Press–Schechter halo mass function at $z = 20$, in the standard ΛCDM scenario (black solid line) and including the modification induced by PBHs, with $f_{\rm PBH}M_{\rm PBH} = 1\ {\rm M}_\odot$ (light blue dashed), $f_{\rm PBH}M_{\rm PBH} = 10\ {\rm M}_\odot$ (blue dotted) and $f_{\rm PBH}M_{PBH} = 100\ {\rm M}_\odot$ (purple dot-dashed).

($M_h = 10^7\ {\rm M}_\odot$) with respect to the standard ΛCDM case, considering $f_{\rm PBH}M_{\rm PBH} = 100$. In Fig. 6.2 we compare the bolometric emissivity, from both haloes and IGM, in the ΛCDM and PBH-ΛCDM cosmologies, as a function of redshift. As a consequence of the increased number of small haloes expected in the PBH-ΛCDM, the contribution to the total emissivity from accreting PBHs in DM haloes is enhanced by a factor of 2 (20) at redshift $z = 30$ (40). Moreover, also the collapsed DM fraction is higher and thus the relative contribution from PBHs accreting in the IGM is further lowered. The emissivity of PBHs accreting in haloes at redshift $z = 20$ (40) is roughly 10 (100) times the emissivity from PBHs in the IGM. We point out that, as a consequence of the aforementioned effects, in the PBH-ΛCDM cosmology halo emissivity dominates the IGM one at any redshift, unlike in the standard ΛCDM case.

6.2.5 Extended PBH mass function

The mass function of PBHs at the epoch of their formation is denoted by $\psi(M_{\rm PBH})$, and defined as:

$$\psi(M_{\rm PBH}) = \frac{1}{f_{\rm PBH}} f_{\rm PBH} M_{\rm PBH}. \tag{6.31}$$

In the following, we generalize our formalism to extended mass functions. In particular, we consider the case of a lognormal mass function[1]:

$$\psi_{\log}(M) = \frac{1}{M\sqrt{2\pi}\sigma} \exp\Big(-\frac{\log(M/M_c)^2}{2\sigma^2}\Big). \tag{6.32}$$

[1]We choose a lognormal mass function to avoid fruitless complications. The main results of our work are unaffected by the exact shape of the mass function.

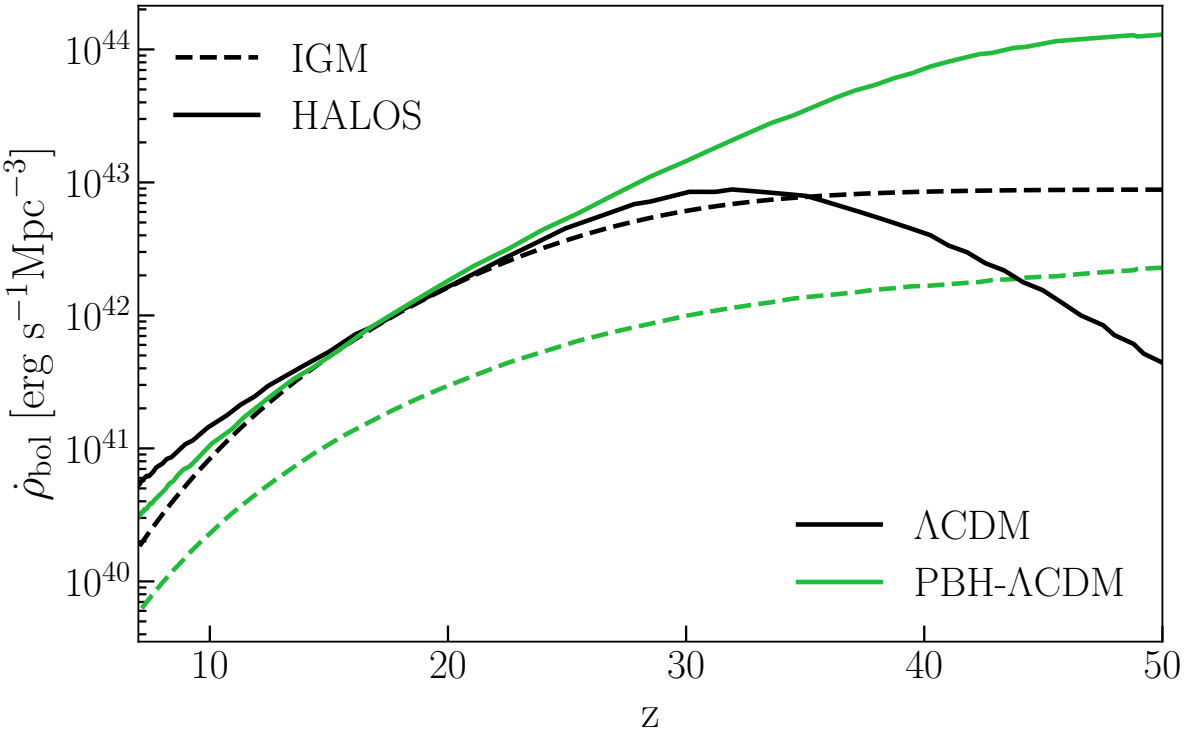

Figure 6.2: Bolometric emissivity from IGM (dashed lines) and haloes (solid lines), in the standard ΛCDM scenario (black) and including the power spectrum modified by PBHs (green). In the case of PBH-ΛCDM cosmology, the halo signal dominates over the IGM one for all the redshift of interest. Here we adopt $M_{\rm PBH} = 30\ {\rm M}_\odot$.

Here M_c is the critical mass that sets the position of the peak and σ is the standard deviation of the distribution. Regarding PBHs in the IGM, their emissivity can be generalized to

$$\dot{\rho}_{\rm IGM}(\nu, z) = \int M n_{\rm PBH}^{\rm IGM}(z, M)\psi(M)L_\nu(z, M), \tag{6.33}$$

where the integral is performed over the PBH mass and $n_{\rm PBH}^{\rm IGM}(z, M)$ is taken from equation (6.3). Recalling that $n_{\rm PBH}^{\rm IGM} \propto M^{-1}$ and $L_\nu \propto M^2$, we can write

$$\dot{\rho}_{\rm IGM} \propto \int M\psi(M)M \equiv \bar{M}. \tag{6.34}$$

Therefore, when computing the emissivity of PBHs in the IGM, an extended mass function is equivalent to a δ-function centered at the mean mass $\bar{M}$ of the mass function[2]. For a lognormal mass function, the mean mass is $\bar{M}_{\rm log} = M_c \exp(\sigma^2/2)$. We will assume the benchmark value $\sigma = 1$ throughout the rest of the paper and quote only the mean mass of the lognormal distribution.

Regarding PBHs accreting in haloes, we must specify how PBHs of different masses are distributed inside the halo. We note that the frictional acceleration exerted onto a body of mass M moving through a homogeneous distribution of particles of mass m ($m \ll M$) with isotropic velocity distribution is $\propto M$ (Binney & Tremaine, 2008). Hence, PBHs with higher masses sink towards the centre of the halo before lighter ones. With this in mind and for simplicity, we then assume that more massive PBHs lie at smaller radii.

[2]This is valid for a constant radiation efficiency. If $\varepsilon \propto \dot{M}^a \propto M^{2a}$, then $L_\nu \propto M^{2+2a}$ and so the corresponding mean mass should be $\bar{M} = \left(\int M\psi(M)M^{2a+1}\right)^{1/(2a+1)}$.

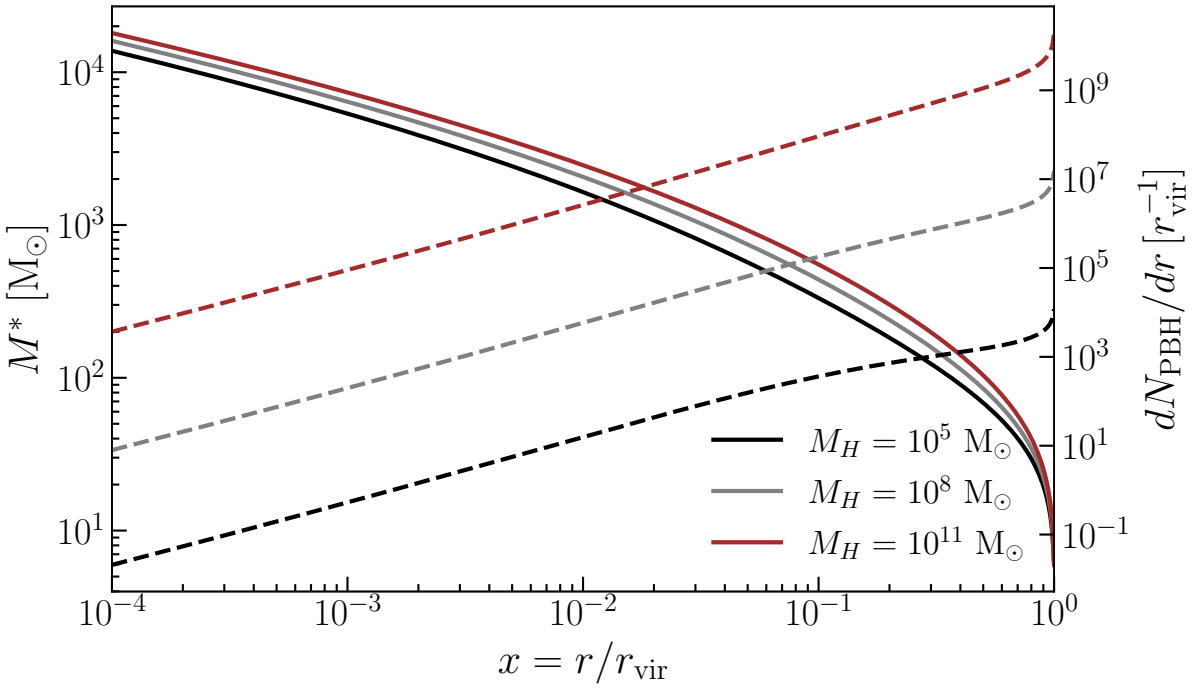

Figure 6.3: Mass of PBHs present at radius r in haloes of masses $10^5\,\mathrm{M}_\odot$ (black), $10^8\,\mathrm{M}_\odot$ (grey), $10^{11}\,\mathrm{M}_\odot$ (brown), when considering a lognormal mass function with $\bar{M}_{\rm log} = 30\ \mathrm{M}_\odot$. The dashed lines show the number of PBHs per unit length, in units of $r_{\rm vir}^{-1}$.

The mass $M^*(r)$ of PBHs at a given radius r can be derived by imposing that the mass $M(r)$ enclosed in a sphere of radius r is equal to the integrated mass of all PBHs more massive than $M^*(r)$:

$$M(r) = 4\pi \int_0^r r' r'^2 \rho_{\rm NFW}(r') = \int_{M^*(r)}^{\infty} M' M' \psi(M'). \tag{6.35}$$

For a lognormal mass function, the right-hand side of the above equation can be computed analitically, giving

$$\log[M^*(r)/M_c] = \sigma^2 + \sqrt{2}\sigma^{-1}\Big[1 - \frac{2M(r)}{M_h}\Big], \tag{6.36}$$

where M_h is the halo mass. We show the resulting $M^*(r)$ for a lognormal mass function with $\bar{M}_{\rm log} = 30\ \mathrm{M}_\odot$ in Fig. 6.3. Once specified $M^*(r)$, the number of PBHs per unit length at radius r is given by

$$N_{PBH} r = 4\pi \frac{f_{PBH}}{M^*(r)} \rho_{DM}(r). \tag{6.37}$$

We can then substitute equation (6.37) into equation (6.17) and apply the same formalism described in Sec. 6.2.3. In Fig. 6.4 we compare the bolometric luminosity of haloes in the case of a delta mass function with $M_{\rm PBH} = 30\ \mathrm{M}_\odot$ and of a lognormal mass function with $\bar{M}_{\rm log} = 30\ M_\odot$. Including the lognormal mass function boosts the halo luminosity by a factor of ~ 10, because more massive PBHs accrete at smaller distances from the center, where the gas density is higher.

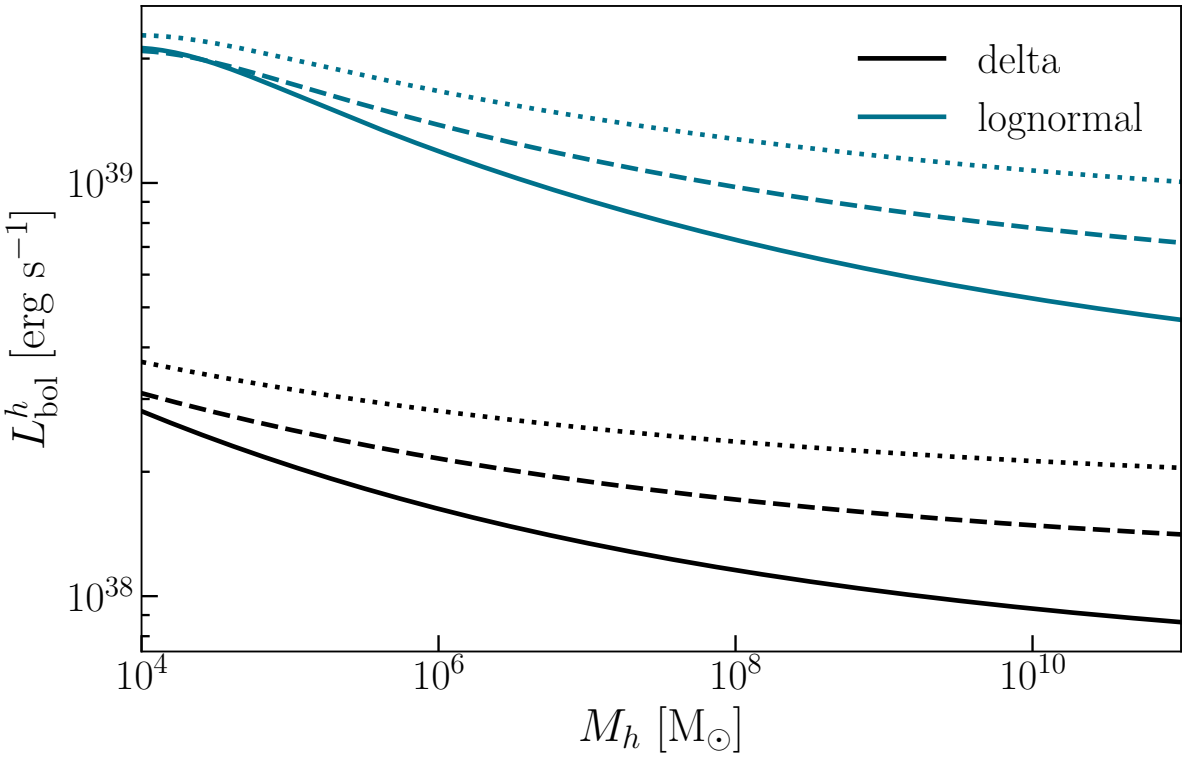

Figure 6.4: Bolometric luminosity of haloes as a function of the halo mass, in the case of a delta (black) and lognormal (blue) mass function, for $z = 20, 30, 40$ (solid, dashed, dotted respectively). The PBH mass for the delta mass function and the mean mass of the lognormal distribution are both set to $M_{\rm PBH} = \bar{M}_{\rm log} = 30\ M_\odot$. With an extended mass function, the luminosity is boosted by a factor ~ 10, because more massive PBH tend to sink towars the center where the gas density is higher.

6.3 Results

In this section we present the IGM temperature evolution, the mean NIRB intensity and the NIRB angular power spectrum obtained from three different models: (*i*) standard ΛCDM cosmology with a PBH delta mass function (ΛCDM-δ); (*ii*) PBH-ΛCDM cosmology with PBH delta mass function (PBH-δ) and (*iii*) PBH-ΛCDM cosmology with a PBH lognormal mass function (PBH-lognormal). We compare our predictions to observational data to test the hypothesis of accreting PBHs as sources of the NIRB.

6.3.1 IGM temperature and ionization evolution

X-ray emission from PBHs would heat and ionize the IGM well before galaxies start to reionize the Universe. To account for this effect, we self-consistently derive the IGM temperature and ionization evolution following the formalism described in Sec. 3 of Ziparo et al. 2022.

In the pre-overlap phase of the cosmic reionization process, the Universe can be split in ionized and neutral regions. In the ionized regions, the redshift evolution of the free electron fraction $x_e(z)$ is solved through equation (33a) in Ziparo et al. 2022, adopting the photoionization rate derived from the UV background in Puchwein et al. (2019). The free electron fraction traces the evolution of the volume filling factor of ionised regions, namely the fraction of volume occupied by ionized regions. In the same regions, we assume an IGM temperature $T_{\rm IGM,ion} = 10^4$ K. Such high temperature suppresses accretion onto PBHs due to high sound speeds (equation (6.9)).

In neutral regions, whose volume filling factor is $1 - x_e(z)$, the free electron fraction $x_{e,n}(z)$

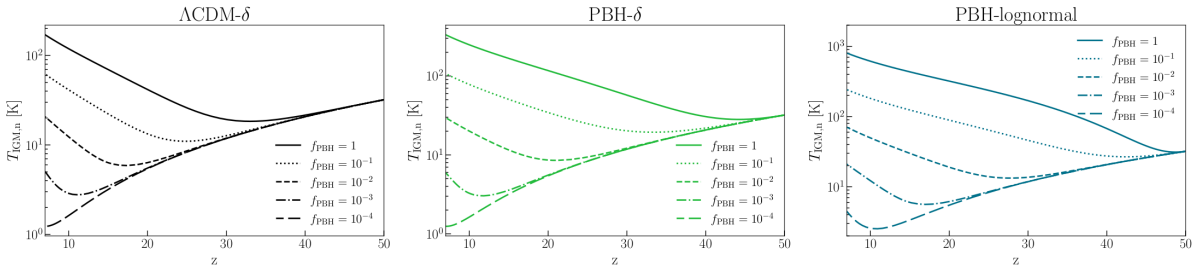

Figure 6.5: Evolution of the neutral IGM temperature as a function of redshift in the three different models , and (black, green and blue respectively). Each line corresponds to different values of $f_{\rm PBH}$: $10^{-4}, 10^{-3}, 10^{-2}, 10^{-1}, 1$ (long-dashed, dot-dashed, dashed, dotted and solid respectively). The PBHs mass is $M_{\rm PBH} = \bar{M}_{\rm log} = 30\ {\rm M}_\odot$. We maintain the same color-coding for the models throughout the rest of the paper.

evolves with redshift according to equation (35a) in Ziparo et al. 2022. Here, the photoionization rate calculation accounts for secondary ionizations due to X-rays emitted by PBHs:

$$\Gamma_{\rm PBH} = \int_{\nu_{\rm min}}^{\infty} \nu \frac{4\pi I_\nu}{h\nu} \left(\frac{h\nu}{E^{\rm th}} - 1 \right) f_{\rm ion} \sigma_H(\nu), \tag{6.38}$$

where $h\nu_{\rm min} = 0.5$ keV [3], $E^{\rm th}$ is the hydrogen ionization threshold, σ_H is the hydrogen ionization cross section and $f_{\rm ion} \sim 0.3$ is the fraction of the primary electron's energy going into secondary ionizations (Furlanetto & Stoever, 2010). In neutral regions we also solve the redshift evolution of temperature $T_{\rm IGM,n}(z)$ through equation (35b) in Ziparo et al. 2022, which takes into account the IGM heating due to the energy injected by X-rays (Mesinger et al., 2013), here assumed to be emitted by PBHs. The heating rate $\epsilon_{\rm PBH}$ per baryon can then be computed as:

$$\epsilon_{\rm PBH} = \int_{\nu_{\rm min}}^{\infty} \nu \frac{4\pi I_\nu}{h\nu} (h\nu - E^{\rm th}) f_{\rm heat} \sigma_H(\nu), \tag{6.39}$$

where $f_{\rm heat} \sim 0.3$ is the fraction of the primary electron's energy going into heat (Valdés et al., 2010).

Following the evolution of neutral regions $T_{\rm IGM,n}$ is crucial because changes in the IGM temperature affects PBHs emissivity. On the one hand, if the IGM temperature increases, the effective velocity of PBHs accreting in the IGM increases as well (equation (6.11)): this lowers their luminosity and consequently their emissivity. On the other hand, to higher $T_{\rm IGM,n}$ correspond higher $M_{\rm min}$ (equation (6.19)): the integration interval in equation (6.18) is thus shortened, which reduces the emissivity of PBHs accreting in haloes. Therefore, if $T_{\rm IGM,n}$ increases (decreases), the total emissivity of PBHs is lowered (enhanced).

We show the resulting temperature evolution in Fig. 6.5 for the three different models, adopting $M_{\rm PBH} = \bar{M}_{\rm log} = 30\ {\rm M}_\odot$ and $f_{\rm PBH} = 10^{-4}, 10^{-3}, 10^{-2}, 10^{-1}, 1$. For $f_{\rm PBH} = 1$, heating from PBHs increases the IGM temperature in neutral regions at $z \sim 6$ by a factor of $\sim 10, 20, 60$ in model ΛCDM-δ, PBH-δ, PBH-lognormal respectively, with respect to a ΛCDM cosmology which does not include PBHs. While in model ΛCDM-δ $T_{\rm IGM,n}$ starts increasing around $z \sim 30$, in model PBH-δ it rises at higher redshifts ($z \sim 40$), as the PBH emissivity is boosted by the higher number of small mass ($M_h \lesssim 10^6$–$10^7\ {\rm M}_\odot$) haloes. For $f_{\rm PBH} \lesssim 10^{-2}$, the effect of PBHs on the halo mass function is negligible and the evolution of $T_{\rm IGM,n}$ in the two cases is almost identical. In model PBH-lognormal, the luminosity of haloes is further enhanced by the lognormal mass function (Fig. 6.4) and $T_{\rm IGM,n}$ reaches ~ 900K at $z \sim 6$.

[3] We neglect the contribution of UV photons to IGM heating and ionization since, as discussed in Ziparo et al. 2022, Appendix B, the Stromgren sphere surrounding accreting PBHs results to be comparable to the Bondi radius, preventing UV photons to contribute to the IGM ionization.

Before moving to the core results of this work, we briefly comment on the implications of IGM heating from PBHs. Firstly, our model does not affect the IGM temperature at $z \lesssim 5$, where measurements from Lyman-alpha forest observations are obtained (Walther et al., 2019; Gaikwad et al., 2020). Below $z \sim 6$, most of the Universe is ionized and IGM temperatures $T_{\rm IGM,ion} \gtrsim 10^4$ suppress the emission and thus the heating from PBHs in ionized regions. Moreover, the contribution from PBHs in neutral regions is also suppressed because their volume filling factor, i.e $1 - x_e$ in our model, approaches zero as cosmic reionization proceeds. Instead, at $z \gtrsim 10$, the Universe is mostly neutral and the volume filling factor of neutral regions is basically unity. Radiation from PBHs is then effective in heating the IGM above the adiabatic cooling temperature. Therefore, forthcoming 21 cm observations could provide stringent constraints on the heating from PBHs and hence on their abundance (Mena et al., 2019).

6.3.2 NIRB mean intensity and angular power spectrum

As already mentioned in the Introduction, direct measurements of the mean NIRB intensity are uncertain (Kashlinsky et al., 2018). However, constraints on the mean NIRB excess from unknown sources can be derived from the angular power spectrum measurement, as done by Kashlinsky et al. (2007), who found $I^{2-5} \gtrsim 1$ nW m^{-2}sr^{-1} in the 2–5 band.

NIRB mean intensity

We compute the mean NIRB intensity in the 2–5 band, using equation (6.20). To test our predictions, in Fig. 6.6 we compare these results with data from Kashlinsky et al. (2007). We consider the limiting case $f_{\rm PBH} = 1$, which sets the upper limit for NIR flux produced by PBHs, for a mass range $1\ {\rm M}_\odot \leq {\rm M}_{\rm PBH} = \bar{\rm M}_{\rm log} \leq 10^3\ {\rm M}_\odot$. Our choice is driven, one the one hand, by the requirement of substantial accretion rates and hence luminosities and, on the other hand, by existing constraints on the abundance of higher mass PBHs. We show the results for the three different models in Fig. 6.6. We find that in the ΛCDM-δ (PBH-δ, PBH-lognormal) model, PBHs contribution to the NIRB mean intensity is at most 1.4 (0.9,1.5) per cent, if $M_{\rm PBH} = 10^3\ {\rm M}_\odot$.

However, current constraints on the abundance of PBHs (Carr & Kühnel, 2020) already exclude $f_{\rm PBH} = 1$ in the mass range considered here. Lower values of $f_{\rm PBH}$ result in lower NIR flux produced by PBHs. In Fig. 6.7 we show, as a function of PBH mass, the ratio between the intensity of the NIRB produced by PBHs computed considering the maximum value of $f_{\rm PBH}$ allowed by existing constraints and the NIRB mean intensity reference value. We also show the most stringent upper limit on $f_{\rm PBH}$, which in the mass range of interest are derived from LIGO observations of black holes mergers (Abbott et al., 2017; Kavanagh et al., 2018) and from CMB angular power spectrum (Poulin et al., 2017).

We find that, in the most favorable case consistent with constraints, PBHs can produce 0.1 per cent of the NIRB intensity if $M_{\rm PBH} \sim 50\ {\rm M}_\odot$. We show the results only for the and models, as we consider constraints computed adopting a delta mass function. We note that the difference between the two models is very tiny, as for low values of $f_{\rm PBH}$ the modification induced by PBHs to the matter power spectrum is almost negligible.

NIRB angular power spectrum

We also compute the angular power spectrum of NIRB fluctuations produced by PBHs at the reference wavelength 3.6 , using equations. (6.22) and (6.24). We show the results in Fig. 6.8, for the case $f_{\rm PBH} = 1$ and with PBH masses between $1\ {\rm M}_\odot$ (lower lines) and $10^3\ {\rm M}_\odot$ (upper lines).

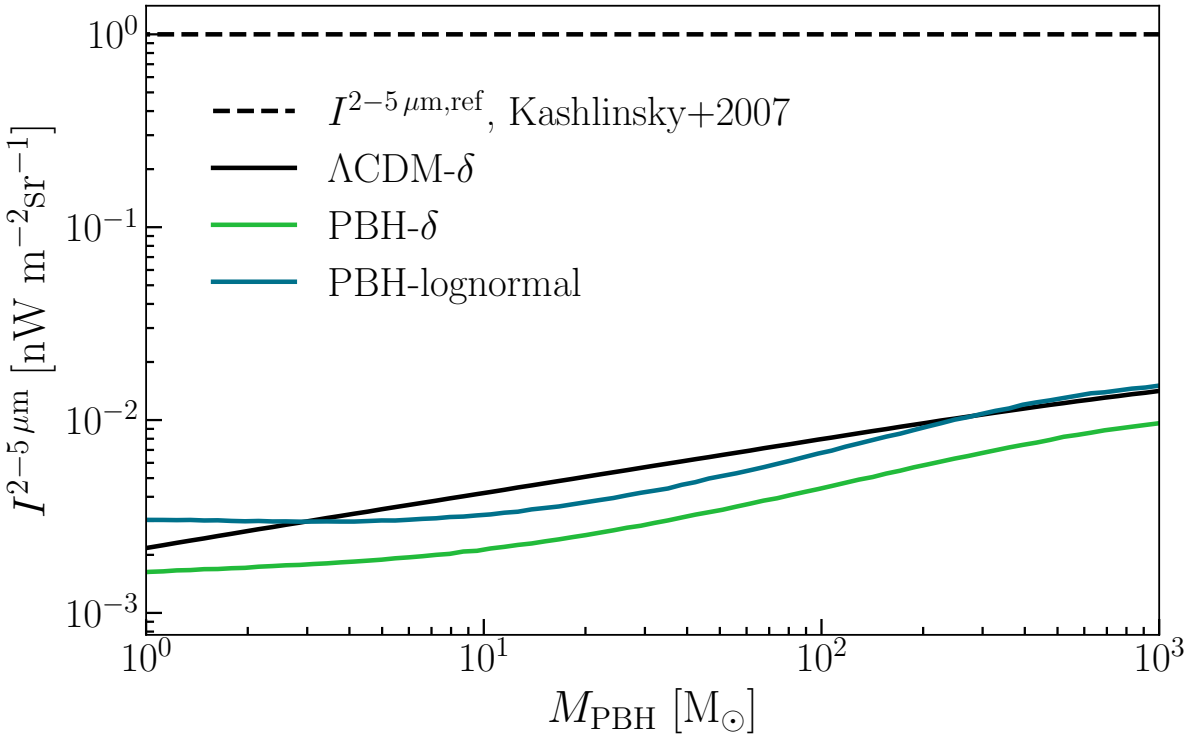

Figure 6.6: Near infrared background intensity in the band 2-5 predicted by the three different models, as a function of PBH mass. The horizontal dashed line corresponds to the minimal near-infrared flux required by NIRB fluctuations (Kashlinsky et al., 2007).

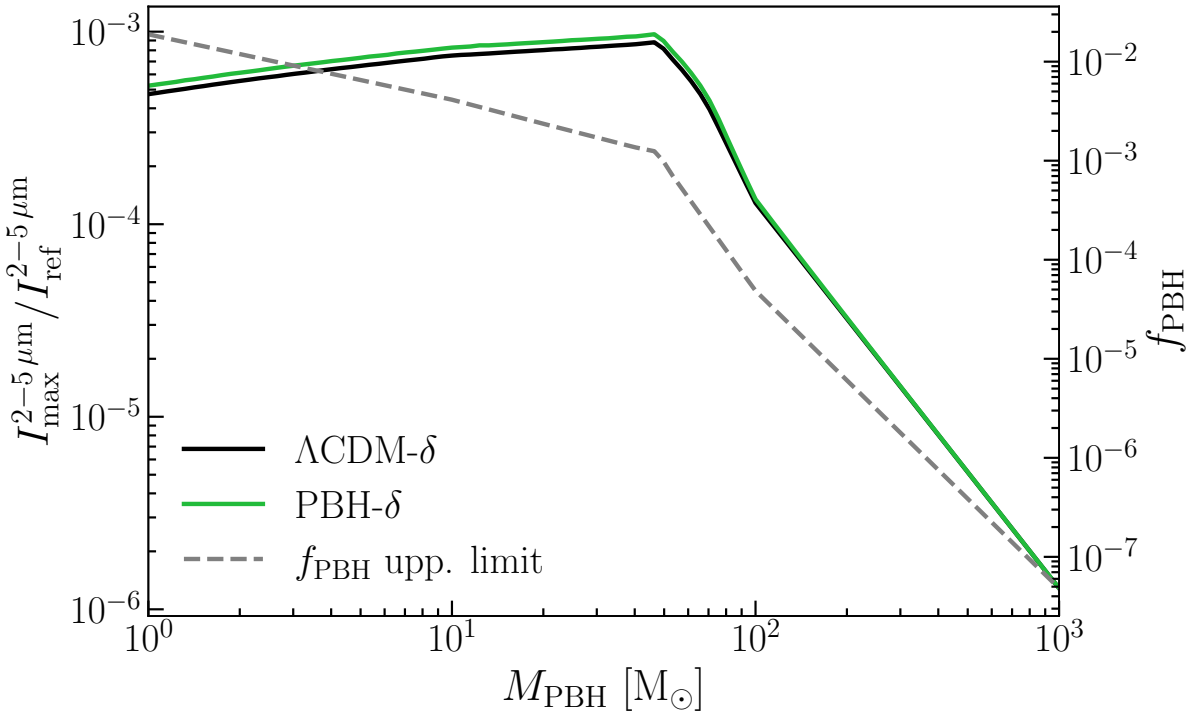

Figure 6.7: Maximum intensity of the NIRB produced by PBHs accounting for present constraints, in units of the reference value (1 nW m^{-2}sr^{-1}), for model ΛCDM-δ (solid black) and (solid green). We do not show the model, because available upper limits on f_{PBH} are derived only for a δ-mass function. We also plot the strongest constraint on f_{PBH} (dashed grey) as a function of the PBH mass. We use the LIGO and CMB bounds from PBHBounds (Kavanagh, 2019).

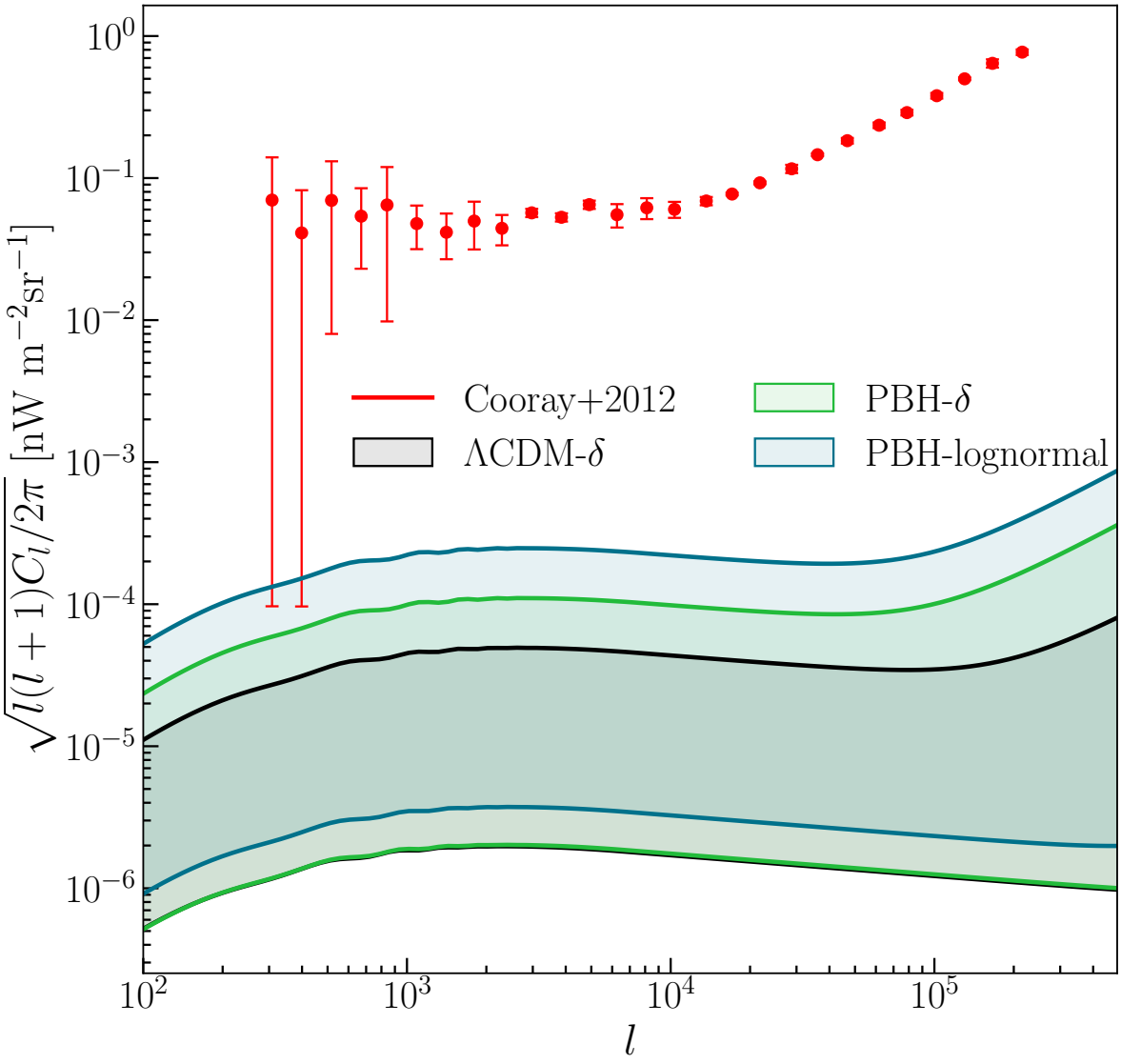

Figure 6.8: Angular power spectrum of the NIRB at 3.6 μm from PBHs for the three models, compared with observational data from Cooray et al. (2012a). Shaded regions correspond to values of PBH mass between 1 $M_\odot$ (lower lines) and 10^3 $M_\odot$ (upper lines).

We compare our predictions with the latest measurements of NIRB angular power spectrum from Spitzer Deep, Wide-Field Survey (Cooray et al., 2012a).

None of the models considered in this work is able to reproduce the observed angular power spectrum. At multiple moment $l \sim 10^3$, corresponding to angular scales of $\theta = 2\pi/l \sim 20$ arcmin, fluctuations predicted by the (,) model are lower than the measured one by a factor of 1000 $(400, 200)$. This holds for $M_{\rm PBH} = 10^3$ $M_\odot$, which provides the highest value of the angular power spectrum in the mass range considered here.

6.4 Summary and Discussion

In this work, we have tested the hypothesis that PBHs are sources of the NIRB excess. By assuming that PBHs constitute a fraction $f_{\rm PBH}$ of cold dark matter (DM), we have computed the mean intensity and angular power spectrum of the NIRB arising from their accretion.

Following the formalism by Ziparo et al. (2022), we account for PBH accretion both in the intergalactic medium (IGM) and in DM haloes, and we self-consistently derive the IGM temperature evolution, considering ionization and heating due to X-ray emission from PBHs. The Ziparo et al. 2022 model is based on the ΛCDM linear matter power spectrum, and considers a δ function for the PBH mass distribution.

Besides this ΛCDM-δ model, we have considered the possibility that PBHs modify the matter power spectrum (PBH-δ model), and follow an extended lognormal mass function (PBH-lognormal model). In both and models we adopt a PBH-ΛCDM cosmology, accounting for the matter power spectrum modified by PBHs.

For each model, we have derived the intensity and angular power spectrum of the NIRB finding that PBHs contribute to the observed NIRB fluctuations to < 1 per cent, even in the most optimistic cases considered in this work. This conclusion is supported by these intermediate results:

- The PBH modification to the power spectrum affects the variance of the matter overdensity field and thus the halo mass function, adding an extra power on small scales. In particular, at $z = 20$, in the PBH-ΛCDM model, the halo mass function is a factor of 3 (40) higher for $M_h = 10^5$ M$_\odot$ ($M_h = 10^7$ M$_\odot$) with respect to the standard ΛCDM case, considering $f_{\rm PBH} M_{\rm PBH} = 100$.

- As a consequence of the increased number of small haloes expected in the PBH-ΛCDM, the contribution to the total emissivity from accreting PBHs in DM haloes is enhanced by a factor of 2 (20) at redshift $z = 30$ (40). Moreover, also the collapsed DM fraction is higher and thus the relative contribution from PBHs accreting in the IGM is further lowered. The emissivity of PBHs accreting in haloes at redshift $z = 20$ (40) is roughly 10 (100) times the emissivity from PBHs in the IGM. We point out that, as a consequence of the aforementioned effects, in the PBH-ΛCDM cosmology the halo emissivity dominates the IGM one at any redshift, unlike in the standard ΛCDM case.

- If the radiative efficiency is indipendent of the accretion rate, given an extended mass function, the emissivity of PBHs accreting in the IGM can be computed adopting a delta mass function with mass equal to the mean mass of the mass function $\bar{M}_{\rm log}$. We compare the bolometric luminosity of haloes in the case of a delta mass function with $M_{\rm PBH} = 30$ M$_\odot$ and of a lognormal mass function with $\bar{M}_{\rm log} = 30$ $M_\odot$. Including the lognormal mass function boosts the halo luminosity by a factor of ~ 10, because more massive PBHs accrete at smaller distances from the center, where the gas density is higher.

- Considering $1 \leq M_{\rm PBH}$ [M$_\odot$] $\leq 10^3$ and $f_{\rm PBH} = 1$, PBHs can produce at most ~ 1 per cent of the flux required to explain NIRB fluctuations. The three models differ in their prediction by less than a factor of $\simeq 2$. Although in PBH-ΛCDM cosmology the total emissivity of PBHs at $z \gtrsim 40$ is ~ 10 higher than in the standard ΛCDM scenario (for both delta and lognormal mass functions), the resulting NIRB is similar, because the gas heating from X-rays produced by PBHs damps their emissivity at lower redshifts.

- When accounting for current constraints on PBH abundance, the maximum relative contribution of PBHs to the NIRB is reduced to 0.1 per cent, for PBHs with $M_{\rm PBH} \sim 50$ M$_\odot$.

- None of our models is able to reproduce the NIRB angular power spectrum. At large angular scales ($\theta \sim 20$ arcmin), fluctuations predicted by model ΛCDM-δ (PBH-δ, PBH-lognormal) are lower than the measured one by a factor of 1000 $(400, 200)$, in the most favorable case with $M_{\rm PBH} = 10^3$ M$_\odot$.

Before concluding, we compare our findings with the results from Hasinger (2020b, hereafter Hasinger 2020b), whose model is adopted in Cappelluti et al. (2022). Hasinger 2020b predicted a NIR flux from PBHs of 10^{-13} erg s^{-1}cm^{-2}deg^{-2} $\sim 3 \times 10^{-4}$ nW m^{-2}sr^{-1}. This corresponds to ~ 0.3 per thousand of the NIRB flux required to explain NIRB fluctuations. Hence, we find a NIRB flux $\sim 10\times$ higher then the one obtained in Hasinger 2020b. We point out some substantial differences between the two models to fully grasp the discrepancy in the two results. Firstly, Hasinger 2020b adopt a non-linear relative velocity between gas and DM to capture the collapse of baryons into DM haloes. This approach does not account for the density profile of DM and gas inside haloes, which enhance the contribution of PBHs accreting in haloes, as gas densities are much higher than the mean baryon density. Secondly, Hasinger 2020b estimates as negligible the heating of accreting gas by X-rays produced by PBHs, which instead in our model provides a negative feedback on the PBH emissivity. Moreover, Hasinger 2020b adopts an extended mass function with a peak around $1 \sim \mathrm{M}_\odot$, but with broad tails reaching up to $10^9 \sim \mathrm{M}_\odot$. They conclude that the dominant contribution arises from PBHs with $M_{\rm PBH} \sim 10^4 \sim \mathrm{M}_\odot$, while we focused only on the range $1 \leq M_{\rm PBH}/\mathrm{M}_\odot \leq 10^3$. A final difference concerns the accretion parameter, which they assume to be $\lambda = 0.05$, i.e. $5\times$ higher than the one adopted here.

To summarize, even if our modelling for the PBH contribution to the NIRB excess differs from the Hasinger 2020b one, we don't end up with a dramatic discrepancy. This is because the extra physical effects that we have included tend to balance each other. In fact, we should have expected a much higher NIRB flux due to the contribution of PBHs accreting in haloes and the boosted matter power spectrum due to the presence of the PBHs. However, these effects are balanced by the inclusion of the IGM heating from PBH X-ray emission that damps their emissivity at lower redshifts.

Primordial black holes as supermassive black holes seeds

7

7.1 Introduction

It has been proposed that PBHs may constitute the seeds of SMBHs (e.g. Düchting, 2004; Kawasaki et al., 2012). PBHs formed with low masses ($M_{\rm PBH} \sim 100\ M_{\odot}$), can mimic the *light seeds* scenario; in this case, however, they would have more time to accrete with respect to PopIII remnants (Bernal et al., 2018). Alternatively, if originated during inflation, they might be as massive as the seeds expected in the *intermediate/heavy* seeds scenarios ($M_{\rm PBH} \sim 10^3 - 10^5\ M_{\odot}$, e.g. Hasinger, 2020b; Cappelluti et al., 2022). Furthermore, PBHs may participate to the growth of stellar compact remnants (neutron stars and stellar-mass black holes) while migrating towards the galactic nuclear region, because of gas dynamical friction (Boco et al., 2020, 2021).

In this work, we propose a new seeding mechanism based on 30 $\rm M_{\odot}$ PBHs, distributed in the very central region ($\lesssim 1$ pc) of high-z ($z > 20$) rare ($\sigma \geq 5$) DM halos. The paper is organized as follows: in Sec. 7.2, we describe the semi-analytic model we developed to produce SMBH seeds; in Sec. 7.3, we present the outcomes of our model, in terms of seed masses and epochs of their formation, and we explore the implications of our seeding mechanism on the formation of early SMBHs; in Sec. 7.4, we summarize the main ingredients and findings of our model and we discuss caveats of our results

7.2 Model

In this section, we describe the model we use to investigate whether PBHs can be considered as valid candidates for SMBH seeds. Fig. 7.1 shows a schematic view of the model: we start from a configuration in which PBHs represent a fraction $f_{\rm PBH} = \Omega_{\rm PBH}/\Omega_{\rm dm}$ of dark matter (Sec. 7.2.1) that coexists with and accretes baryons (Sec. 7.2.3) that are settled in the potential well of a DM halo in the form of cooled gas (Sec. 7.2.2); PBHs loose angular momentum as a consequence of the dynamical friction on the gas and gather in the central region of the potential well forming a dense core, PBHs accretion hampers star formation through radiative feedback (Sec. 7.2.4); PBHs clustered in the core undergo a runaway collapse that ends up into a massive BH whose mass depends on the initial conditions of the configuration (Sec. 7.2.5).

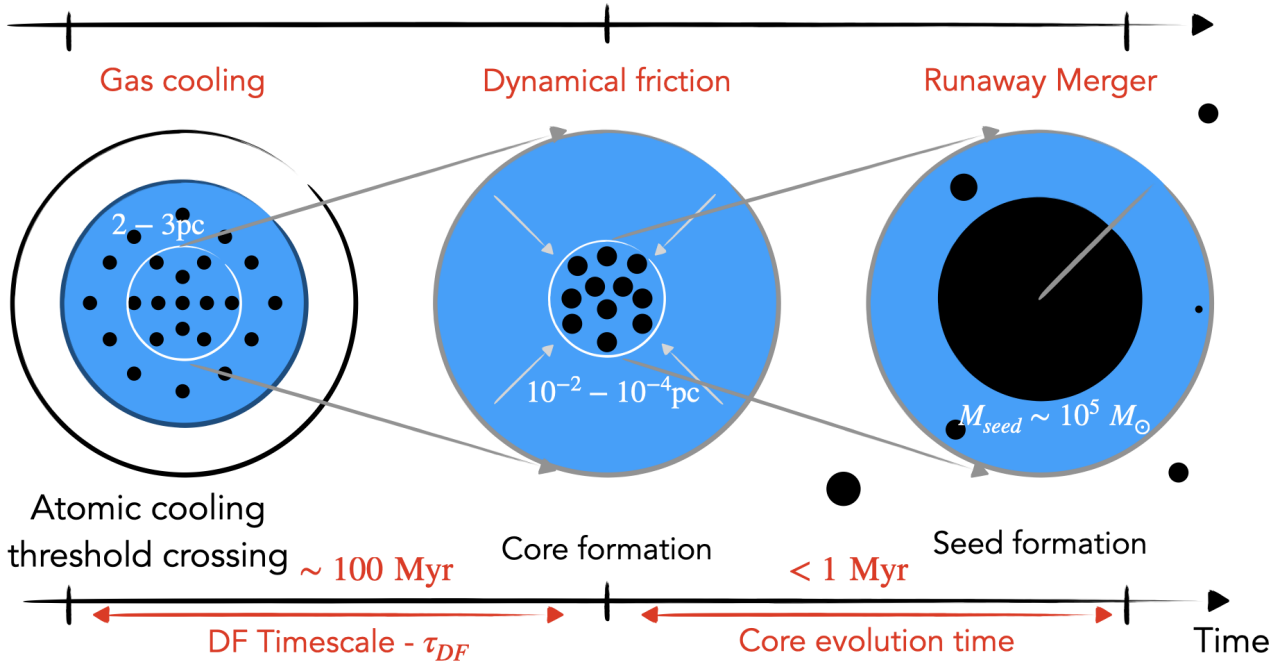

Figure 7.1: Schematic description of the seed formation process presented in this work. High density peak in the early Universe collapse forming dark matter halos comprised of PBHs. The halo mass increases as cosmic time progresses, reaching a point where its temperature surpasses the atomic cooling threshold. This initiates the gas cooling process within the halo. As the gas cools, it becomes denser and settles towards the center of the dark matter gravitational potential, embedding the PBHs at the center. PBHs accreting and moving into dense gas lose angular momentum due to dynamical friction and gather in a core. At the moment that the core is dense enough to retain the products of binary merging, it starts to evolve. PBH binaries form and merge extremely rapidly due to the high density, ultimately resulting in a runaway merger phase. The core is finally converted into a seed.

7.2.1 Halo and gas modelling

We model dark matter halos assuming a standard NFW Navarro, Frenk & White (NFW, Navarro et al., 1997) density profile:

$$\rho_{\rm dm}(r) = \frac{\rho_c \delta_c}{cx(1+cx)^2}, \tag{7.1}$$

where ρ_c is the critical density of the universe, δ_c is the critical density for the collapse, $x = r/r_{\rm vir}$ denotes the radial distance in units of the virial radius $r_{\rm vir}$.

The virial radius and temperature of a DM halo of mass M_h can be computed as (Barkana & Loeb, 2001):

$$r_{\rm vir} = 0.784 \left(\frac{M_h}{10^8\ h^{-1}\ M_\odot}\right)^{1/3} \left[\frac{\Omega_m}{\Omega_m^z}\frac{\Delta_c}{18\pi^2}\right]^{-1/3} \left(\frac{1+z}{10}\right)^{-1} h^{-1}\ {\rm kpc}, \tag{7.2}$$

$$T_{\rm vir} = 1.98 \times 10^4 \left(\frac{\mu}{0.6}\right) \left(\frac{M_{\rm vir}}{10^8\ h^{-1}\ M_\odot}\right)^{2/3} \left[\frac{\Omega_m}{\Omega_m^z}\frac{\Delta_c}{18\pi^2}\right]^{1/3} \left(\frac{1+z}{10}\right)\ {\rm K}, \tag{7.3}$$

where the overdensity[1] relative to ρ_c at the collapse redshift can be expressed as $\Delta_c = 18\pi^2 + 82d - 39d^2$, with $d = \Omega_m^z - 1$ and $\Omega_m^z = \Omega_m(1+z)^3/(\Omega_m(1+z)^3 + \Omega_\Lambda)$; Δ_c is related to δ_c through the following relation:

$$\delta_c = \frac{\Delta_c}{3}\frac{c^3}{ln(1+c) - c/(1+c)}, \tag{7.4}$$

where the concentration parameter c is computed following the model described in Prada et al. (2012).

We assume that the gas is distributed following a singular isothermal radial density profile and is in hydrostatic equilibrium with dark matter (Makino et al., 1998):

$$\rho_g(r) = \rho_0 \exp\left(-\frac{\mu m_p}{2k_B T_g}[v_e^2(0) - v_e^2(r)]\right), \tag{7.5}$$

where ρ_0 is obtained normalizing the total mass integrated over the profile to the gas mass $M_g = (\Omega_b/\Omega_m)M_h$, and $T_g = T_{\rm vir}(M_h, z)$.

7.2.2 Halo growth and gas cooling

As time passes, DM halos grow through minor/major mergers and accretion from the IGM, and their mass evolution can be described through the following relation (Fakhouri et al., 2010):

$$\frac{dM_h}{dt} = 46.1\left(\frac{M_h}{10^{12}M_\odot}\right)^{1.1}(1+1.11z)\sqrt{\Omega_m(1+z)^3+\Omega_\Lambda}M_\odot {\rm yr}^{-1}. \tag{7.6}$$

When M_h becomes large enough to have a virial temperature above the atomic cooling threshold[2] $T_g = 10^4$K, a fraction $f_g = 0.1$ of the gas mass cools down to the same temperature[3] and reaches high density values ($n_{g,0} \sim 10^2 - 10^5$ cm^{-3}), that favors the BH accretion and starts the dynamical friction process described below. Hereafter, we call "crossing redshift" ($z_\times$) and "crossing mass" ($M_{h,\times}$) the redshift and the halo mass when $T_{\rm vir}(M_h, z) = 10^4$ K. We consider these values as the initial conditions for the calculations described below.

7.2.3 PBH distribution and accretion

We populate the halo with PBHs following the DM density profile:

$$N_{\rm PBH}(r) = f_{\rm PBH}\frac{4\pi}{M_{\rm PBH}}\int_0^r \rho_{\rm dm}(r')r'^2 dr', \tag{7.7}$$

where[4] $M_{\rm PBH} = 30\ M_\odot$ is the PBH mass (e.g. Ziparo et al., 2022) and $f_{\rm PBH}$ is constrained in Sec. 7.3.3.

[1] We adopt a ΛCDM cosmology in agreement with Planck18 (Planck Collaboration et al., 2020) results: $\Omega_m = 0.315, \Omega_\Lambda = 0.685, \Omega_b = 0.049, \sigma_8 = 0.811, n_s = 0.965$, and $H_0 = 100\,h$ km s^{-1} Mpc^{-1} $= 67.4$ km s^{-1} Mpc^{-1}.

[2] The assumed value $T_g = 10^4$K is motivated by the gas composition (atomic hydrogen) at early epochs ($z \gtrsim 10$). The hydrogen cooling function has a sharp drop below this value (Katz et al., 1996).

[3] We expect the gas to be fully ionized by PBHs feedback in the central zone, and we assume a temperature of 10^4 K for the ionized gas (Anderson et al., 2009).

[4] We assume a monochromatic PBH mass function and we defer to a future work the investigation of extended mass functions.

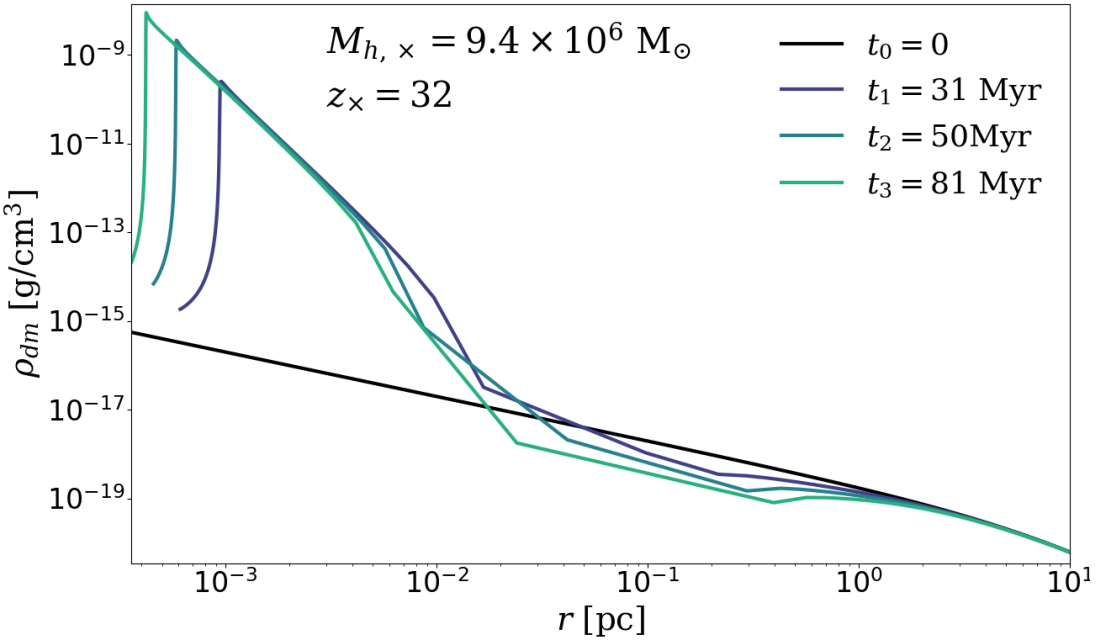

Figure 7.2: Dark matter density profile evolution with time. The black line ($t_0 = 0$) shows a classic NFW profile (Navarro et al., 1997). The purple, blue and green lines show the profile evolution at time $t_1 = 31$ Myr, $t_2 = 50$ Myr, $t_3 = 81$ Myr. The plot shows a DM density spike in the innermost part of the halo. This spike is caused by PBHs gradually shrinking their orbits due to gas dynamical friction.

PBHs accrete the surrounding gas following the Bondi-Hoyle-Lyttleton prescription (Hoyle & Lyttleton, 1939; Bondi & Hoyle, 1944):

$$\dot{M}_{\rm PBH} = \frac{G^2 M_{\rm PBH}^2 \rho_g}{(c_s^2 + v_{\rm PBH}^2)^{3/2}}, \tag{7.8}$$

where $c_s = (k_B T_{\rm g,c}/\mu m_p)^{1/2} {\rm km\ s^{-1}} = 8.3\ {\rm km\ s^{-1}}$ is the sound speed, and $v_{\rm PBH}$ is the relative velocity between gas and PBHs, here approximated to the circular velocity at a radius r as:

$$v_c(r) = \sqrt{\frac{G(M_g(r) + M_{\rm dm}(r))}{r}}. \tag{7.9}$$

The accretion rate is limited at the Eddington rate:

$$\dot{M}_{\rm E} = \frac{L_{\rm E}}{\varepsilon c^2}, \tag{7.10}$$

where $L_{\rm E} = 1.26 \times (M_{\rm PBH}/M_\odot) L_\odot$ is the Eddington luminosity, $\varepsilon = 0.1$ is the radiative efficiency, and c is the speed of light. The radiation emitted in this process provide thermal and ionization feedback (Hasinger, 2020b) strong enough to prevent H_2 formation, and therefore to hamper star formation. Since the volume filling factor of PBHs Strömgren spheres is O(1) in the central region of the halo ($r \sim$ pc), we consider the gas to be fully ionized ($T_g = 10^4$K).

7.2.4 Dynamical Friction

We treat the dynamics of a system of black holes orbiting in the halo potential and embedded in the halo gas, following Mo et al. (2010). Angular momentum loss of PBHs on the gas[5] reduces

[5]In contrast to what happens when a black hole moves through neutral gas, in fully ionized medium (Park & Bogdanović, 2017) and for a black hole in supersonic motion (Ostriker, 1999) the dynamical friction can work even

the orbits, bringing the black holes to form a dense cluster. The equation that regulates this process is:

$$\frac{dL}{dt} = -0.428 \ln \Lambda \frac{G M_{\rm PBH}}{r}, \tag{7.11}$$

where L is the specific angular momentum, and Λ is the Coulomb logarithm that depends on $M_{\rm PBH}$ and M_g through the following expression:

$$\ln \Lambda = \frac{1}{2} \ln \left[1 + \left(\frac{b_{\rm max}}{b_{90}} \right)^2 \right], \tag{7.12}$$

where $b_{\rm max}$ is the maximum impact parameter, and b_{90} is the impact parameter for which the deflection angle of the reduced particle of the encounter is equal to 90°. Following Binney & Tremaine (2008), we define $b_{\rm max} = r$, where r is the radius of the circular orbit assumed for PBHs, and $b_{90} = v_{\rm c}^2 / G M_\bullet$. Eq. 7.12 can thus be rewritten as:

$$\ln \Lambda = \frac{1}{2} \ln \left[1 + \left(\frac{M_g + M_{\rm dm}}{M_{\rm PBH}} \right)^2 \right]. \tag{7.13}$$

The dynamical friction on the gas has the effect of shrinking the radius of the PBH orbit with a rate dr/dt such that:

$$r \frac{dr}{dt} = -0.428 \ln \Lambda \frac{G M_{\rm PBH}}{v_c}. \tag{7.14}$$

This expression can be used to compute the dynamical friction timescale,

$$\tau_{\rm df} = \frac{1.17}{\ln \Lambda} \frac{r_i^2 v_c}{G M_{\rm PBH}}. \tag{7.15}$$

7.2.5 Runaway merger

Due to gas dynamical friction PBHs migrate towards the center of the gas ($r \leq 0.01$ pc) forming a cluster of PBHs. As a consequence of the PBH clustering, the distance between PBHs can become small enough for PBHs to form binaries and undergo runaway mergers, possibly leading to runaway merger that ends up with the formation of a single, massive black hole, which would represent the seed for a SMBH.

For this process to occur it is necessary that, after mergers, the products are retained within the core, namely that PBHs resulting from mergers are characterised by a recoil velocity v_k smaller than the escape velocity $v_{\rm esc}$ of the core (Davies et al., 2011). The kick velocity that a PBH can attain after the merging with another PBH, as a consequence of the asymmetric emission of gravitational radiation, depends on the mass ratio of the merging PBHs and on their spins. We adopt as a fiducial maximum value $v_k^{\rm max} = 1000$ kms^{-1} (Davies et al., 2011) and, in Appendix A.3, we quantify how much this assumption affects our results. Once that v_k is fixed, the condition for the runaway merger is given by:

$$v_{\rm esc}(r_c) = \sqrt{\frac{G M_c(r_c)}{r_c}} \geq v_k, \tag{7.16}$$

where r_c and M_c represent the radius and the mass of the core, respectively.

in the absence of stars.

These two quantities evolve with time, as a consequence of the PBH clustering and accretion processes that cause r_c to shrink and M_c to increase. This effect can be visualised in Fig. 7.2 that shows how the dark matter density profile evolves with time. Initially, the PBH distribution follows the NFW profile (solid black line). As time passes, PBHs accrete and sink in the central region, forming a core that becomes increasingly smaller and more massive (solid coloured lines), thus being characterised by an increasing escape velocity. In particular, $v_{\rm esc}$ can reach at a given time the critical value of $v_k^{\rm max}$, thus satisfying the condition for the runawy merger into a single BH. The mass of the BH resulting from this process is given by $M_{\rm seed} = N_{\rm PBH}(r_c) \times M_{\rm PBH}$, where $N_{\rm PBH}$ is the number of PBHs enclosed in r_c, determined as follows.

We first compute how the number of PBHs as a function of the radius $N_{\rm PBH}(r)$ evolves with time (solid curved lines in Fig. 7.3, for different crossing halos and redshifts). We find that in $\sim 10 - 100$ Myr, the dynamical friction boosts the PBH number in the core, shrinking PBHs orbits from < 10 pc down to $\sim 10^{-3}$ pc. We then define $N_{\rm cr}$ as the *critical number* of PBHs such that

$$v_{esc}(r) = \sqrt{\frac{G N_{\rm cr}(r) \times M_{\rm PBH}}{r}} = v_k^{\rm max}, \tag{7.17}$$

shown with dashed lines in Fig. 7.3. We underline that N_{cr} increases linearly with the radius and decreases with time. The time dependence is due to the fact that PBHs get more massive because of the accretion process; therefore, a smaller number of them is enough to verify the condition in Eq. 7.17. Fig. 7.3 shows that, at a given time, it can be identified the core radius r_c as the distance from the center that satisfies the following condition: $N_{\rm PBH}(r_c) \geq N_{\rm cr}(r_c)$.

In halos with crossing masses and redshifts such that the condition in Eq. 7.17 is verified during their evolution, the seed mass resulting from the runaway merger of PBHs in the core is given by $M_{\rm seed} = N_{\rm PBH}(r_c) \times M_{\rm PBH} = M_c(r_c)$.

7.3 Results

In this section, we present the results obtained by solving the three coupled differential equations regulating the PBH accretion (Eq. 7.8), the evolution of the halo mass (Eq. 7.6), and the shrinking of the PBH orbits (Eq. 7.14). We first quantify the seed masses, and the masses and redshifts of the host DM halos (Sec. 7.3.1); then, we provide instructions about the seeding prescription resulting from our work (Sec. 7.3.2), which can be used as an input of semi-analytical models and cosmological simulations; furthermore, we quantify the fraction of DM into PBHs ($f_{\rm PBH}$) required for this seeding mechanism to work (Sec. 7.3.3); finally, we check whether our model can provide a viable seeding mechanism to explain observations of $6 < z < 11$ SMBHs (Sec. 7.3.4).

7.3.1 Seed formation

Fig. 7.4 shows the redshift evolution of DM halos that reach masses $\sim 10^{10-13}\ M_\odot$ at $z = 6$, corresponding to $5-7\sigma$ fluctuations of the density field. We focus on this specific redshift range because the main goal of our work is to explain the existence of SMBHs at $z \gtrsim 6$. The figure shows that the crossing mass does not vary much with the σ fluctuation. For what concerns the crossing redshift, we find that the smaller is the σ fluctuation the lower is the crossing redshift, namely the redshift when the halo mass becomes larger that the atomic cooling mass threshold (e.g. $z \sim 20 - 40$ for $\sigma = 5 - 7$, respectively). This is due to the fact that lower σ fluctuations are characterised by longer dynamical friction timescales ($\tau_{df} \sim 10 - 100$ Myr for $\sigma = 5 - 7$).

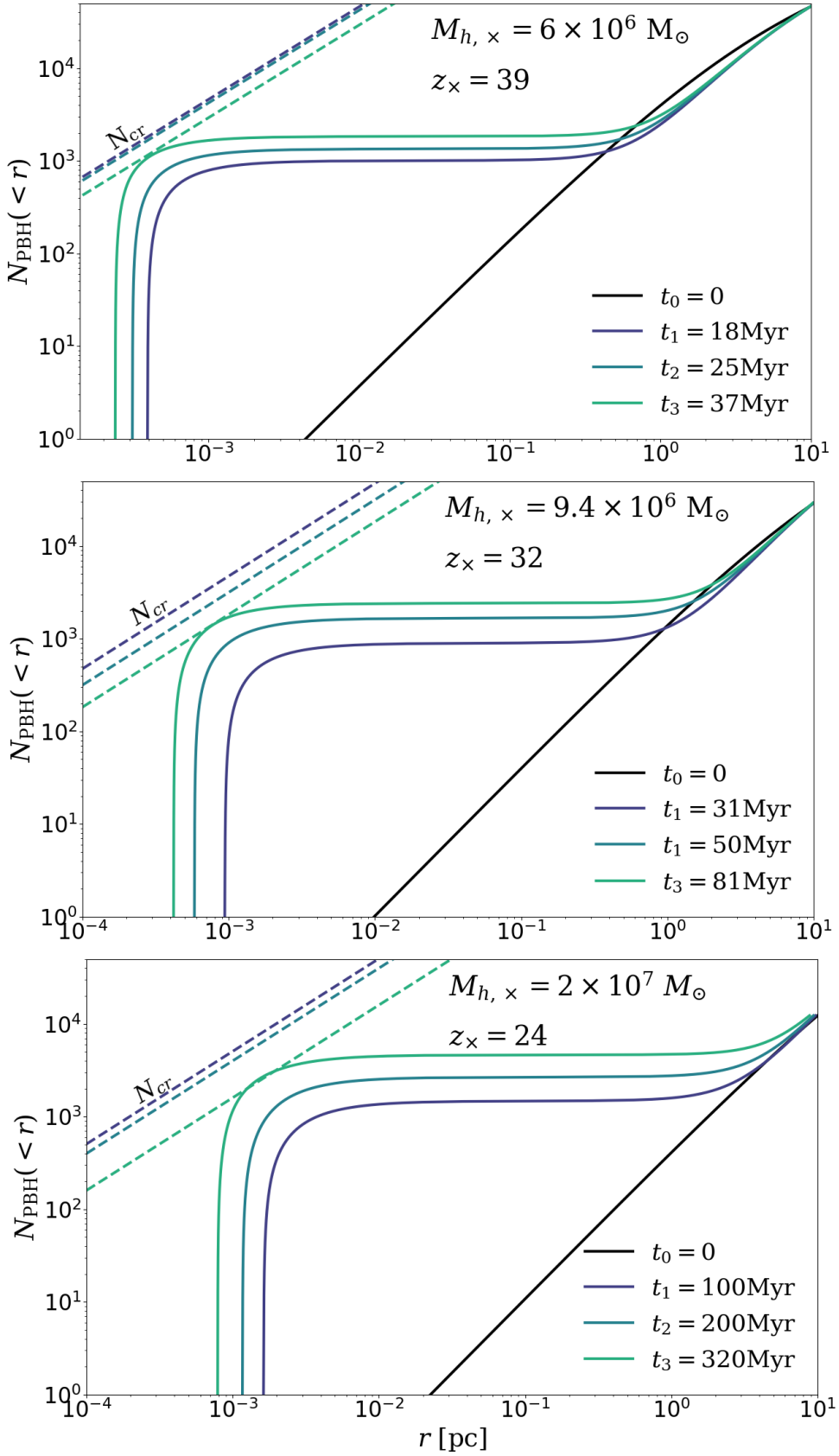

Figure 7.3: Time evolution of the PBH cumulative number within 1 pc of the DM halo center. Different panels represent different cases of the crossing redshift $z_\times$ and halo mass $M_{h,\times}$, as labelled in the figure. The black straight line represents the initial PBH distribution following the NFW profile; curved coloured lines show how the PBH distribution evolves with time due to gas dynamical friction; dashed straight lines denote the critical PBH cumulative number $N_{\rm cr}$ required to reach the escape velocity $v_{\rm esc} = 1000\ {\rm kms}^{-1}$.

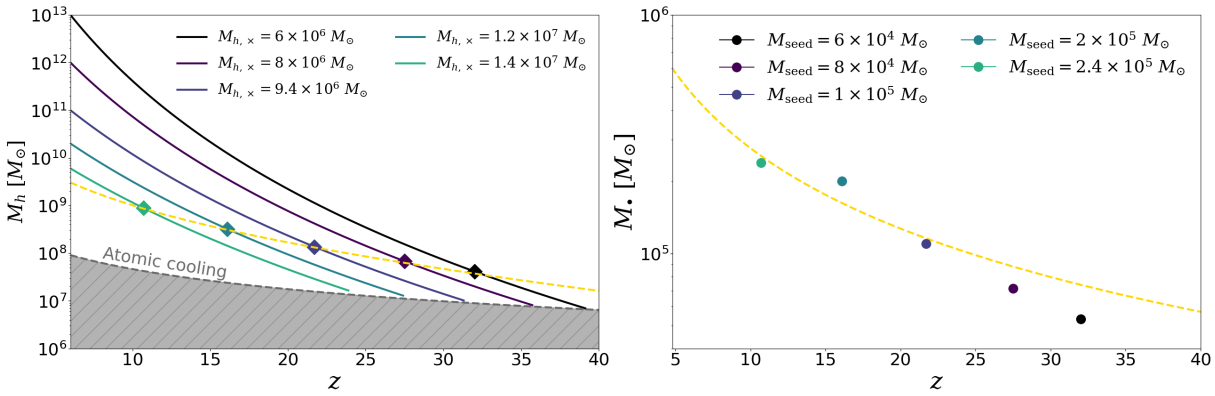

Figure 7.4: *Left panel:* Redshift evolution of DM halos characterized by $M_h \sim 10^{10-13}\ M_\odot$ masses at $z = 6$ and crossing masses $M_{h,\times} \sim 10^{6-7}\ M_\odot$ at $z_\times = 25 - 40$. Different lines show different $M_{h,\times}$ and $z_\times$ combinations, as labelled in the figure. Diamonds represent the DM halo mass at the time when the runaway merger occurs and the massive seed is formed. The golden dashed line denotes the best fit for the redshift evolution of the halo masses at the seed formation epoch (Eq. 8.1). The shaded grey area represents the $z - M_h$ parameter space below the atomic cooling threshold. Perturbations that are above the atomic cooling threshold at earlier times are larger and produce less massive seeds in shorter time, as detailed in the main text. *Right panel:* Seed mass evolution with redshift. Colored filled circles show the mass of different seeds associated to the halo masses (diamonds) in the right panel. The golden dashed line represents the best fit for the redshift evolution of the seed masses (Eq. 8.2).

Such differences arise from different initial conditions in the central part ($r \sim 10$ pc) of the halos at the crossing epoch. For $\sigma \simeq 7$, the high central gas density ($n_{g,0} \sim 10^5 \mathrm{cm}^{-3}$) implies efficient accretion and dynamical friction; furthermore, the high concentration ($c = 31$) corresponds to a larger number of PBHs in the central zone. For $\sigma \simeq 5$, the much smaller central density ($n_{g,0} \sim 10^3 \mathrm{cm}^{-3}$) makes the accretion and dynamical friction less efficient; furthermore, the lower concentration ($c = 8$) implies that a longer time is required to gather a number of PBHs large enough to reach the critical number $N_{\rm cr}$ (see Eq. 7.17).

We start the computation considering the crossing mass and redshift as initial conditions. At each timestep, we check if and when the condition in Eq. 7.17 is satisfied. The dots overplotted on the continuous lines in Fig. 7.4 denote the mass and redshift when this takes place. Since the core collapse occurs on a very short timescale (≤ 1 Myr), we identify the seed formation with the same redshift, and we report for each case the seed mass produced. Our model predicts the formation of massive seed ($M_\bullet \sim 10^{4-5}\ M_\odot$) in high-z ($10 < z < 30$) DM halos with masses $M_h \sim 5 \times 10^7 - 10^9\ M_\odot$.

We expect that the seed formation process described in this work naturally stops at $z \simeq 20$ due to the low gas and PBHs density in the halo center at the crossing time. For example, we verified that perturbations that cross the atomic cooling mass at $z \lesssim 22$ do not form a seed even after 1 Gyr.

7.3.2 Seeding prescription

We exploit the results reported in Sec. 7.3.1 to obtain a seeding recipe for theoretical models and simulations.

The diamonds in Fig. 7.4 (right panel) represent the masses that halos have at the time of the seed formation. By fitting these data (yellow dashed), we find that the mass of halos that produce a seed evolves with redshift following this relation:

$$M_{h,\rm seed}(z) = 2 \times 10^9\ M_\odot \left(\frac{1+z}{10}\right)^{-2} e^{-0.05z}. \tag{7.18}$$

Similarly, dots in Fig. 7.4 (left panel) denote how the mass of the seed formed changes with redshift, which can be fitted (yellow dashed) by the following equation:

$$M_{\rm seed}(z) = 3.1 \times 10^5 \, M_\odot \left(\frac{1+z}{10}\right)^{-1.2}. \tag{7.19}$$

Eq. 8.1-8.2 provide a very simple seeding prescription: at any redshift, both the mass of the halo and the mass of the BH that must be seeded in it are defined.

7.3.3 Fraction of DM into PBHs

As we show in Fig. 7.2, we only considered the central 10 pc of the halo in our computation. In that region, we assumed that all the dark matter is in the form of PBHs. This assumption appears to be strong, given the already existing observational constrains on $f_{\rm PBH}$ around $M_{\rm PBH} = 30\,M_\odot$ (see e.g. Carr & Kühnel 2020). We argue that $f_{\rm PBH}$ has to be differentiate into two regimes: $f_{\rm PBH} = 1$ in the central part of rare dark matter halos ($\sigma \geq 5$), and $f_{\rm PBH} = 0$ elsewhere.

$$f_{\rm PBH} = \begin{cases} 1 & \text{if } r \leq 10 \text{ pc}, \\ 0 & \text{if } r > 10 \text{ pc}. \end{cases}$$

To compute an upper limit on the global fraction of DM into PBHs, we make the strong assumption that the entire DM halo is made of PBHs at the crossing redshift. We thus compute the minimum amount of the PBH energy density necessary for the described seeding mechanism to occur as:

$$\rho_{\rm PBH,min} = \int_{z_2}^{z_1} dz \, M_{\rm cool}(z) \frac{dn(M_h, z)}{dM}, \tag{7.20}$$

where $z_1 \sim 22$ and $z_2 \sim 40$, are the minimum and the maximum crossing redshifts of the rarest ($\gtrsim 5\sigma$ fluctuations) DM halos that produce massive seeds (see left panel of Fig. 7.4), $M_{\rm cool}(z)$ is the atomic cooling threshold mass, and $dn(M_h, z)/dM$ is their halo mass function. We compare this quantity with the DM energy density at z_2:

$$f_{\rm PBH} = \frac{\Omega_{\rm PBH}}{\Omega_{\rm dm}} = \frac{\rho_{\rm PBH,min}}{\Omega_{\rm dm}\rho_{c,0}(1+z_2)^3}, \tag{7.21}$$

and we find that the minimum fraction of DM into PBHs required for the process to occur is extremely small ($f_{\rm PBH} \gtrsim 7 \times 10^{-10}$) and not ruled out by current observational constraints. We expect this minimum fraction to be even smaller, as only a part ($\sim 0.01\%$) of the halo crossing mass ($M_{h,\times}$) is contained in the central 10 pc that we consider for our computation.

We underline that our seeding mechanism is expected to occur only in high-σ fluctuations of the density field; therefore while computing $f_{\rm PBH}$ we are assuming that PBHs at the epoch of their formation are clustered in those regions that will evolve into rare, massive DM halos. However, in a standard Gaussian power spectrum of primordial fluctuations, PBHs spatial distribution is not expected to have any initial clustering (Ali-Haïmoud, 2018; De Luca et al., 2022). The absence of clustering intrinsically arises from the form of the power spectrum that implies no coupling between long- and short-wavelength modes (Tada & Yokoyama, 2015). In this framework, PBHs formation solely depends on the density contrast at the PBH scale, and whether or not its value is larger that the critical density for PBH formation. In the presence of small non-gaussianity in the primordial power spectrum, the coupling between long- and short-wavelength modes is naturally present. Mode coupling has a dual effect (Tada & Yokoyama, 2015): to reduce the

critical density required for the PBH formation by a factor that depends on the density contrast on scales larger than the ones involved in the PBH formation process itself; to boost the variance of short-wavelength perturbations. These two effects ultimately result into an initial clustering of PBHs at the formation epoch in correspondence of density peaks at larger scales.

7.3.4 Implications for early SMBHs

We use our model to interpret observations of early ($6 < z < 10$) SMBHs (Table 7.1). We adopt estimates found in literature for the mass of the SMBH hosting halo. We then track M_h backward in time, following Fakhouri et al. (2010). Once that the crossing redshift ($z_\times$) and mass ($M_{h,\times}$) are determined, our model allows us to compute: the redshift ($z_{\rm seed}$), the mass ($M_{\rm seed}$), and the halo mass ($M_{h,{\rm seed}}$) of the seed, as well as the average Eddington ratio $\langle\lambda_{\rm E}\rangle$ to which the seed should accrete to explain the observed SMBH masses (or X-ray luminosity, see below).

In Fig. 7.5, we show both observational data and the seed masses resulting from our model (coloured as in Fig. 7.4).

We find that $z \sim 6$ quasars can be explained with $6 \times 10^4 M_\odot$ seeds, planted at $z \sim 32$, and growing at a sub-Eddington pace $\langle\lambda_{\rm E}\rangle \sim 0.55$. A similar scenario ($\langle\lambda_{\rm E}\rangle \sim 0.48$) can also reproduce the BH mass of GNz11 at $z = 10.6$. However, we cannot reproduce the UV luminosity of this source, which is instead consistent with $\lambda_{\rm E}^{\rm obs} \sim 5.5$. We emphasize here that $\langle\lambda_{\rm E}\rangle$ must not be considered a proxy of $\lambda_{\rm E}^{\rm obs}$. In fact, while $\langle\lambda_{\rm E}\rangle$ provides an average value on the lifetime of the seed, $\lambda_{\rm E}^{\rm obs}$ represents the accretion rate of the BH at the time of the observation. Our model cannot predict the amplitude of variations around the average value, that are typically associated to the SMBH accretion process. Observations of $z \sim 6$ quasars (Farina et al., 2022; Mazzucchelli et al., 2023) are consistent with variations of the order of $\Delta\lambda_{\rm E}/\langle\lambda_{\rm E}\rangle \sim 70\%$ ($\langle\lambda_{\rm E}^{\rm obs}\rangle \sim 0.46 \pm 0.32$). Whether variations of the accretion rate are occurring with similar amplitudes in earlier phases of BH growth is unknown. However, if this is the case, our estimate $\langle\lambda_{\rm E}\rangle \sim 0.48 \pm 0.34$ implies that we can easily accomodate moderate episodes of super-Eddington accretion $\lambda_{\rm E}^{\rm obs} \sim 1-2$, while $\lambda_{\rm E}^{\rm obs} \sim 5.5$ values are difficult to reproduce (see also Bhatt et al. 2024).

For what concerns UHZ1, since the BH mass is not known, we prefer to quantify the minimum $\langle\lambda_{\rm E}\rangle$ value that can reproduce the X-ray luminosity $L_X \geq 2 \times 10^{44}$ ergs^{-1} estimated by Bogdan et al. (2023b). UHZ1 data favour a scenario perfectly consistent with the one drawn by Bogdan et al. (2023b): seeds must have been planted slightly later ($z \lesssim 22$) than the other two cases, are more massive ($1 \times 10^5 M_\odot$) and more efficiently accreting ($\langle\lambda_{\rm E}\rangle = 0.9$), ending up into a $M_\bullet \sim 4 \times 10^7 M_\odot$ at $z = 10.1$.

We use a similar approach for UHZ9. Due to the absence of a direct BH mass measurement, we quantify the minimum $\langle\lambda_{\rm E}\rangle$ value that can reproduce the bolometric luminosity $L_{\rm B} \gtrsim 10^{46}$ ergs^{-1} estimated by Kovacs et al. (2024b). Similarly to UHZ1 case, slightly late ($z \sim 25$), and more efficiently accreting ($\lambda_E = 0.96$) seeds are preferred. Starting from initial masses of $0.9 \times 10^5\ M_\odot$, these seeds evolve into very massive BHs ($M_\bullet = 1 \times 10^8\ M_\odot$) at redshift $z = 10$.

By comparing the PBH seeding mechanism with other scenarios, we find that, since PBH seeds form at high redshift ($z \sim 20-40$) with high masses $M_{\rm seed} \sim 10^5\ M_\odot$, the mean accretion rate required to produce SMBHs at $z \sim 6-10$ is less extreme than the ones requested by the NSC (red box in Fig. 7.5) and PopIII (green box) scenarios, and comparable to the DCBH one (blue box).

Table 7.1: Observations and predictions for $6 < z < 10$ SMBHs. For $z \sim 6$ quasars we consider $M_h = 10^{13} M_\odot$ (Costa, 2023). For UHZ1 (GNz11; UHZ9), given the estimated stellar mass of $M_* \simeq 2.0 \times 10^8 M_\odot$ ($M_* \simeq 6 \times 10^8 M_\odot$; $M_* \simeq 3.3 \times 10^8 M_\odot$ Atek et al. 2023; Castellano et al. 2023), and assuming $M_* = \epsilon_* (\Omega_b/\Omega_m) M_h$, with a star formation efficiency $\epsilon_* = 0.1$, we find $M_h = 2.0 \times 10^{10} M_\odot$ ($M_h = 2 \times 10^{11} M_\odot$; $3.3 \times 10^{10} M_\odot$). For $\lambda_{\rm E^{obs}}$ we report the values from Farina et al. 2022; Mazzucchelli et al. 2023 and Maiolino et al. 2023(GNz11).

	Quasars	UHZ1	GNz11	UHZ9
OBSERVATIONS				
z	6	10.1	10.6	10
$M_\bullet [M_\odot]$	10^9	$4{\times}10^7$	$2{\times}10^6$	10^8
$M_h [M_\odot]$	10^{13}	$2.0{\times}10^{10}$	2×10^{11}	2×10^8
$\lambda_{\rm E}^{\rm obs}$	0.46 ± 0.32	-	5.5	-
PREDICTIONS				
$z_{\rm seed}$	32	21.7	27.5	25
$M_{\rm seed} [M_\odot]$	6×10^4	1.1×10^5	0.8×10^5	0.9×10^5
$M_{h,{\rm seed}} [M_\odot]$	4×10^7	1.5×10^8	0.7×10^8	0.7×10^8
$\langle \lambda_{\rm E} \rangle$	0.55	0.92	0.48	0.96

7.4 Summary and discussion

We have shown that runaway mergers of PBHs in the central region ($r < 1$ pc) of high redshift ($20 < z < 40$) halos can lead to the formation of massive black hole seeds. This mechanism provides a new route to rapid SMBH growth. The main results of this study are:

- Due to dynamical friction on dense gas in early dark matter halos, PBHs of mass $\simeq 30\ M_\odot$ tend to concentrate into a compact ($r_c \sim 10^{-3}$ pc) core containing $\simeq 1000$ PBHs. At such high concentration, PBHs form binaries triggering their runaway merger process, eventually leading to a massive ($10^{4-5}\ M_\odot$) BH seed.

- Massive BH seeds predominantly form in early ($6 < z < 30$), rare halos of mass $5 \times 10^7 - 10^9\ M_\odot$, representing $\gtrsim 5\sigma$ fluctuations of the density field. Based on these results we derive a physical seeding prescription (eq. 8.1 and eq. 8.2) that can be used in theoretical and numerical studies.

- Our seeding mechanism can explain recent JWST observations of early SMBHs (Maiolino et al., 2023; Bogdan et al., 2023b; Kovacs et al., 2024b), without the need for super-Eddington accretion. Moreover, our predictions nicely agree with the observed properties of $z \sim 6$ quasars, matching at the same time the host dark matter halo ($M_h \sim 10^{12-13}\ M_\odot$),

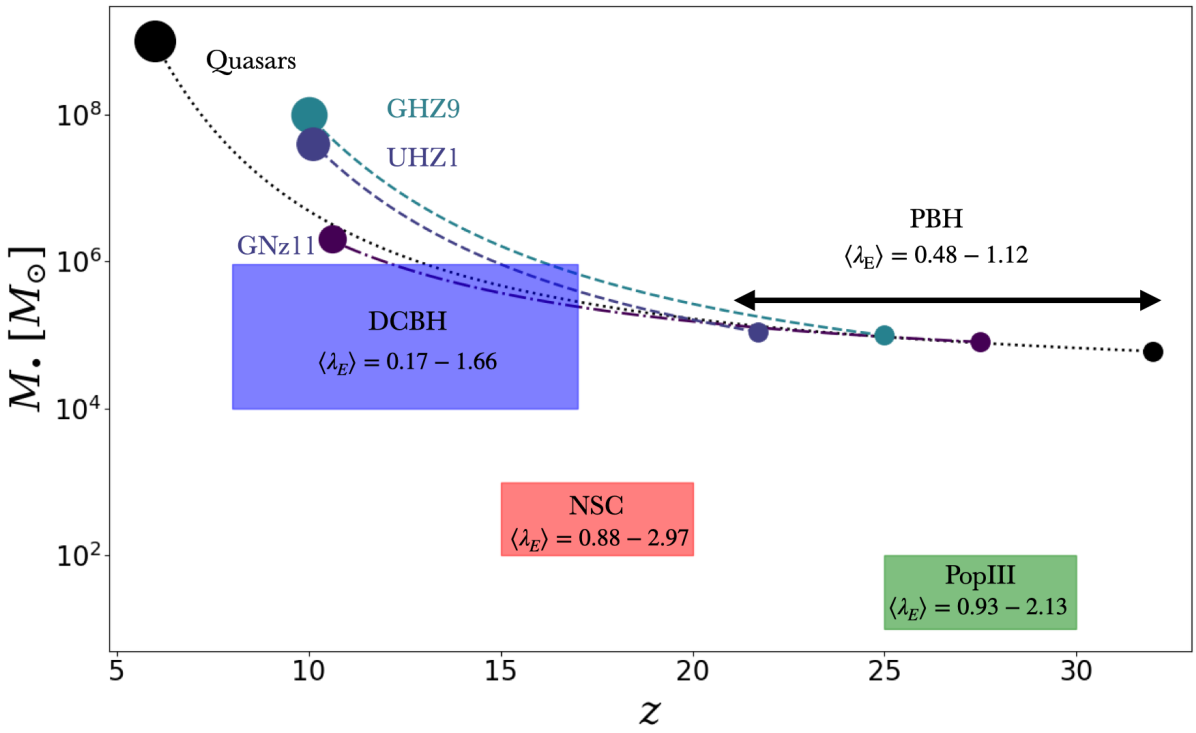

Figure 7.5: Growth of PBH seeds accreting into $z \sim 6 - 10$ SMBHs. Large (small) circles represent SMBH observations (predicted PBH seeds). By assigning the halo mass to the observed SMBH hosts and evolving it back in cosmic time, we link each SMBH to its PBH progenitor. Dashed and dotted lines represent the assembly of the SMBHs assuming the constant mean accretion rate $\langle\lambda_E\rangle$ reported in Tab. 7.1. We find that PBH seeds can explain the masses of $z \sim 6 - 10$ SMBHs with $0.48 < \langle\lambda_E\rangle < 1.12$ (see Fig. A.4 for further details). Colored boxes report the redshift and mass ranges for different seeding scenarios: $z = 8-17$ and $M_{\rm seed} = 10^{4-6}\ M_\odot$ for DCBHs (blue box, Ferrara et al., 2014); $z = 15 - 20$ and $M_{\rm seed} = 10^{2-3}\ M_\odot$ for NSCs (red box, Volonteri et al., 2003); $z = 25 - 30$ and $M_{\rm seed} = 10^{1-2}\ M_\odot$ for PopIII remnants (green box Madau & Rees, 2001). For each seeding scenario, we report the minimum and maximum $\langle\lambda_E\rangle$ value required to explain the observed masses of $z \sim 6 - 10$ SMBHs. The PBH seeding mechanism combines the early birth ($z \gtrsim 20$) of *light/intermediate* seeds with the high masses ($M_{\rm seed} \sim 10^5\ M_\odot$) of *heavy* seeds. Thus, PBH seeds can explain $z \sim 6 - 10$ SMBH observations by growing with less extreme $\langle\lambda_E\rangle$ values.

and SMBH ($M_\bullet \sim 10^{8-10}\ M_\odot$) masses with a conservative mean accretion rate, $\langle\lambda_E\rangle \sim 0.5$.

- Our seeding mechanism combines the early birth ($z \gtrsim 20$) of *light/intermediate* seeds with the high masses ($M_{\rm seed} \sim 10^5\ M_\odot$) of *heavy* seeds, resulting in less stringent requirements on the BH accretion history.

- The proposed BH seed formation process is expected to copiously emit gravitational waves during the thousands of PBH-PBH mergers occurring in the runaway phase. We defer to future work a calculation of the resulting GW signal, its contribution to the stochastic GW background, and detectability with future GW instruments, such as the Einstein Telescope (Punturo et al., 2010).

Although we consider our results as fairly robust, a number of assumptions made deserve further scrutiny. In Sec. 7.2, we have assumed that star formation is suppressed in the central regions of the halo. This assumption is based on two heuristic arguments: (i) competitive accretion by PBHs should rapidly devoid the gas, thus strongly inhibiting its conversion into stars; (ii) UV radiation produced by PBH gas accretion should largely photo-dissociate H_2 molecules, again preventing star formation.

It is worth noting, though, that the proposed seeding mechanism might work equally well even in the presence of stars. Although we considered only dynamical friction on the gas, the inclusion of a stellar component would also contribute to friction. For a standard 1-100 $M_\odot$ Salpeter stellar IMF (Salpeter, 1955), 30 $M_\odot$ PBHs are heavier than $\gtrsim 99\%$ of the stars. We then expect PBHs to sink towards the halo center, similarly to the gas-only case, by kicking out lighter stars.

We have also neglected the effect that minor and major mergers of DM halos could have on the PBH core formation process. DM halo mergers modify the halo density profile, and may perturb the orbits of PBHs as they sink towards the halo center. As for minor mergers, it has been shown that their effect is to smoothly feed the halo outskirts without significantly affecting the halo central regions (Salvador-Solé et al., 1998). Major mergers might be in principle more disruptive, as they can alter even the central distribution of dark matter. If so, they could possibly hamper the settling of the PBH core. However, the physical process proposed here is effective only in high-σ density fluctuations, for which major mergers are rare. In other words, major mergers are likely affecting the number of seeds produced by our model, but they should not prevent their formation entirely. Nevertheless, a quantitative assessment of major merger effects on the results presented in this work will require dedicated numerical simulations.

Part III

Conclusions and future prospects

Summary

8

In this Thesis, we have explored the possibility that PBHs can solve some of the puzzles arising from recent observational campaigns, as outlined in the abstract of this document. First of all, we have focused our study on the following open question:

Can PBHs be the sources of the observed backgrounds excess?

We developed a semi-analytical model that is based on the assumption that PBHs constitute a fraction $f_{\rm PBH}$ of cold dark matter (DM), and that allows us to compute the accretion rate and the relative luminosity of PBHs in dark matter halos and in the IGM. We underline that we self-consistently derive the IGM temperature evolution, considering ionization and heating due to X-ray emission from PBHs. In this framework, we explored the possibility that radiation emitted by accreting PBHs could contribute to the X-ray (CXB), the radio (CRB), and the near infared (NIRB) backgrounds.

For what concerns the comparison with CXB and CRB observations, we have based our model on the ΛCDM linear matter power spectrum, and considered a δ function for the PBH mass distribution at $30 M_{\odot}$. Hereafter, we refer to this model with the term ΛCDM-δ model. Our main results are the following:

- By comparing the cumulative X-ray emission from PBHs predicted by our model with the observed CXB, we set the strongest existing constraint on $f_{\rm PBH} \leq 3 \times 10^{-4}\ (30/M_{\rm PBH})$ in the mass range $1 - 1000\, M_{\odot}$.

- By comparing the PBH radio emission predicted by our model with the measured CRB, we find that the predicted brightness temperature $T_b(1.4\ {\rm GHz}) \sim 0.004\ {\rm K}$ resulting from our model represents only a small fraction ($\sim 1\%$) of the radio excess observed by ARCADE2.

For what concerns the comparison with NIRB observations, we have varied the δ function describing the PBH mass function in the mass range $1 < M_{\rm PBH}/M_{\odot} < 10^3$. Furthermore, besides the ΛCDM-δ model, we have considered the possibility that PBHs modify the matter power spectrum. In this case, we have considered two possibilities: (i) the PBH mass distribution is described by a δ function in the mass range $1 < M_{\rm PBH}/M_{\odot} < 10^3$ (PBH-δ model); (ii) the PBH mass distribution follows an extended lognormal mass function (PBH-lognormal model), with a mean PBH mass $\bar{M}_{\rm log}$ varying in the same range of the δ functions. For each model, we have derived the mean intensity and angular power spectrum of the NIRB arising from the accretion onto PBHs, finding the following main results:

- Considering $f_{\rm PBH} = 1$, PBHs can produce at most $\sim 1\%$ of the NIRB intensity, for $M_{\rm PBH} = \bar{M}_{\rm log} = 10^3\ {\rm M}_{\odot}$. The three models differ in their prediction by less than a

factor of $\simeq 2$. Although in both PBH-δ and PBH-lognormal models the total emissivity of PBHs at high redshift ($z \gtrsim 40$) is ~ 10 higher than in the standard ΛCDM-δ model, the resulting NIRB is similar, because the gas heating from X-rays produced by PBHs damps their emissivity at lower redshifts.

- When accounting for current constraints on PBH abundance, the maximum relative contribution of PBHs to the NIRB is reduced to 0.1%, for PBHs with $M_{\rm PBH} \sim 50$ M.

- None of our models is able to reproduce the NIRB angular power spectrum. At large angular scales ($\theta \sim 20$ arcmin), fluctuations predicted by model ΛCDM-δ (PBH-δ, PBH-lognormal) are lower than the measured one by a factor of 1000 $(400, 200)$, in the most favorable case with $M_{\rm PBH} = 10^3$ M.

Given the main results discussed so far, we conclude that PBHs are not the sources responsible for the observed background excesses.

The second open question we have tackled is the following:

Can PBHs lead to the formation of SMBHs seeds?

Similarly to what we have done in the semi-analytical model described above, we populated DM haloes with PBHs, assuming that they constitute a fraction $f_{\rm PBH}$ of DM. We then computed the dynamical friction exerted by gas on the dynamics of the PBHs in the innermost region of DM halo. We have shown that runaway mergers of PBHs in the central region ($r < 1$ pc) of high redshift ($20 < z < 40$) halos can lead to the formation of massive black hole seeds. This mechanism provides a new route to rapid SMBH growth. The main results of this study are:

- Due to dynamical friction on dense gas in early dark matter halos, PBHs of mass $\simeq 30\,M_\odot$ tend to concentrate into a compact ($r_c \sim 10^{-3}$ pc) core containing $\simeq 1000$ PBHs. At such high concentration, PBHs form binaries triggering their runaway merger process, eventually leading to a massive ($10^{4-5}\,M_\odot$) BH seed.

- Massive BH seeds predominantly form in early ($6 < z < 30$), rare halos of mass $5 \times 10^7 - 10^9\,M_\odot$, representing $\gtrsim 5\sigma$ fluctuations of the density field. We derive a physical seeding prescription that can be used in theoretical and numerical studies:

$$M_{h,\rm seed}(z) = 2 \times 10^9\,M_\odot \left(\frac{1+z}{10}\right)^{-2} e^{-0.05z}; \tag{8.1}$$

$$M_{\rm seed}(z) = 3.1 \times 10^5\,M_\odot \left(\frac{1+z}{10}\right)^{-1.2}. \tag{8.2}$$

  These equations provide, for a given redshift, the mass of the haloes that produce a SMBH seed and the mass of the seed itself.

- Our seeding mechanism can explain recent JWST observations of early SMBHs without the need for super-Eddington accretion. Moreover, our predictions nicely agree with the observed properties of $z \sim 6$ quasars, matching at the same time the host dark matter halo ($M_h \sim 10^{12-13}\,M_\odot$), and SMBH ($M_{\rm BH} \sim 10^{8-10}\,M_\odot$) masses with a conservative mean accretion rate, $\langle \lambda_E \rangle \sim 0.5$.

Given the main results related to this second open question, we conclude that PBHs provide a promising route for the formation of SMBH seeds. Our seeding mechanism combines in fact the early birth ($z \gtrsim 20$) of *light/intermediate* seeds with the high masses ($M_{\rm seed} \sim 10^5\ M_\odot$) of *heavy* seeds, resulting in less stringent requirements on the BH accretion history.

Interestingly, the proposed seed formation process is expected to copiously emit gravitational waves during the thousands of PBH-PBH mergers occurring in the runaway phase. We defer to future work a calculation of the resulting GW signal, its contribution to the stochastic GW background, and detectability with future GW instruments, such as the Einstein Telescope.

Supplementary material

A.1 Halo concentration

Halo concentration describes the central density of an halo in terms of its mean density. It can be expressed as a ratio of radii, mean velocities or densities. It plays a key role in shaping the dark matter density distribution, and consequently the baryon density distribution. The relation adopted in this work (Eq. 5.8) allows us to compute the concentration parameter at $z = 0$. We modeled the redshift evolution as $c \propto (1 + z)^{-1}$, as suggested by previous works (Barkana & Loeb, 2002; Duffy et al., 2008; Ricotti, 2009).

The mass-redshift evolution of the concentration parameter is shown in fig A.1. The figure is the result of an extrapolation for low mass and high redshift of eq. 5.8. The concentration-mass-redshift relation for dark matter halos is still an open problem. The general approach to derive this relation is to observe the behaviour of halo concentration in simulations, for a fixed range of mass and redshift (Macciò et al., 2007; Klypin et al., 2016; Ludlow et al., 2016). It has been found that the concentration decreases with both redshift and mass, $c \propto M^{-\alpha}(1+z)^{-\beta}$ (Bullock & Boylan-Kolchin, 2017; Bullock et al., 2001). Besides this general trend, several controversies still exist. In Prada et al. (2012) was pointed out that a more general evolution can be obtained relating the concentration parameter to the r.m.s. fluctuation of the density field, $c(\sigma(M, z))$. This also implied an increasing trend with the halo mass/redshift supported by different works (Dutton & Macciò, 2014; Klypin et al., 2011). The apparent tension between those works and previous results was relaxed arguing that the effect appears due to the inclusion of non-relaxed halos in the sample (Ludlow et al., 2012). Part of the disagreement in the high-mass end is caused by the comparison of concentration based on radial ratios and concentration based on velocity ratios.

Different models also disagree on the concentration parameters of light-halos ($M < 10^8\, M_\odot$). Deriving halo concentration parameter from simulations suggests a power-law dependence both on redshift and mass. The resulting relations are valid in a fixed range of mass and redshift, extrapolating beyond the validity range often results in extremely high concentration values ($c > 100$) for very small halos ($M \sim 10^{-5} M_\odot$). Compact mini-halos can results in two effects: amplification of the annihilation rate, and overestimation of the boost factor due to substructure. The former has been observed in works relative to dark-matter annihilation resulting in γ-ray emission (e.g., Ando et al. 2019). The latter one has been addressed in Sánchez-Conde & Prada (2014), clarifying that a more conservative evolution of the concentration parameter (e.g. Prada et al., 2012)) can reduce this effect. We avoid this criticality since the region of the parameter space (M, z) in which the effect is dominant is always excluded by the evolution of the minimum halo mass.

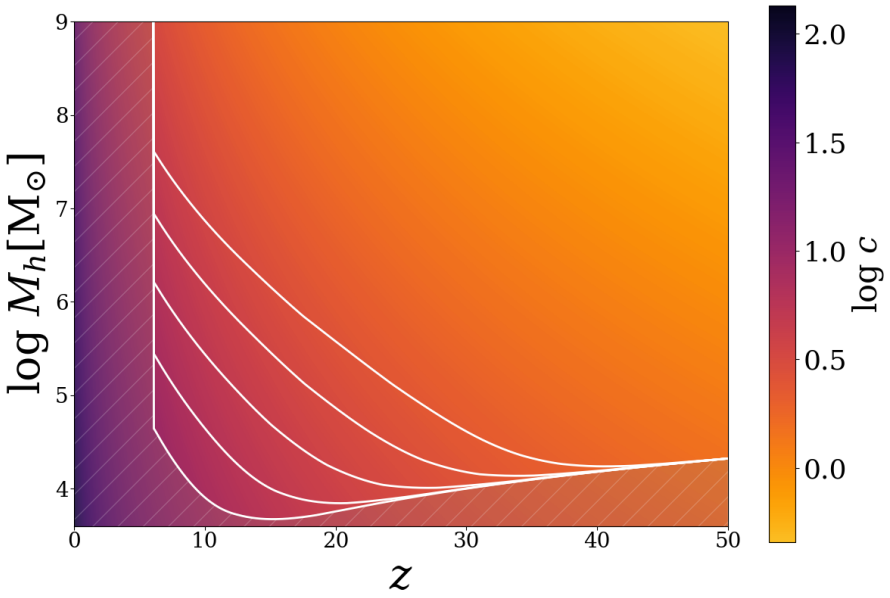

Figure A.1: Evolution of the concentration parameter $log\ c$ with mass and redshift. The white continuous lines represent different minimum halo masses as a function of $f_{\rm PBH} = 1, 0.1, 10^{-2}, 10^{-3}$.

A.2 Ionizing photons from PBHs

In this paper we neglect the effects of UV ionizing photons emitted by PBHs. To motivate this choice, we start from Fig. A.2, where we show the ratio between the Bondi radius and the Strömgren radius as a function of halo mass and redshift. From this figure, it is possible to determine whether UV photons are trapped inside the Bondi radius. We find that for very high accretion rates, $\dot{M} \gtrsim 10^{-1}\dot{M}_E$, UV photons cannot travel beyond the Bondi radius. This condition is verified in low-mass halos. Due to their large number density, they are the largest contributors to the cosmic backgrounds. This motivates our choice to neglect UV ionizing radiation in the model. A similar argument was presented in (Hasinger, 2020a). Even in the case of UV photons escaping the Bondi radius, the density of the surrounding medium is high enough to result in a fast hydrogen recombination. The condition $t_H/t_r > 1$ has to be verified for photons to escape the proximity of PBHs, where t_H is the Hubble time, and t_r is the recombination time.

A.3 Comparison with RAPSTER

According to our model, the seed mass $M_{\rm seed}$ is equal to the core mass M_c when Eq. 7.17 is satisfied. We remind that this condition means that all the PBHs contained in the core can collapse into a single seed if they are retained within the core itself during the runaway mergers. This occurs when the mass and the radius of the core are such that its escape velocity is larger than the maximum kick velocity v_k^{max} that a PBH can receive during the runaway mergers. This value can be as small as $\simeq$ 180 km s^{-1}, in the case of non-spinning PBHs (González et al., 2007), and as large as $\simeq$ 4000 km s^{-1} (Baker et al., 2008) for an optimal mass ratio and spin configuration. Since our assumed $v_k^{max} = 1000$ km s^{-1} value is smaller than the latter, we may underestimate the number of PBHs that are lost because of GW recoils. Furthermore, we are neglecting the fact that in a binary merger the remnant mass is lower then the sum of the two

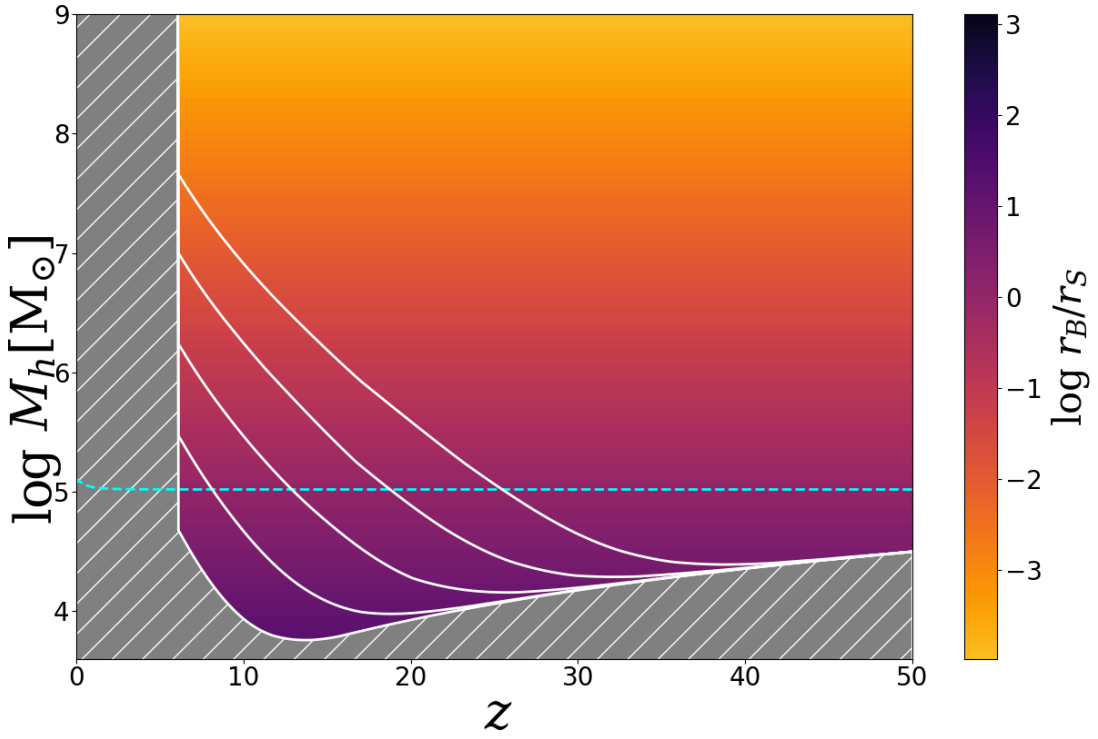

Figure A.2: Evolution of the ratio between the Bondi radius, r_B, and the Strömgren radius, r_S, as a function of halo mass and redshift. The computation is performed at a halo radius $r = 0.01\ r_{vir}$, and for a UV bolometric correction $f_{UV} = 0.01$. The dashed cyan line represents the case $r_B/r_S = 1$. The white continuous lines represent different minimum halo masses as a function of $f_{\rm PBH} = 1, 0.1, 10^{-2}, 10^{-3}$.

black holes masses, since a fraction of the initial rest mass is converted into GW emission. In other words, by considering $M_{\rm seed} = M_c$, we may overestimate the final seed mass.

To proper compute the fraction of PBHs retained by the cluster during the runaway mergers and the mass loss due to GW emissions, we adopt and modify the publicly available code Rapid Cluster Evolution (RAPSTER, Kritos et al., 2022). RAPSTER follows (i) the BH formation process from the death of massive stars, (ii) the formation of a BH core in the cluster, (iii) the subsequent dynamical formation of binary black holes (BBHs), and (iv) the final merging of BBHs in the cores of nuclear star clusters; it finally provides (v) the properties of the system resulting from the BBH merging and computes the corresponding gravitational wave emission. In particular, RAPSTER accounts for the mass loss due to recoil kicks, three body interactions, and GW emission and thus allows us to properly compute the mass retained in the cluster during the collapse (hereafter M_{rap}). The aim of this Appendix is thus to compare our estimated seed mass $M_{\rm seed}$ with the actual value M_{rap}.

The RAPSTER calculations start from an initial configuration that consists of a giant molecular cloud (GMC) of mass $M_{cl,0}$, radius $r_{cl,0}$ and metallicity Z. A fraction of the GMC mass, that depends on the assumed star formation efficiency ($\varepsilon_\star = 0.1$), fragments into stars whose masses are distributed according to the assumed initial mass function[1] (IMF). Massive stars ($> 20\ M_\odot$) evolve into BH remnants. This process determines the initial number of BHs in the cluster, $N_{\rm BH}^{tot}$. These black holes proceed to form a denser core inside the cluster due to energy equipartition between stars and black holes in a process called mass segregation. The radius of this core is

[1]The Kroupa IMF (Kroupa, 2001) is adopted, with a -2.3 power law index for $M_\star > 1\ M_\odot$.

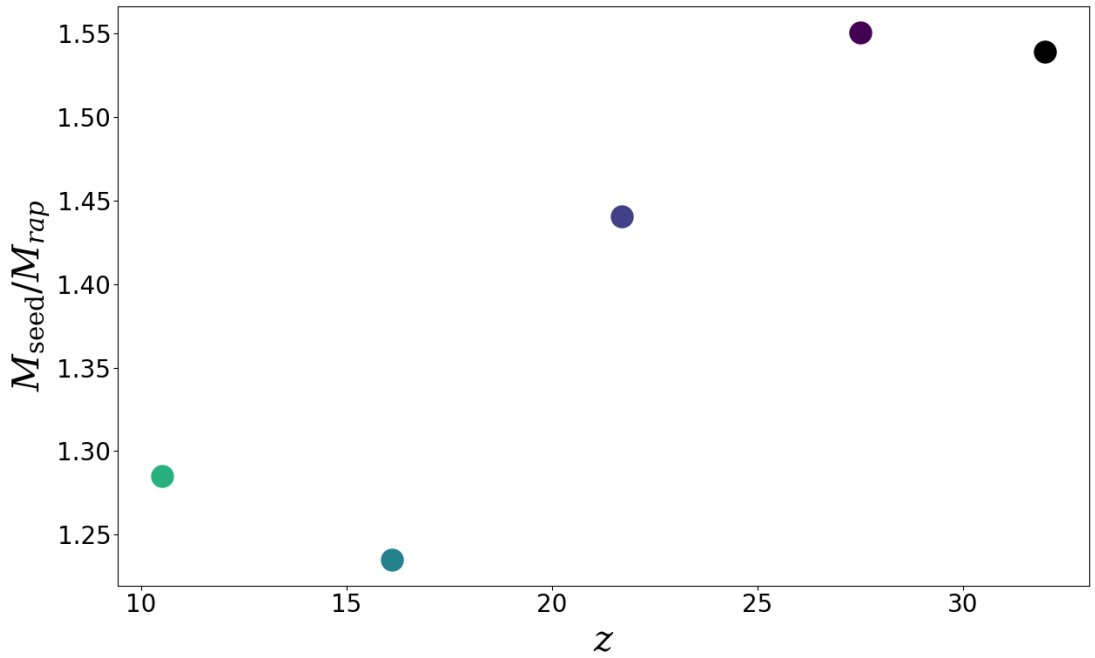

Figure A.3: Seed mass comparison. Ratio between our ($M_{\rm seed}$) and RAPSTER (M_{rap}) estimate of the final seed mass as a function of redshift, for the same cases shown in Fig. 7.4.

computed as:

$$\frac{r_{c,bh}}{r_{cl,0}} = 0.02 \frac{8}{\xi_{min}} \left(\frac{M_\bullet}{10\ M_\odot} \right)^2 \frac{n_{\rm bh}}{1000} \frac{0.64 M_\odot}{\bar{m}} \frac{10^6 M_\odot}{M_{cl}}, \tag{A.1}$$

where $\xi = M_\bullet \sigma_{\rm bh}^2 / \bar{m} \sigma_\star^2$, is the temperature ratio between black holes and stars, $\sigma_\star$ is the stellar velocity dispersion, and $\bar{m}$ is the mean stellar mass. As a result of interactions that occur in the dense cluster, energy is distributed among the members of the system, with BHs slowing down and lighter objects gaining kinetic energy via two-body encounters. As relics of massive star evolution, BHs become the heaviest components in the cluster, and if not already formed in the core, they sink into the central regions via dynamical friction on the stars.

We adapt the RAPSTER code to follow the evolution of a core composed of PBHs that is formed due to the dynamical friction on the gas. To this aim, we use the radius (r_c) and mass ($M_c = N_{\rm PBH} M_{\rm PBH}$) of the core (as computed in Sec. 7.2.5) for the initial configuration ($r_{cl,0}$ and $M_{cl,0}$ in the RAPSTER formalism).

We fix the cluster position in the center of the galaxy and we remove stars from the computation since we expect feedback from PBH accretion to stop the star formation process. We finally initialize PBHs spin to a monochromatic distribution peaked at the 0 value, as we expect PBHs to be non-spinning before the first generation of mergers (De Luca et al., 2020).

We plot in Fig. A.3 the $M_{\rm seed}$ to M_{rap} ratio for seeds formed at different redshifts. We find that, as expected, $M_{\rm seed}$ is always overestimating the M_{rap} value; however, the difference between the two values is not significant, being always smaller that a factor 1.6. We thus conclude that the equation $M_{\rm seed} = M_c$ and our assumption of $v_k^{max} = 1000$ km s^{-1} provide a satisfactory estimate of the final seed mass.

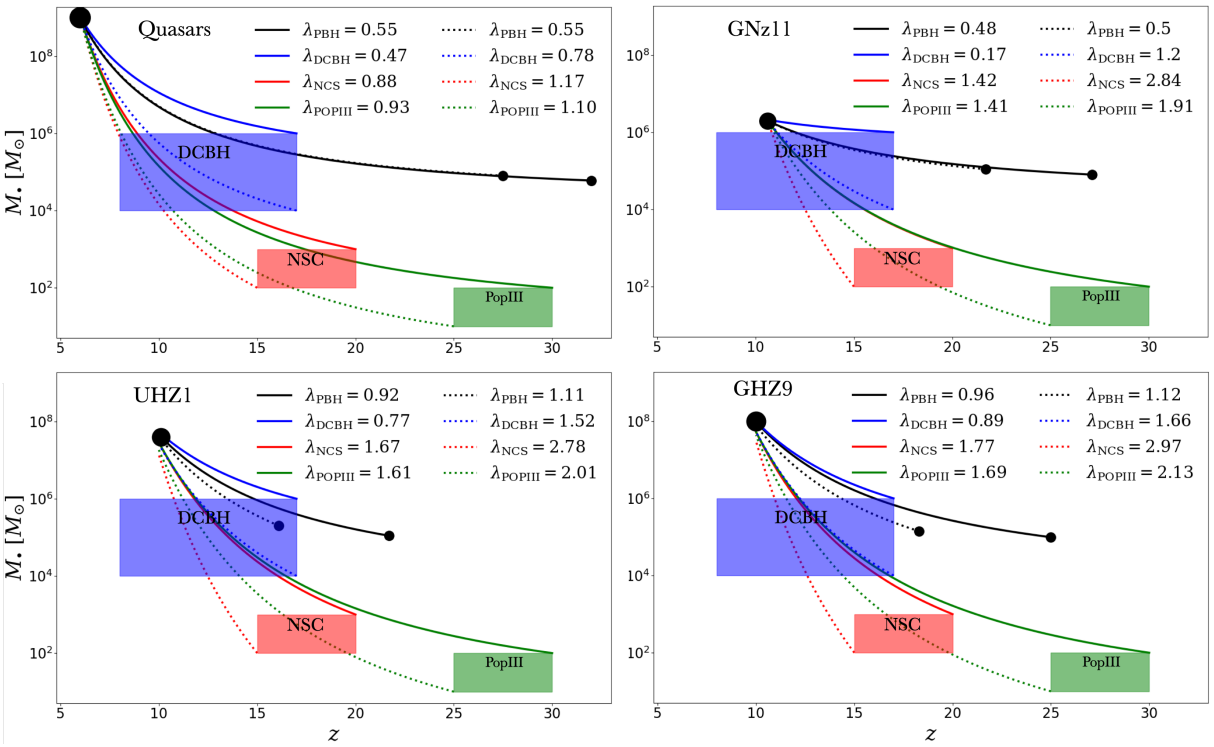

Figure A.4: Redshift evolution of seeds into $z \sim 6-10$ SMBHs. Large (small) circles represent SMBH observations (predicted PBH seeds). By assigning the halo mass to the observed SMBH hosts and evolving it back in cosmic time, we link each SMBH to its progenitor. The continuous (dotted) line represents the minimum (maximum) mean accretion rate ($\langle\lambda_E\rangle$) necessary to reach the final SMBH mass. The colored boxes mark the masses and redshifts interval of different seeding scenarios: DCBH (blue box), NSC (red box), PopIII remnants (green box). *Upper left panel:* The black circle represent the observations of a typical SMBH ($M_\bullet = 10^9\ M_\odot$) at redshift $z = 6$. PBH Seed masses of $M_{\rm seed} = 6-8\times10^4 M_\odot$ planted at $z = 27-32$ can reproduce the observed masses if accreting at a mean sub-Eddington accretion rate ($\lambda_E = 0.55$). For other seeding scenarios we find: $\lambda_{\rm DCBH} = 0.47-0.78$, $\lambda_{\rm NSC} = 0.88-1.17$, $\lambda_{\rm PopIII} = 0.93-1.10$. *Upper right panel:* The large black dot represents the massive black hole ($M_\bullet = 2\times10^6\ M_\odot$, Maiolino et al. 2023) hosted by GNz11 at redshift $z = 10.6$. We find that a seed mass of $M_{\rm seed} = 0.8-1\times10^5\ M_\odot$ planted at $z = 21.7-27.5$ can reproduce the observed SMBH mass ($M_\bullet \sim 2\times10^6\ M_\odot$) with a mean sub-Eddington accretion rate ($\lambda_E = 0.48-0.50$). For other seeding mechanism we find: $\lambda_{\rm DCBH} = 0.17-1.20$, $\lambda_{\rm NSC} = 1.42-2.84$, $\lambda_{\rm PopIII} = 1.41-1.91$. *Lower left panel:* The large black dot represents the massive black hole ($L_X \sim 2\times10^{44}$ erg s^{-1}, Bogdán et al. 2023a) powering UHZ1 at redshift $z = 10.1$. PBHs seeds of mass $M_{\rm seed} \sim 10^5$ M$_\odot$ planted at $z = 16.1-21.7$ can reproduce the observed luminosity with a mean accretion rate of $\lambda_E = 0.92-1.11$, and reach a final mass of $3-4\times10^7\ M_\odot$. Applying the same methodology to other seeding scenarios we find: $\lambda_{\rm DCBH} = 0.77-1.52$, $\lambda_{\rm NSC} = 1.67-2.78$, $\lambda_{\rm PopIII} = 1.61-2.01$. *Lower right panel:* The large black dot represents the massive black hole hosted in GHZ9 at redshift $z = 10$. PBH seeds of mass $M_{\rm seed} \sim 10^5$ M$_\odot$ planted at redshift $z = 18.3-25$ in massive halos ($M_h = 0.7-2\times10^8\ M_\odot$), and accreting with $\lambda_E = 0.96-1.12$ reproduce the observed bolometric luminosity ($L_{\rm B} \simeq 10^{46}$ erg s^{-1}, Kovacs et al. 2024b) and stellar mass $M_\star = 0.5-3.3\times10^8\ M_\odot$ (Atek et al., 2023; Castellano et al., 2023), and reach final BH masses of $M_\bullet = 0.7-1\times10^8\ M_\odot$. Similarly, for other seeding scenarios we find: $\lambda_{\rm DCBH} = 0.89-1.66$, $\lambda_{\rm NSC} = 1.77-2.97$, $\lambda_{\rm PopIII} = 1.69-2.13$.

A.4 Observational uncertainties

In this Appendix, we evaluate the impact of observational uncertainties on the mean accretion rates predicted for the PBH seeds in the four cases discussed in Sec. 7.4.

In Fig. 7.5, we have connected each observational data (large circles) to a single PBH seed (small circles) with a single mean accretion rate $\langle\lambda_{\rm E}\rangle$. We remind that this has been done through the following steps: i) to estimate the mass of the hosting halo (M_h) from the stellar mass ($M_\star$) inferred from observations: $M_\star = \varepsilon_\star(\Omega_b/\Omega_m)M_h$, where $\varepsilon_\star = 0.1$ is the star formation efficiency; ii) to track M_h backward in time, following Fakhouri et al. (2010); iii) to identify the crossing redshift ($z_\times$) and mass ($M_{h,\times}$) that determine the redshift ($z_{\rm seed}$) and mass ($M_{\rm seed}$) of the PBH seed; iv) to compute the average Eddington ratio to which the seed should accrete to explain the observed data. So far, for step i), we have used the $M_\star$ upper limit of each observational case.

In this Appendix, we instead consider both the lower and upper limits of $M_\star$ that convert into a minimum and maximum $z_{\rm seed}$ and $M_{\rm seed}$, thus finally providing a maximum and minimum value for $\langle\lambda_{\rm E}\rangle$, respectively. Similarly, for the other seeding scenarios, we consider the minimum/maximum seed mass and formation redshift as predicted by theoretical models. In these cases, the minimum and maximum $\langle\lambda_{\rm E}\rangle$ value is associated to the maxima seed mass/formation redshift and minima seed mass/formation redshift, respectively. The results are shown in Fig. A.4.

For what concerns $z \sim 6$ quasars (upper left panel), we find that their masses can be explained without relying on super-Eddington accretion, independently of the considered seeding mechanism. Following Costa (2023), we assume that $M_\bullet = 10^9\ M_\odot$ are hosted into $M_h = 10^{12-13}\ M_\odot$ dark matter halos. These halo masses correspond to PBH progenitors with $M_{\rm seed} = 6 - 8 \times 10^4 M_\odot$ planted at redshift $z = 32 - 27$. To grow into the SMBHs at redshift $z = 6$, both seeds require the same accretion history with a mean accretion rate of $\lambda_{\rm PBH} = 0.55$. This value is consistent with the accretion rate required for DCBHs to evolve into the same SMBH masses $\lambda_{\rm DCBH} = 0.47 - 0.78$. Viceversa, both the NSCs and PopIII scenarios require accretion rates closer to the Eddington limit: ($\lambda_{\rm NSC} = 0.88 - 1.17$, $\lambda_{\rm PopIII} = 0.93 - 1.10$).

To determine the mass of the dark matter halo hosting GNz11 (upper right panel), we use the observational esteem of the galaxy stellar mass $M_\star \simeq 10^{9-10}\ M_\odot$ by Maiolino et al. 2023. Thus, PBH seeds forming between redshift $z = 27.5 - 21.7$ with masses of $M_{\rm seed} = 0.8 - 1 \times 10^5\ M_\odot$ reproduce the observed mass of the BH inside GNz11 ($M_\bullet = 2 \times 10^6\ M_\odot$) with a mean accretion rate of $\lambda_{\rm PBH} \sim 0.48 - 0.50$. For what concerns the DCBH scenario, models predict seed masses very close to the BH mass in GNz11, and an interval of redshift for their formation that includes the GNz11 redshift. In this case, we only consider the upper limit of this interval that implies an extremely low mean accretion rate value ($\lambda_{\rm DCBH} = 0.17$). In the other cases, super-Eddington accretion is always necessary to match the observed BH mass: $\lambda_{\rm NSC} = 1.42 - 2.84$, $\lambda_{\rm PopIII} = 1.41 - 1.91$.

In the case of UHZ1 and GHZ9 (Bogdán et al., 2023a; Kovacs et al., 2024b) the inferred stellar masses are very close to the BH masses. These high BH to stellar mass ratios ($M_\bullet/M_\star \sim 1$) imply a very rapid BH assembly for both sources. For UHZ1 (lower left pabel), we adopt the stellar mass estimate ($M_\star = 0.4 - 1.9 \times 10^8\ M_\odot$) provided by Castellano et al. (2023) which converts into $M_h \simeq 0.4 - 2 \times 10^9\ M_\odot$. PBH seeds with masses $M_{\rm seed} \simeq 10^5 M_\odot$ planted at redshift $z = 16.1 - 21.7$ can reproduce the observed luminosity ($L_x \sim 2 \times 10^{44}{\rm erg\ s^{-1}}$) with a mean accretion rate of $\lambda_{\rm PBH} = 0.92 - 1.11$. Similarly, DCBHs can reproduce the UHZ1 luminosity with $\lambda_{\rm DCBH} = 0.77 - 1.52$. The other two seeding scenarios require instead higher (super-Eddington) mean accretion rates for a prolonged period of time (< 200 Myr): $\lambda_{\rm NSC} =$

$1.67-2.78$, $\lambda_{\rm PopIII}=1.61-2.01$.

In the case of GHZ9 (lower right panel), for the galaxy stellar mass we use the value $M_\star = 0.5-3.3\times10^8\ M_\odot$ (Castellano et al., 2023; Atek et al., 2023). PBH seeds planted at redshift $z = 18-25$ with masses $M_{\rm seed}=10^5\ M_\odot$ can explain the observed luminosity ($L_B=10^{46}{\rm erg\ s^{-1}}$) with a mean accretion history of $\lambda_{\rm PBH}=0.96-1.12$. In the case of DCBHs, a mean accretion rate close to the Eddington rate ($\lambda_{\rm DCBH}=0.89-1.66$) is required to explain the high inferred BH mass ($M_\bullet\sim10^8\ M_\odot$) at the high observational redshift ($z=10.3$). The other two seeding scenarios require sustained super-Eddington accretion: $\lambda_{\rm NSC}=1.77-2.97$, $\lambda_{\rm PopIII}=1.69-2.13$.

Bibliography

Abbott L. S. C., Collaboration V., 2016, Phys. Rev. Lett., 116, 061102

Abbott B. P., et al., 2016, Phys. Rev. Lett., 116, 061102

Abbott B. P., et al., 2017, Phys. Rev. D, 96, 022001

Abbott B. P., et al., 2019, The Astrophysical Journal Letters, 882, L24

Abbott R., et al., 2020a, Phys. Rev. Lett., 125, 101102

Abbott B. P., et al., 2020b, ApJL, 892, L3

Abbott R., et al., 2020c, ApJL, 896, L44

Afshordi N., McDonald P., Spergel D. N., 2003, ApJL, 594, L71

Agarwal B., Dalla Vecchia C., Johnson J. L., Khochfar S., Paardekooper J.-P., 2014, MNRAS, 443, 648

Agazie G., et al., 2023, ApJL, 951, L8

Alcock C., et al., 2000, ApJ, 542, 281

Ali-Haïmoud Y., 2018, Phys. Rev. Lett., 121, 081304

Ali-Haïmoud Y., Kamionkowski M., 2017, Phys. Rev. D, 95, 043534

Ali-Haïmoud Y., Kovetz E. D., Kamionkowski M., 2017, Phys. Rev. D, 96, 123523

Ananna T. T., Treister E., Urry C. M., Ricci C., Hickox R. C., Padmanabhan N., Marchesi S., Kirkpatrick A., 2020, ApJ, 889, 17

Anderson L. D., Bania T. M., Jackson J. M., Clemens D. P., Heyer M., Simon R., Shah R. Y., Rathborne J. M., 2009, ApJS, 181, 255

Ando S., Ishiyama T., Hiroshima N., 2019, Galaxies, 7, 68

Atek H., et al., 2023, MNRAS, 524, 5486

Bañados E., et al., 2018, Nature, 553, 473

Baker J. G., Boggs W. D., Centrella J., Kelly B. J., McWilliams S. T., Miller M. C., van Meter J. R., 2008, ApJL, 682, L29

Ballesteros G., Serpico P. D., Taoso M., 2018, JCAP, 2018, 043

Barkana R., 2018, Nature, 555, 71

Barkana R., Loeb A., 2001, Physics Reports, 349, 125

Barkana R., Loeb A., 2002, ApJ, 578, 1

Barnacka A., Glicenstein J. F., Moderski R., 2012, Phys. Rev. D, 86, 043001

Bernal J. L., Raccanelli A., Verde L., Silk J., 2018, JCAP, 2018, 017

Bhatt M., et al., 2024, arXiv e-prints, p. arXiv:2401.13733

Binney J., Tremaine S., 2008, Galactic Dynamics: Second Edition

Bird S., Cholis I., Muñoz J. B., Ali-Haïmoud Y., Kamionkowski M., Kovetz E. D., Raccanelli A., Riess A. G., 2016, Phys. Rev. Lett., 116, 201301

Blaineau T., et al., 2022, A&A, 664, A106

Blinnikov S., Dolgov A., Porayko N., Postnov K., 2016, JCAP, 2016, 036

Boco L., Lapi A., Danese L., 2020, ApJ, 891, 94

Boco L., Lapi A., Sicilia A., Capurri G., Baccigalupi C., Danese L., 2021, JCAP, 2021, 035

Bogdán Á., et al., 2023a, Nature Astronomy,

Bogdan A., et al., 2023b, arXiv e-prints, p. arXiv:2305.15458

Bondi H., 1952, MNRAS, 112, 195

Bondi H., Hoyle F., 1944, Monthly Notices of the Royal Astronomical Society, 104, 273

Bowman J. D., Rogers A. E. E., Monsalve R. A., Mozdzen T. J., Mahesh N., 2018, Nature, 555, 67

Brandt T. D., 2016, ApJL, 824, L31

Brandt W. N., Hasinger G., 2005, ARA&A, 43, 827

Bromm V., Loeb A., 2003, ApJ, 596, 34

Bucher M., 2015, International Journal of Modern Physics D, 24, 1530004

Bullock J. S., Boylan-Kolchin M., 2017, Annual Review of Astronomy and Astrophysics, 55, 343–387

Bullock J. S., Kolatt T. S., Sigad Y., Somerville R. S., Kravtsov A. V., Klypin A. A., Primack J. R., Dekel A., 2001, MNRAS, 321, 559

Cang J., Gao Y., Ma Y.-Z., 2021, arXiv e-prints, p. arXiv:2108.13256

Capela F., Pshirkov M., Tinyakov P., 2013, Phys. Rev. D, 87, 123524

Cappelluti N., et al., 2013, ApJ, 769, 68

Cappelluti N., et al., 2017, ApJ, 837, 19

Cappelluti N., Hasinger G., Natarajan P., 2021, arXiv e-prints, p. arXiv:2109.08701

Cappelluti N., Hasinger G., Natarajan P., 2022, ApJ, 926, 205

Carr B. J., 1975, ApJ, 201, 1

Carr B. J., Hawking S. W., 1974, MNRAS, 168, 399

Carr B., Kühnel F., 2020, Annual Review of Nuclear and Particle Science, 70, 355

Carr B., Kuhnel F., 2021, arXiv e-prints, p. arXiv:2110.02821

Carr B., Silk J., 2018, MNRAS, 478, 3756

Carr B., Kühnel F., Sandstad M., 2016, Phys. Rev. D, 94, 083504

Carr B., Raidal M., Tenkanen T., Vaskonen V., Veermäe H., 2017, Phys. Rev. D, 96, 023514

Carr B., Clesse S., García-Bellido J., 2019, arXiv e-prints, p. arXiv:1904.02129

Carr B., Kohri K., Sendouda Y., Yokoyama J., 2021, Reports on Progress in Physics, 84, 116902

Castellano M., et al., 2023, ApJL, 948, L14

Chapline G. F., 1975, Nature, 253, 251

Chen S., Zhang H.-H., Long G., 2022, Phys. Rev. D, 105, 063008

Cheng Y.-T., Bock J. J., 2022, ApJ, 940, 115

Chisholm J. R., 2006, Phys. Rev. D, 73, 083504

Civano F., et al., 2016, ApJ, 819, 62

Clesse S., García-Bellido J., 2017, Physics of the Dark Universe, 15, 142

Clesse S., García-Bellido J., 2022, Physics of the Dark Universe, 38, 101111

Condon J. J., 1984, ApJ, 287, 461

Condon J. J., 1992, ARA&A, 30, 575

Condon J. J., Cotton W. D., Greisen E. W., Yin Q. F., Perley R. A., Taylor G. B., Broderick J. J., 1998, AJ, 115, 1693

Condon J. J., et al., 2012, ApJ, 758, 23

Coogan A., Morrison L., Profumo S., 2021, Phys. Rev. Lett., 126, 171101

Cooray A., Bock J. J., Keatin B., Lange A. E., Matsumoto T., 2004, ApJ, 606, 611

Cooray A., et al., 2012a, Nature, 490, 514

Cooray A., Gong Y., Smidt J., Santos M. G., 2012b, ApJ, 756, 92

Costa T., 2023, arXiv e-prints, p. arXiv:2308.12987

Cyburt R. H., Fields B. D., Olive K. A., 2003, Physics Letters B, 567, 227

Davies M. B., Miller M. C., Bellovary J. M., 2011, ApJL, 740, L42

De Luca V., Franciolini G., Pani P., Riotto A., 2020, JCAP, 2020, 052

De Luca V., Desjacques V., Franciolini G., Pani P., Riotto A., 2021, Phys. Rev. Lett., 126, 051101

De Luca V., Franciolini G., Riotto A., Veermäe H., 2022, Phys. Rev. Lett., 129, 191302

Devecchi B., Volonteri M., 2009, ApJ, 694, 302

Dodelson S., 2003, Modern Cosmology

Dolgov A., Silk J., 1993, Phys. Rev. D, 47, 4244

Driver S. P., et al., 2016, ApJ, 827, 108

Düchting N., 2004, Phys. Rev. D, 70, 064015

Duffy A. R., Schaye J., Kay S. T., Dalla Vecchia C., 2008, MNRAS, 390, L64

Dutton A. A., Macciò A. V., 2014, MNRAS, 441, 3359

Eckart A., Genzel R., 1996, Nature, 383, 415

Edgar R., 2004, New Astronomy Reviews, 48, 843

Einstein A., 1916, Annalen der Physik, 354, 769

Eisenstein D. J., Loeb A., 1995, ApJ, 443, 11

Elvis M., et al., 2009, ApJS, 184, 158

Event Horizon Telescope Collaboration et al., 2019, ApJL, 875, L1

Ewall-Wice A., Chang T. C., Lazio J., Doré O., Seiffert M., Monsalve R. A., 2018, ApJ, 868, 63

Ewall-Wice A., Chang T.-C., Lazio T. J. W., 2019, arXiv e-prints, p. arXiv:1903.06788

Ewall-Wice A., Chang T.-C., Lazio T. J. W., 2020, MNRAS, 492, 6086

Fabian A. C., Barcons X., 1992, ARA&A, 30, 429

Fakhouri O., Ma C.-P., Boylan-Kolchin M., 2010, MNRAS, 406, 2267

Fan X., et al., 2006, AJ, 131, 1203

Fan X., Bañados E., Simcoe R. A., 2023, ARA&A, 61, 373

Farina E. P., et al., 2022, ApJ, 941, 106

Fernandez E. R., Komatsu E., Iliev I. T., Shapiro P. R., 2010, ApJ, 710, 1089

Ferrara A., 2012, Nature, 490, 494

Ferrara A., Salvadori S., Yue B., Schleicher D., 2014, MNRAS, 443, 2410

Ferrarese L., Ford H., 2005, Space Science Reviews, 116, 523

Ferrarese L., Merritt D., 2000, ApJL, 539, L9

Fialkov A., Barkana R., 2019, MNRAS, 486, 1763

Fialkov A., Barkana R., Cohen A., 2018, Phys. Rev. Lett., 121, 011101

Fixsen D. J., et al., 2011, The Astrophysical Journal, 734, 5

Franciolini G., 2021, arXiv e-prints, p. arXiv:2110.06815

Franciolini G., Musco I., Pani P., Urbano A., 2022, Phys. Rev. D, 106, 123526

Franciolini G., Junior Iovino A., Vaskonen V., Veermae H., 2023, arXiv e-prints, p. arXiv:2306.17149

Friedmann A., 1922, Zeitschrift fur Physik, 10, 377

Furlanetto S. R., Stoever S. J., 2010, MNRAS, 404, 1869

Gaggero D., Bertone G., Calore F., Connors R. M. T., Lovell M., Markoff S., Storm E., 2017, Phys. Rev. Lett., 118, 241101

Gaikwad P., et al., 2020, MNRAS, 494, 5091

Gallo E., Fender R. P., Pooley G. G., 2003, MNRAS, 344, 60

García-Bellido J., Ruiz Morales E., 2017, Physics of the Dark Universe, 18, 47

Gebhardt K., et al., 2000, ApJL, 539, L13

Germani C., Musco I., 2019, Phys. Rev. Lett., 122, 141302

Ghez A. M., et al., 2008, ApJ, 689, 1044

Giacconi R., Gursky H., Paolini F. R., Rossi B. B., 1962, Phys. Rev. Lett., 9, 439

Gillessen S., Eisenhauer F., Trippe S., Alexander T., Genzel R., Martins F., Ott T., 2009, ApJ, 692, 1075

Gilli R., Risaliti G., Salvati M., 1999, A&A, 347, 424

Gilli R., Comastri A., Hasinger G., 2007, A&A, 463, 79

González J. A., Sperhake U., Brügmann B., Hannam M., Husa S., 2007, Phys. Rev. Lett., 98, 091101

Green D. A., 2019, Journal of Astrophysics and Astronomy, 40, 36

Green A. M., Kavanagh B. J., 2021, Journal of Physics G Nuclear Physics, 48, 043001

Green A. M., Liddle A. R., Malik K. A., Sasaki M., 2004, Phys. Rev. D, 70, 041502

Griest K., Cieplak A. M., Lehner M. J., 2014, ApJ, 786, 158

Gültekin K., et al., 2009, ApJ, 698, 198

Gundlach C., 2000, arXiv e-prints, pp gr–qc/0001046

Harada T., Yoo C.-M., Kohri K., 2013, Phys. Rev. D, 88, 084051

Hasinger G., 2020a, JCAP, 2020, 022

Hasinger G., 2020b, JCAP, 2020, 022

Hawking S., 1971, MNRAS, 152, 75

Hawking S. W., 1974, Nature, 248, 30

Heger A., Fryer C. L., Woosley S. E., Langer N., Hartmann D. H., 2003, ApJ, 591, 288

Hektor A., Hütsi G., Marzola L., Raidal M., Vaskonen V., Veermäe H., 2018, Phys. Rev. D, 98, 023503

Helgason K., Ricotti M., Kashlinsky A., 2012, ApJ, 752, 113

Helgason K., Ricotti M., Kashlinsky A., Bromm V., 2016, MNRAS, 455, 282

Hickox R. C., Markevitch M., 2006, ApJ, 645, 95

Hickox R. C., Markevitch M., 2007, ApJL, 661, L117

Hinshaw G., et al., 2013, ApJS, 208, 19

Hooper D., Goodenough L., 2011, Physics Letters B, 697, 412

Hoyle F., Lyttleton R. A., 1939, Mathematical Proceedings of the Cambridge Philosophical Society, 35, 405–415

Hubble E., 1929, Proceedings of the National Academy of Science, 15, 168

Inman D., Ali-Haïmoud Y., 2019, Phys. Rev. D, 100, 083528

Jansky K. G., 1933, Popular Astronomy, 41, 548

Jedamzik K., 2021, Phys. Rev. Lett., 126, 051302

Kannike K., Marzola L., Raidal M., Veermäe H., 2017, JCAP, 2017, 020

Kashlinsky A., 2016a, ApJL, 823, L25

Kashlinsky A., 2016b, ApJL, 823, L25

Kashlinsky A., Odenwald S., 2000, ApJ, 528, 74

Kashlinsky A., Mather J. C., Odenwald S., Hauser M. G., 1996, ApJ, 470, 681

Kashlinsky A., Arendt R. G., Mather J., Moseley S. H., 2007, ApJL, 654, L1

Kashlinsky A., Arendt R. G., Ashby M. L. N., Fazio G. G., Mather J., Moseley S. H., 2012, ApJ, 753

Kashlinsky A., Arendt R. G., Atrio-Barandela F., Cappelluti N., Ferrara A., Hasinger G., 2018, RMP, 90

Katz N., Weinberg D. H., Hernquist L., 1996, ApJS, 105, 19

Kavanagh B., 2019, doi:10.5281/zenodo.3538999

Kavanagh B. J., Gaggero D., Bertone G., 2018, Phys. Rev. D, 98, 023536

Kawasaki M., Kusenko A., Yanagida T. T., 2012, Physics Letters B, 711, 1

Klypin A. A., Trujillo-Gomez S., Primack J., 2011, ApJ, 740, 102

Klypin A., Yepes G., Gottlöber S., Prada F., Heß S., 2016, MNRAS, 457, 4340

Kohri K., Terada T., 2018, Classical and Quantum Gravity, 35, 235017

Kormendy J., Ho L. C., 2013, ARA&A, 51, 511

Kovacs O. E., et al., 2024a, arXiv e-prints, p. arXiv:2403.14745

Kovacs O. E., et al., 2024b, arXiv e-prints, p. arXiv:2403.14745

Kritos K., Strokov V., Baibhav V., Berti E., 2022, arXiv e-prints, p. arXiv:2210.10055

Kroupa P., 2001, MNRAS, 322, 231

Kühnel F., Freese K., 2017, Phys. Rev. D, 95, 083508

Kurk J. D., et al., 2007, ApJ, 669, 32

Laha R., 2019, Phys. Rev. Lett., 123, 251101

Latif M. A., Ferrara A., 2016, Publ. Astr. Soc. Australia, 33, e051

Latif M. A., Schleicher D. R. G., Schmidt W., Niemeyer J., 2013, MNRAS, 433, 1607

Leinert C., et al., 1998, A&A Supp., 127, 1

Loeb A., 2010, How did the first stars and galaxies form?. Princeton University Press

Lu P., Takhistov V., Gelmini G. B., Hayashi K., Inoue Y., Kusenko A., 2021, ApJL, 908, L23

Ludlow A. D., Navarro J. F., Li M., Angulo R. E., Boylan-Kolchin M., Bett P. E., 2012, MNRAS, 427, 1322

Ludlow A. D., Bose S., Angulo R. E., Wang L., Hellwing W. A., Navarro J. F., Cole S., Frenk C. S., 2016, Monthly Notices of the Royal Astronomical Society, 460, 1214

Lupi A., Colpi M., Devecchi B., Galanti G., Volonteri M., 2014, MNRAS, 442, 3616

Macciò A. V., Dutton A. A., van den Bosch F. C., Moore B., Potter D., Stadel J., 2007, MNRAS, 378, 55

Madau P., Rees M. J., 2001, ApJL, 551, L27

Madau P., Silk J., 2005, Monthly Notices of the Royal Astronomical Society, 359, L37

Madau P., Meiksin A., Rees M. J., 1997, ApJ, 475, 429

Madau P., Pozzetti L., Dickinson M., 1998, ApJ, 498, 106

Magorrian J., et al., 1998, The Astronomical Journal, 115, 2285

Maiolino R., et al., 2023, arXiv e-prints, p. arXiv:2305.12492

Makino N., Sasaki S., Suto Y., 1998, ApJ, 497, 555

Manshanden J., Gaggero D., Bertone G., Connors R. M. T., Ricotti M., 2019, JCAP, 2019, 026

Manzoni D., Ziparo F., Gallerani S., Ferrara A., 2024, MNRAS, 527, 4153

Matsumoto T., Kim M. G., Pyo J., Tsumura K., 2015, ApJ, 807, 57

Matsuura S., et al., 2017, ApJ, 839, 7

Matthews T. A., Sandage A. R., 1963, ApJ, 138, 30

Mazzucchelli C., et al., 2023, A&A, 676, A71

Mena O., Palomares-Ruiz S., Villanueva-Domingo P., Witte S. J., 2019, Phys. Rev. D, 100, 043540

Merloni A., Heinz S., di Matteo T., 2003, MNRAS, 345, 1057

Mesinger A., Furlanetto S., Cen R., 2011, MNRAS, 411, 955

Mesinger A., Ferrara A., Spiegel D. S., 2013, MNRAS, 431, 621

Meszaros P., 1975, A&A, 38, 5

Mirocha J., Furlanetto S. R., 2019, MNRAS, 483, 1980

Mo H., van den Bosch F. C., White S., 2010, Galaxy Formation and Evolution

Monroy-Rodríguez M. A., Allen C., 2014, ApJ, 790, 159

Moretti A., Campana S., Lazzati D., Tagliaferri G., 2003, ApJ, 588, 696

Mortlock D. J., et al., 2011, Nature, 474, 616

Muñoz J. B., Loeb A., 2018, arXiv e-prints, p. arXiv:1802.10094

Murray S. G., Power C., Robotham A. S. G., 2013, Astronomy and Computing, 3, 23

Musco I., Miller J. C., Rezzolla L., 2005, Classical and Quantum Gravity, 22, 1405

Musco I., Miller J. C., Polnarev A. G., 2009, Classical and Quantum Gravity, 26, 235001

Mushotzky R. F., Cowie L. L., Barger A. J., Arnaud K. A., 2000, Nature, 404, 459

Navarro J. F., Frenk C. S., White S. D. M., 1997, ApJ, 490, 493

Nicastro F., et al., 2005, Nature, 433, 495

Niemeyer J. C., Jedamzik K., 1999, Phys. Rev. D, 59, 124013

Niikura H., Takada M., Yokoyama S., Sumi T., Masaki S., 2019, Phys. Rev. D, 99, 083503

Norris R. P., et al., 2011, Publ. Astr. Soc. Australia, 28, 215

O'Brien B., Szczepańczyk M., Gayathri V., Bartos I., Vedovato G., Prodi G., Mitselmakher G., Klimenko S., 2021, Phys. Rev. D, 104, 082003

Onken C. A., Ferrarese L., Merritt D., Peterson B. M., Pogge R. W., Vestergaard M., Wandel A., 2004, ApJ, 615, 645

Ostriker E. C., 1999, ApJ, 513, 252

Pacucci F., Nguyen B., Carniani S., Maiolino R., Fan X., 2023, ApJL, 957, L3

Park K., Bogdanović T., 2017, ApJ, 838, 103

Partridge R. B., Peebles P. J. E., 1967, ApJ, 148, 377

Peacock J. A., 1998, Cosmological Physics. Cambridge University Press, doi:10.1017/CBO9780511804533

Peebles P. J. E., 1993, Principles of Physical Cosmology

Penzias A. A., Wilson R. W., 1965, ApJ, 142, 419

Peterson B. M., et al., 2004, ApJ, 613, 682

Planck Collaboration 2018, arXiv e-prints, p. arXiv:1807.06209

Planck Collaboration et al., 2016, A&A, 594, A13

Planck Collaboration et al., 2020, A&A, 641, A6

Poulin V., Serpico P. D., Calore F., Clesse S., Kohri K., 2017, Phys. Rev. D, 96, 083524

Prada F., Klypin A. A., Cuesta A. J., Betancort-Rijo J. E., Primack J., 2012, Monthly Notices of the Royal Astronomical Society, 423, 3018

Press W. H., Schechter P., 1974, ApJ, 187, 425

Puchwein E., Haardt F., Haehnelt M. G., Madau P., 2019, MNRAS, 485, 47

Punturo M., et al., 2010, Classical and Quantum Gravity, 27, 194002

Raidal M., Vaskonen V., Veermäe H., 2017, JCAP, 2017, 037

Reber G., 1944, ApJ, 100, 279

Reines A. E., Volonteri M., 2015, The Astrophysical Journal, 813, 82

Remillard R. A., McClintock J. E., 2006, ARA&A, 44, 49

Rengelink R. B., Tang Y., de Bruyn A. G., Miley G. K., Bremer M. N., Roettgering H. J. A., Bremer M. A. R., 1997, A&A Supp., 124, 259

Reynolds S. P., 2008, ARA&A, 46, 89

Ricotti M., 2009, MNRAS, 392, L45

Ricotti M., Ostriker J. P., Mack K. J., 2008a, ApJ, 680, 829

Ricotti M., Ostriker J. P., Mack K. J., 2008b, ApJ, 680, 829

Riess A. G., et al., 1998, AJ, 116, 1009

Roncadelli M., Treves A., Turolla R., 2009, arXiv e-prints, p. arXiv:0901.1093

Rybicki G. B., Lightman A. P., 1986, Radiative Processes in Astrophysics

Salpeter E. E., 1955, ApJ, 121, 161

Salpeter E. E., 1964, ApJ, 140, 796

Salvador-Solé E., Solanes J. M., Manrique A., 1998, ApJ, 499, 542

Salvaterra R., Ferrara A., 2003, MNRAS, 339, 973

Salvaterra R., Ferrara A., 2006, MNRAS, 367, L11

Salvaterra R., Haardt F., Volonteri M., Moretti A., 2012, A&A, 545, L6

Sánchez-Conde M. A., Prada F., 2014, MNRAS, 442, 2271

Sano K., Kawara K., Matsuura S., Kataza H., Arai T., Matsuoka Y., 2015, ApJ, 811, 77

Santos M. R., Bromm V., Kamionkowski M., 2002, MNRAS, 336, 1082

Sasaki M., Suyama T., Tanaka T., Yokoyama S., 2016, Phys. Rev. Lett., 117, 061101

Schmidt M., 1963, Nature, 197, 1040

Scott D., Rees M. J., 1990, MNRAS, 247, 510

Serpico P. D., Poulin V., Inman D., Kohri K., 2020, Physical Review Research, 2, 023204

Shakura N. I., Sunyaev R. A., 1973, A&A, 24, 337

Shapiro S. L., 1973, ApJ, 180, 531

Shibata M., Sasaki M., 1999, Phys. Rev. D, 60, 084002

Silk J., Rees M. J., 1998, A&A, 331, L1

Smyth N., Profumo S., English S., Jeltema T., McKinnon K., Guhathakurta P., 2020, Phys. Rev. D, 101, 063005

Tada Y., Yokoyama S., 2015, Phys. Rev. D, 91, 123534

Tinker J. L., Robertson B. E., Kravtsov A. V., Klypin A., Warren M. S., Yepes G., Gottlöber S., 2010, ApJ, 724, 878

Tisserand P., et al., 2007, A&A, 469, 387

Treister E., Urry C. M., 2006, ApJL, 652, L79

Treister E., Urry C. M., Virani S., 2009, ApJ, 696, 110

Tsumura K., Matsumoto T., Matsuura S., Sakon I., Wada T., 2013, Pub. Astron. Soc. Japan, 65

Ueda Y., Akiyama M., Hasinger G., Miyaji T., Watson M. G., 2014, ApJ, 786, 104

Valdés M., Evoli C., Ferrara A., 2010, MNRAS, 404, 1569

Vaskonen V., Veermäe H., 2021, Phys. Rev. Lett., 126, 051303

Villanueva-Domingo P., Ichiki K., 2021, arXiv e-prints, p. arXiv:2104.10695

Voit G. M., 2005, Reviews of Modern Physics, 77, 207

Volonteri M., Rees M. J., 2005, ApJ, 633, 624

Volonteri M., Haardt F., Madau P., 2003, ApJ, 582, 559

Walther M., Oñorbe J., Hennawi J. F., Lukić Z., 2019, ApJ, 872, 13

Wang R., Wu X.-B., Kong M.-Z., 2006, ApJ, 645, 890

Willott C. J., et al., 2007, AJ, 134, 2435

Willott C. J., et al., 2010, AJ, 139, 906

Wong K. W. K., Franciolini G., De Luca V., Baibhav V., Berti E., Pani P., Riotto A., 2021, Phys. Rev. D, 103, 023026

Xie F.-G., Yuan F., 2012, MNRAS, 427, 1580

Yoshida N., Omukai K., Hernquist L., Abel T., 2006, ApJ, 652, 6

Yuan F., Narayan R., 2014, ARA&A, 52, 529

Yue B., Ferrara A., Salvaterra R., Chen X., 2013, Monthly Notices of the Royal Astronomical Society, 431, 383

.

Zel'dovich Y. B., Novikov I. D., 1966, , 43, 758

Ziparo F., Gallerani S., Ferrara A., Vito F., 2022, MNRAS, 517, 1086

Zoutendijk S. L., et al., 2020, A&A, 635, A107

de Oliveira-Costa A., Tegmark M., Gaensler B. M., Jonas J., Landecker T. L., Reich P., 2008, MNRAS, 388, 247

van Haarlem M. P., et al., 2013, A&A, 556, A2